

**Manipulator Identification and Control Using a Base-Mounted  
Force/Torque Sensor**

by

**Karl David Iagnemma**

Bachelor of Science in Mechanical Engineering  
Univeristy of Michigan (1994)

Submitted to the  
Department of Mechanical Engineering  
in partial fulfillment of the requirements for the degree of

**Master of Science in Mechanical Engineering**

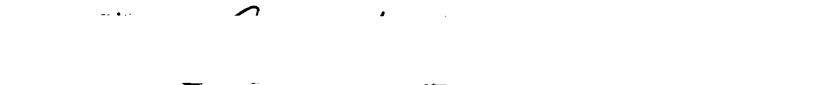
at the

**Massachusetts Institute of Technology**


June, 1997

© 1997 Massachusetts Institute of Technology


Signature of Author

  
Department of Mechanical Engineering  
May 9, 1997

Certified By

  
Steven Dubowsky  
Thesis Supervisor

Accepted By

  
Ain A. Sonin  
Chairman, Departmental Graduate Committee

MASSACHUSETTS INSTITUTE  
OF TECHNOLOGY

JUL 21 1997 Eng



## Acknowledgements

I would like to thank Professor Steven Dubowsky for his guidance and technical assistance during the past two years. I'd also like to thank the past and present members of the lab, especially Guillaume Morel and Guangjun Liu, for their technical contributions to this work.

I would like to recognize the National Science Foundation and the Korean Electric Power Company for providing financial support for this work.

Finally, thanks to my parents. And thanks to my sister, for all the chicken.

# Table of Contents

<b>1 Introduction</b>	
1.1 Background and Literature Review.....	9
1.2 Purpose of this Thesis.....	11
1.3 Outline of Thesis.....	12
<b>2 Manipulator Fine-Motion Position Control</b>	
2.1 Introduction.....	14
2.2 Fine-Motion Position Control Theory.....	14
2.2.1 Torque Feedback Linear Analysis.....	15
2.2.2 Generalized Torque Estimation Equations.....	17
2.2.3 Simplified Torque Estimation Equations.....	20
2.3 Fine-Motion Position Control Simulation.....	21
2.3.1 Governing Equations and Controller Design for PUMA 550 System.....	22
2.3.2 Simulation Results for PUMA 550 System.....	24
2.4 Fine-Motion Position Control Experimentation.....	31
2.4.1 Governing Equations and Controller Design for Schilling Titan II System.....	31
2.4.2 Experimental Results for Schilling Titan II System.....	33
2.5 Summary and Conclusions.....	40
<b>3 Manipulator Force Control</b>	
3.1 Introduction.....	41
3.2 Force Control Simulation.....	41
3.3 Force Control Experimentation.....	44
3.4 Torque Control.....	45
3.4.1 Torque Control Theory.....	45
3.4.2 Torque Control Simulation Results.....	48

3.4.3	Torque Control Experimental Results.....	51
3.5	Implicit Force Control.....	54
3.5.1	Implicit Force Control Theory.....	55
3.5.2	Implicit Force Control Simulation Results.....	57
3.5.3	Implicit Force Control Experimental Results.....	59
3.6	Summary and Conclusions.....	63
<b>4</b>	<b>Manipulator Identification</b>	
4.1	Introduction.....	65
4.2	Manipulator Mass Parameter Identification.....	65
4.2.1	Mass Parameter Identification Theory.....	67
4.2.2	Mass Parameter Identification Experimentation.....	70
4.3	Manipulator Inertial Parameter Identification.....	74
4.3.1	Inertial Parameter Identification Theory.....	76
4.3.2	Inertial Parameter Identification Experimentation.....	82
4.4	Summary and Conclusions.....	89
<b>5</b>	<b>Conclusions and Suggestions for Further Work</b>	
5.1	Contributions of This Work.....	90
5.2	Suggestions for Further Work.....	91
	<b>References</b>	
	<b>Appendix</b>	
A	PUMA 550 Kinematic Description.....	98
B	Base Force/Torque Sensor Calibration Procedure.....	99
C	Complete Inertial Parameter Matrix for a PUMA 550.....	104

## List of Figures

Figure 2.1	Single Joint Manipulator with PD Controller.....	15
Figure 2.2	Single Joint Manipulator with PD Controller and Torque Feedback.....	16
Figure 2.3	Generalized Manipulator Mounted on a Base Force/Torque Sensor.....	18
Figure 2.4	Body-Fixed Coordinate Frames for a Generalized Link $i$ .....	19
Figure 2.5	A PUMA 550 Manipulator with Coordinate Frames Attached.....	21
Figure 2.6	Joint Friction Model.....	22
Figure 2.7	Position Control System Architecture.....	24
Figure 2.8	Joint One Torque Control Simulation.....	25
Figure 2.9	Joint One Torque Control Experiment.....	26
Figure 2.10	Joint One Simulated Triangular Wave Tracking.....	27
Figure 2.11	Joint One Simulated Triangular Wave Tracking Error.....	27
Figure 2.12	Joint One Experimental Triangular Wave Tracking.....	28
Figure 2.13	Simulated Cartesian Space Tracking.....	30
Figure 2.14	Experimental Cartesian Space Tracking.....	30
Figure 2.15	Schilling Titan II Dimensions.....	32
Figure 2.16	Control System Architecture.....	32
Figure 2.17	Schilling Titan II Coordinate Frames.....	34
Figure 2.18	Joint Three Triangular Wave Tracking.....	35
Figure 2.19	Joint Three Triangular Wave Tracking Error.....	35
Figure 2.20	Joint Three Triangular Wave Tracking.....	36
Figure 2.21	Joint Three Triangular Wave Tracking Error.....	37

Figure 2.22	Cartesian Space Tracking.....	38
Figure 2.23	Joint Three Tracking with Payload.....	40
Figure 3.1	Simulated Base-Sensor Interaction Force Measurement.....	42
Figure 3.2	Force Control Experimental Setup.....	43
Figure 3.3	Single Joint Model with Frictional Disturbance.....	44
Figure 3.4	Single Joint with Frictional Disturbance Under Integral Control.....	45
Figure 3.5	Integral Compensator Disturbance Rejection Properties.....	46
Figure 3.6	Torque Control System Architecture.....	47
Figure 3.7	Torque Control Simulation—Pure Integral Control.....	48
Figure 3.8	Torque Control Simulation—Integral Control with Damping.....	49
Figure 3.9	Torque Control Simulation—Integral Control with Dominant Pole.....	50
Figure 3.10	Torque Control Experimentation—Pure Integral Control.....	51
Figure 3.11	Torque Control Experimentation—Integral Control with Damping.....	52
Figure 3.12	Torque Control Simulation—Integral Control with Dominant Pole.....	53
Figure 3.13	Force Control Environment Interaction Model.....	54
Figure 3.14	Implicit Force Control System Architecture.....	56
Figure 3.15	Implicit Force Control Simulation Results—PD Control.....	57
Figure 3.16	Implicit Force Control Position Trajectory—PD Control with Torque Feedback.....	58
Figure 3.17	Implicit Force Control Simulation Results—PD Control with Torque Feedback.....	59
Figure 3.18	Implicit Force Control Desired Position Trajectory—PD Control.....	60

Figure 3.19	Implicit Force Control Experimental Results—PD Control.....	60
Figure 3.20	Implicit Force Control Position Trajectory—PD Control with Torque Feedback.....	61
Figure 3.21	Implicit Force Control Experimental Results—PD Control with Torque Feedback.....	62
Figure 3.22	Implicit Force Control Experimental Results—PD Control with Torque Feedback.....	63
Figure 4.1	A One Degree-Of-Freedom Static Manipulator.....	66
Figure 4.2	Comparison of Measured and Computed $M_x$ and $M_y$ .....	73
Figure 4.3	Error Between Measured and Computed $M_x$ and $M_y$ .....	73
Figure 4.4	A One Degree-Of-Freedom Dynamic Manipulator.....	76
Figure 4.5	Excitation Trajectory—Joint One.....	84
Figure 4.6	Excitation Trajectory—Joint Two.....	85
Figure 4.7	Verification Trajectory—Joint One.....	86
Figure 4.8	Verification Trajectory—Joint Two.....	87
Figure 4.9	Comparison of Predicted and Measured Forces and Torques.....	88
Figure B.1	Application of Moments: $M_x$ Direction (PUMA Robot Hidden).....	102
Figure B.2	Application of $M_x$ Moment and $F_x$ Force (PUMA Robot Hidden).....	102



# Chapter 1

## Introduction

### 1.1 Background and Literature Review

Many applications of industrial manipulators require accurate control of position during small, slow motions, and accurate control of small forces. It is difficult to achieve high precision during these “fine motions” due to nonlinear joint friction, which can lead to stick-slip behavior, static positioning errors, or limit cycle oscillations. There are several existing approaches for improving fine motion manipulator performance. However, they are hampered by one of the following factors. They require complex modeling of frictional behavior (Popovic *et al.*, 1994; Canudas de Wit *et al.*, 1996). They can require the use of specially designed joint-torque sensors, which are costly, complex, and have limited accuracy (Pfeffer *et al.*, 1989; Vischer and Khatib, 1995). Finally, some methods have been proposed that control only finite displacements, ignoring the trajectory tracking problem and thus making it difficult to produce smooth, slow motions (Popovic *et al.*, 1995). A more complete discussion of friction compensation techniques can be found in (Morel and Dubowsky, 1996).

A simple control scheme which overcomes the above limitations has been developed and demonstrated on an electrical industrial robot (Morel and Dubowsky, 1996). This method utilizes feedback from a six-axis force/torque sensor mounted at the base of the manipulator, which is used to estimate the torque at each joint of the manipulator. The estimation process is based on Newton-Euler equations of successive rigid bodies. With an

estimation of the joint torque, accurate joint torque control is possible. This leads to improved friction compensation, which in turn allows the execution of fine-motion positioning tasks. This method is attractive because of the simplicity of its implementation and excellent performance. It does not require models of the actuator characteristics or joint friction, nor does it require the manipulator to be retrofitted with expensive and difficult to implement joint-torque sensors.

A first main purpose of the research described in this thesis was to apply this method to a hydraulic manipulator. This is a challenging application due to the very high joint friction present in such manipulators. The second purpose was to extend the methodology to force control. Finally, manipulator identification and sensor calibration techniques were investigated as extensions of the use of a base-mounted force/torque sensor.

There is little discussion in the literature of fine motion control as applied to hydraulic manipulators. Hydraulic manipulators are frequently used in industrial applications requiring the manipulation of heavy payloads and the application of large forces. Such tasks are common in nuclear maintenance, undersea, and field applications (Dubowsky, 1996). Hydraulic robots are attractive due to their high load carrying capacity (relative to typical electric motor-driven robots), but are often difficult to control due to high joint friction and actuator nonlinearities (Merritt, 1967).

One recent position control method utilizes a nonlinear PI controller, with the integral term modified to include a term which is designed to detect the onset of stiction (Heinrichs *et al.*, 1996). This method is attractive due to its ease of implementation. However, the authors reported that performance was poorest for fine motions, where friction effects have large influence.

Manipulator force control has been studied by many researchers over the past twenty years (Whitney, 1987). It is well known that accurate control of joint torques leads to improved force control performance (Asada and Youcef-Toumi, 1987; An, 1988). Feedback from the base force/torque sensor

can be used for this purpose. This leads to improved performance under two types of force control: torque control, and implicit force control.

Manipulator identification has been studied by many researchers in recent years, due to its important role in model formulation (An *et al.*, 1985; Khosla and Kanade, 1985; Armstrong *et al.*, 1986). Most methods are based on the solution of a series of equations relating joint torque to joint motion. However, since most manipulators are not equipped with joint torque sensors, an estimate of the joint torque which is derived from a measurement of the motor current is used. This estimated value is degraded by the presence of unmodeled joint friction and actuator dynamics.

## 1.2 Purpose of this Thesis

Previous work in fine-motion control using a base force/torque sensor has been limited to the position control of an electrically-driven manipulator (Morel and Dubowsky, 1996). As discussed above, the focus of this work is to evaluate applications of the base force/torque sensor method to the fine-motion control of a hydraulic manipulator, force control of an electrically-driven manipulator, and parameter identification of an electrically-driven manipulator.

In this thesis, theoretical methods of joint-torque estimation are reviewed. It is then shown that if dynamic terms of the joint-torque estimation equations are neglected and gravity torque is assumed to be constant, the estimation equations become a series of computationally very simple static transformations. A simulation which utilizes this highly simplified form of the algorithm predicts improved performance during fine-motion tasks for an electrically-driven manipulator. These results support experimental results, proving the efficacy of the simulation (Morel and Dubowsky, 1996).

The method is then applied to a hydraulic manipulator with nonlinear actuators and very high joint friction. Experimental results clearly demonstrate that excellent tracking performance during fine motion tasks is

achievable even with the simplified form of the algorithm. Results are also presented for tasks requiring the fine positioning of heavy payloads. Again, the experimental results show improved performance over conventional (i.e. PD) control schemes.

Two force control methods are then examined in theory, simulation, and experimentation. Base force/torque sensor feedback is again used to estimate joint torques, and performance improvements are shown relative to a system without torque feedback. It is shown that high resolution force control is attainable on an electrical experimental system.

Finally, a novel method for identifying manipulator mass and inertial parameters is presented. Previous work with the base sensor in this area has been limited to the estimation of mass parameters (West *et al.*, 1989). Experimental results for a similar method of mass parameter identification is presented. Theory and experimental results are then presented for a novel inertial parameter identification scheme. Unlike most identification methods which estimate joint torque from a measurement of the motor current, the method exploits feedback from the base force/torque sensor and thus is not influenced by joint friction or actuator dynamics. The method does not require measurement of the joint acceleration, but only the joint velocity. It is shown that accurate mass and inertial parameter identification is possible on an experimental system.

### **1.3 Outline of Thesis**

This thesis is divided into five chapters. This chapter serves as an introduction and overview of the work. Chapter 2 introduces the base force/torque sensor method as applied to the fine-motion positioning problem. Simulation results are presented for an electrically-driven manipulator and are compared to results from an experimental system. Finally, experimental results are presented for a hydraulic system.

Chapter 3 gives an introduction to the force control problem, and provides a brief review of recent research in the field. It describes two general

methods of force control: torque control, and implicit force control. Each method is modified to utilize base-sensor feedback. Simulation and experimental results are presented for each method.

Chapter 4 introduces manipulator identification. Conventional methods for parameter identification are briefly reviewed, and a method for identifying manipulator mass parameters is presented. Experimental results show that the method is capable of high-accuracy parameter estimation. A method for dynamic identification which utilizes base-sensor feedback is then described. Experimental results are presented which confirm the validity of the method.

Chapter 5 outlines general conclusions regarding the use of the base force/torque sensor, and presents suggestions for further work.

The appendices to this thesis give detailed information on specific topics related to the practical implementation of the proposed methods. Appendix A provides a kinematic description of the PUMA 550 manipulator. Appendix B describes a calibration procedure for base-mounted force/torque sensors. Appendix C provides the detailed equations for inertial parameter estimation of the first two joints of a PUMA 550 manipulator.

## Chapter 2

# Manipulator Fine-Motion Position Control

### 2.1 Introduction

This chapter describes simulation and experimental studies of fine-motion position control of a PUMA 550 and a Schilling Titan II manipulator. Section 2.2 presents the theoretical framework for the base force/torque sensor method, and discusses important simplifications that can be made for the fine-motion case. Section 2.3 contains simulation results for a PUMA 550 manipulator executing fine-motion tasks and compares them to experimental results. Section 2.4 presents experimental results for the Schilling Titan II system, for unloaded free motion tasks, and free motion tasks with a payload.

### 2.2 Fine-Motion Position Control Theory

To obtain good performance during fine-motion positioning tasks, it is essential to compensate for joint-level disturbances, such as friction. Our approach to friction compensation is based on torque feedback. To understand the benefit of torque feedback in position control, it is worthwhile to examine a simple linear model of a single joint manipulator. With an analytical understanding of the benefits of torque feedback, the problem of torque estimation can then be addressed. The generalized dynamic torque estimation equations used in the base force/torque sensor method were originally presented in (Morel and Dubowsky, 1996). Here, we review these equations, and present a simplified version of them. Through simulation

and experimentation, the simplified equations are shown to be sufficient and effective for fine-motion control.

### 2.2.1 Torque Feedback Linear Analysis

Consider a single-joint DC motor-driven manipulator, shown in Figure 2.1. This joint is controlled by a PD controller, and subject to a torque disturbance,  $\tau_d$ .

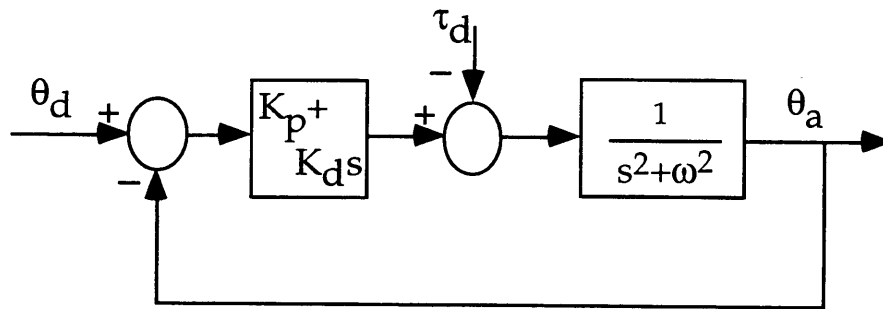


Figure 2.1: Single Joint Manipulator with PD Controller

We are interested in examining the system positioning performance with respect to joint-level disturbances, such as friction. Thus, we write the system transfer function, paying particular attention to the transfer function from  $\theta_a$  to  $\tau_d$ .

$$\theta_a = \frac{K_p + K_d s}{s^2 + K_d s + K_p + \omega^2} \theta_d - \frac{1}{s^2 + K_d s + K_p + \omega^2} \tau_d \quad (2.1)$$

And:

$$\frac{\theta_a}{\tau_d} = -\frac{1}{s^2 + K_d s + K_p + \omega^2} \quad (2.2)$$

For a unit-step torque disturbance, the asymptotic output will be:

$$\theta_a(\infty) = -\frac{1}{K_p + \omega^2}$$

We see that the system is incapable of rejecting the torque disturbance, and a steady-state positioning error results. Increasing the  $K_p$  gain of the

compensator will reduce this gain, but stability issues limit the effectiveness of this solution.

We now consider a similar system, modified to include an integral-type compensator acting on a torque feedback loop. This system is shown in Figure 2.2.

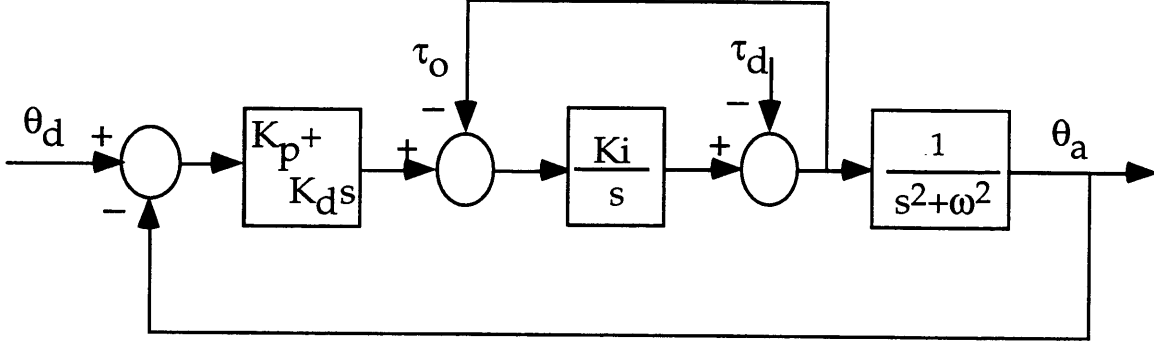


Figure 2.2: Single Joint Manipulator with PD Controller and Torque Feedback

Again, we are interested in examining the system positioning performance with respect to joint-level disturbances. Thus, we again write the system transfer function, again paying attention to the transfer function from  $\theta_a$  to  $\tau_d$ .

$$\theta_a = \frac{(K_d K_i)s + K_p K_i}{s^3 + (\omega^2 + K_d K_i)s + K_p K_i} \theta_d - \frac{K_i s}{s^3 + (\omega^2 + K_d K_i)s + K_p K_i} \tau_o - \frac{s}{s^3 + (\omega^2 + K_d K_i)s + K_p K_i} \tau_d \quad (2.3)$$

And:

$$\frac{\theta_a}{\tau_d} = -\frac{s}{s^3 + (\omega^2 + K_d K_i)s + K_p K_i} \quad (2.4)$$

For a unit-step torque disturbance, the asymptotic output will be:

$$\theta_a(\infty) = 0$$



From this simple analysis, we see that the system rejects the torque disturbance in finite time, and no steady-state positioning error results. The addition of an integral term in the critical path should add phase lag to the system. However, for slow motions the effects of this additional lag should be negligible.

### 2.2.2 Generalized Torque Estimation Equations

The preceding analysis assumed “perfect” torque feedback (i.e. the actual joint torque was read by an ideal sensor with no noise or measurement error). In reality, joint torque is difficult to measure, and as a consequence most manipulators are not equipped with joint torque sensors. Here, we develop equations for estimating joint torque from a measured wrench at the base of the manipulator (Morel and Dubowsky, 1996).

In the general case, the wrench,  $W_b$ , exerted by the manipulator shown in Figure 2.3 on its base sensor can be expressed as the sum of two components:

$$W_b = W_g + W_d \quad (2.5)$$

where  $W_g$  is the gravity component, and  $W_d$  is the component caused by manipulator dynamic motion. Note that the base sensor measures forces and torques corresponding to joint torques that are effectively transmitted to the manipulators links. Thus, friction does not appear in the measured wrench.

Since we are interested in eventually obtaining equations relating the base wrench to manipulator motion, it is desirable to eliminate the wrench component that is caused by gravity. The gravity wrench can be compensated for using the following model (West *et al.*, 1989; Baker, 1992) :

$$W_d = W_b - W_g = W_b - \left( \begin{array}{l} F_g = \sum_{i=1}^n m_i g \\ M_g^{O_s} = \sum_{i=1}^n O_s G_i \times m_i g \end{array} \right) \quad (2.6)$$

where  $F_g$  and  $M_g^{O_s}$  are the gravity force and moment at the center of the sensor  $O_s$ , respectively,  $m_i$  and  $G_i$  are the mass and the location of the center of mass of link  $i$ , respectively.

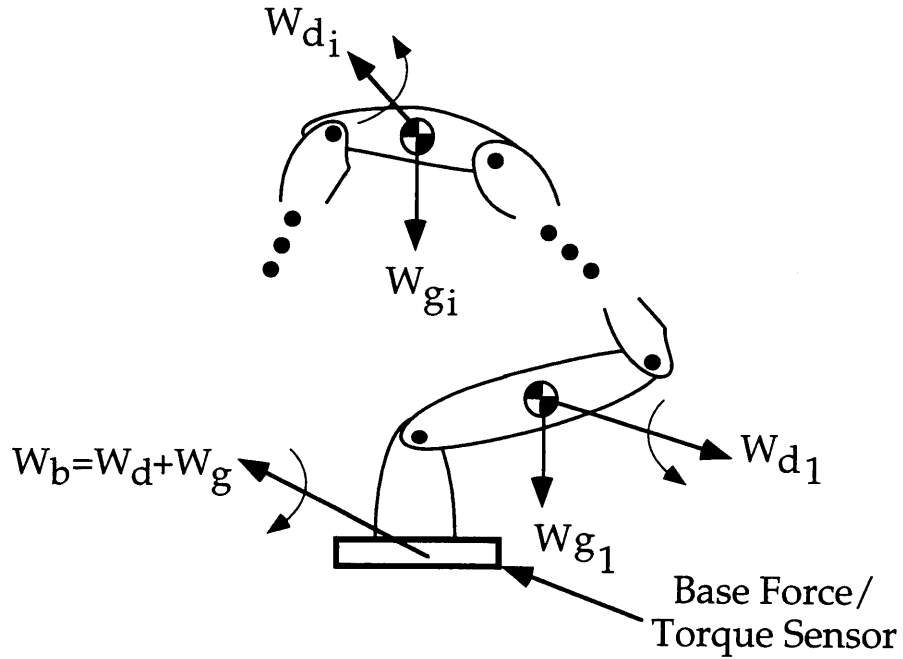


Figure 2.3: Generalized Manipulator Mounted on a Base Force/Torque Sensor

Assuming accurate gravity compensation, the Newton-Euler equations of the first  $i$  links are:

$$\begin{cases} W_{0 \rightarrow 1} = -W_{\text{base}} \\ W_{1 \rightarrow 2} = W_{0 \rightarrow 1} - W_{\text{dyn}_1} \\ \vdots \\ \vdots \\ W_{i \rightarrow i+1} = W_{i-1 \rightarrow i} - W_{\text{dyn}_i} \end{cases} \quad (2.7)$$

where  $W_{i \rightarrow i+1}$  is the wrench exerted by the link  $i$  on the link  $i+1$  and  $W_{\text{dyn}_i}$  is the dynamic wrench corresponding to link  $i$ . The  $W_{\text{dyn}_i}$  term can be expressed at any point A in terms of the acceleration  $\dot{V}_{G_i}$  of  $G_i$ , the angular acceleration  $\dot{\omega}_i$  and the angular velocity  $\omega_i$ :

$$\mathbf{W}_{\text{dyn}_i} = \begin{pmatrix} \mathbf{F}_{\text{dyn}_i} = m_i \dot{\mathbf{V}}_{G_i} \\ \mathbf{M}_{\text{dyn}_i}^A = I_i \dot{\boldsymbol{\omega}}_i + \boldsymbol{\omega}_i \times I_i \boldsymbol{\omega}_i + G_i A \times m_i \dot{\mathbf{V}}_{G_i} \end{pmatrix} \quad (2.8)$$

The torque at joint  $i+1$  is obtained by projecting the moment vector at  $O_i$  along  $z_i$  (see Figure 2.4) :

$$\tau_{i+1} = -z_i^t \left[ \mathbf{M}_d^{O_i} + \sum_{j=1}^i \left( I_j \dot{\boldsymbol{\omega}}_j + \boldsymbol{\omega}_j \times I_j \boldsymbol{\omega}_j + O_i G_j \times m_j \dot{\mathbf{V}}_{G_j} \right) \right] \quad (2.9)$$

Where  $M_d$  is the dynamic moment component of the base wrench.

Analysis of this equation shows that for joints nearest to the base sensor with orthogonal axes of rotation, we can write torque estimation equations that depend only on the measured base wrench. However, for distal joints that have axes of rotation that are non-orthogonal to the axes of rotation of proximal links, dynamic terms must be included in the torque estimation equations. This requires knowledge of joint acceleration, which is difficult to measure in practice.

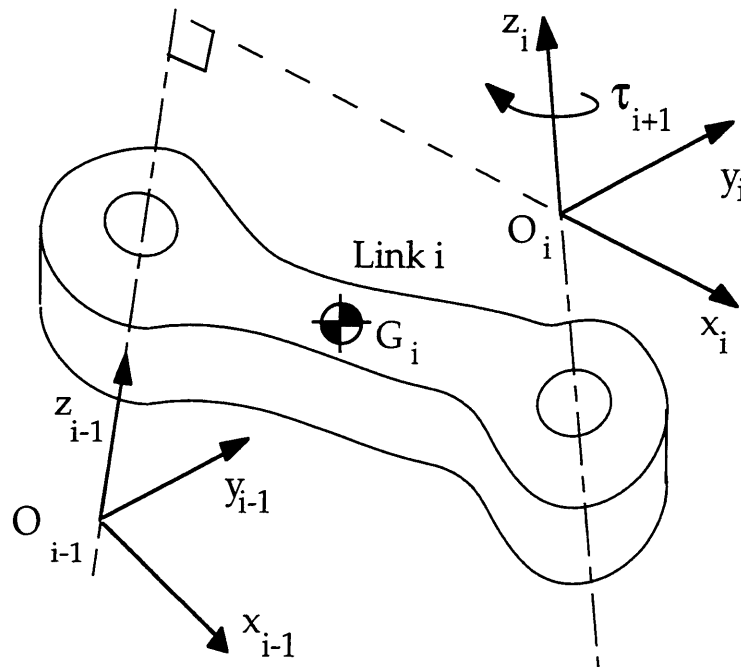


Figure 2.4: Body-Fixed Coordinate Frames for a Generalized Link  $i$

### 2.2.3 Simplified Torque Estimation Equations

In the general algorithm, the gravity wrench is computed for every manipulator configuration along a trajectory. In the fine-motion case, however, it is assumed that since the manipulator range of motion is small, the gravity wrench is nearly constant. Thus, we can set it equal to the static wrench measured by the base sensor immediately before motion. In this way, the complexity related to computing the gravitational wrench, such as identification of link weights and a static manipulator model, is eliminated. If the joints of the manipulator move just a few degrees, it can be shown that the errors in the gravitational terms are only a few percent.

For the fine-motion case, it is also assumed that the manipulator moves very slowly. In this case,  $W_{\text{dyn}}$  terms will generally be negligible. Hence, dynamic terms are treated as a disturbance. As a result, for slow, fine motions, only the measured wrench at the base is used to estimate the torque in joint  $i+1$ . The torque is estimated by projecting the base wrench at  $O_i$ ,  $W_{\text{base}}^{O_i}$ , along  $z_i$  (see Figure 2.4). This leads to the equation:

$$\tau_{i+1} = -z_i^t \cdot W_{\text{base}}^{O_i} \quad (2.10)$$

This equation can be written as,

$$\tau = A(q) \cdot W_{\text{base}}^{O_i} \quad (2.11)$$

Thus the estimated torque is computed via a static transformation from the manipulator base to joint  $i$ . The method does not depend on measurements (or estimations) of the joint velocities or accelerations, estimates or models of masses or inertias of the links or payload, or models of the actuator dynamics or friction, but only on joint positions, and the manipulator's kinematic parameters.

### 2.3 Fine-Motion Position Control Simulation

A three degree-of-freedom (d.o.f.) simulation of a PUMA 550 manipulator was formulated in Matlab to predict performance during fine motions under base force/torque sensor control. The PUMA 550 is a five d.o.f. industrial electrically-driven manipulator, shown in Figure 2.5 (refer to Appendix A for complete kinematic description). Many researchers have studied this system, and thus mass and inertial parameters are available in the literature (Corke, 1984, Armstrong *et al.*, 1986). To simulate the base sensor measurement, manipulator equations of motion were written with respect to the sensor frame.

Several simplifications were made. The first was that gravity compensation was assumed to be perfect. Sensor compliance was not considered, and neither were the effects of sensor noise. These simplifications were deemed reasonable, especially for the fine-motion case. However, encoder digital effects were considered significant for low-velocity motion, and were included in the simulation.

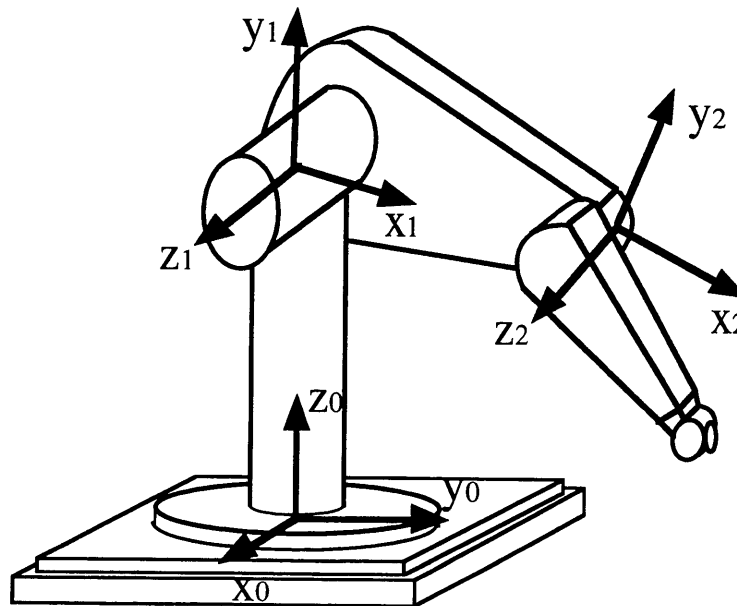


Figure 2.5: A PUMA 550 Manipulator with Coordinate Frames Attached

An important component of the simulation was the friction model. Previous researchers have characterized the type of friction present in a PUMA manipulator (Armstrong, 1991; Canudas de Wit *et al.*, 1996). This curve captures the nonlinear behavior of friction at low-speeds. A Lorentzian friction model was employed to compute the frictional torque  $F$ , which takes the following form (Armstrong, 1991):

$$F(\dot{\theta}) = 5.05 + 4.94\dot{\theta} + 1.30 \frac{1}{1 + (\dot{\theta}/0.0058)^2} + 0.466 \frac{1}{1 + (\dot{\theta}/0.068)^2} \quad (2.12)$$

The sign of this frictional torque is assumed to be opposite that of the direction of motion. Figure 2.6 is a plot of the friction model. Note that the stick-slip (negative-sloping) regime ranges from zero velocity to approximately 1 degree per second.

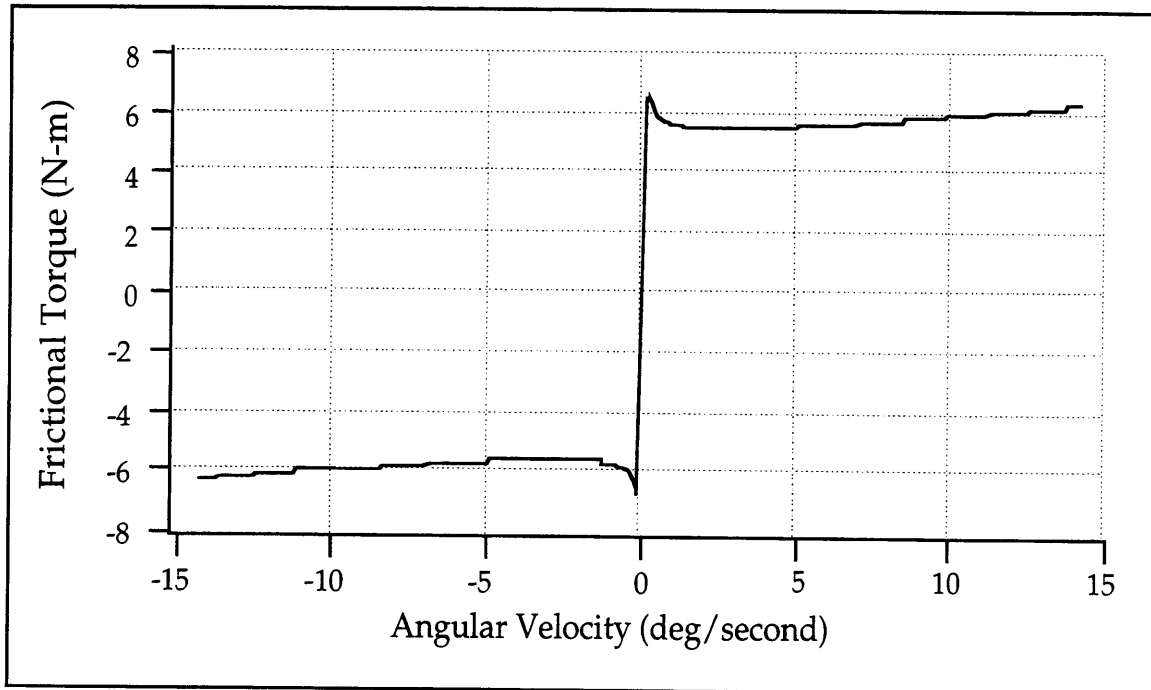


Figure 2.6: Joint Friction Model

### 2.3.1 Governing Equations and Controller Design for PUMA 550 System

The position control scheme consists of an inner torque loop and an outer position loop, as shown in Figure 2.7. During fine motions, the frictional torque of the PUMA 550 is often larger than the dynamic torque

applied to the joint. With this in mind, a high DC gain is required in the torque controller. Several researchers have studied the performance of various types of torque controllers (Volpe and Khosla, 1992; Vischer and Khatib, 1995). An integral compensator achieves low-pass filtering and zero steady-state error, which is desirable. A proportional compensator could introduce instability, and a derivative compensator is ineffective and difficult to implement on a real system due to noise issue. Previous studies also suggests that a feedforward compensator should not be used in conjunction with integral control, but experimental work shows improvement in the torque control performance when a feedforward term is used.

The torque control law was chosen as follows:

$$\tau_{\text{out}} = \tau_{\text{des}} + K_{\text{int}} \int_0^t (\tau_{\text{des}} - \tau_{\text{est}}) \quad (2.13)$$

Where  $\tau_{\text{des}}$  and  $\tau_{\text{est}}$  are the desired and estimated (i.e. base-sensed) torques, respectively. The control gain  $K_{\text{int}}$  was tuned to 75% of the value that caused instability in the simulation.

The inner torque loop serves to eliminate friction at the manipulator joints. With a “frictionless” manipulator, excellent positioning performance can be achieved without the use of complex control algorithms. A simple PD controller is sufficient for the outer loop compensator. The final position control law was as follows:

$$\tau_{\text{out}} = \tau_{\text{des}} + K_{\text{int}} \int_0^t (\tau_{\text{des}} - \tau_{\text{est}}) \quad (2.14)$$

With:

$$\tau_{\text{des}} = K_p(\theta_d - \theta) + K_d(\dot{\theta}_d - \dot{\theta}) \quad (2.15)$$

Where  $K_p$  and  $K_d$  are diagonal gain matrices.

The simplified torque estimation equation, Equation 2.10, yields the following result when applied to the PUMA 550:

$$A(q) = \begin{pmatrix} 0 & 0 & 0 & 0 & 0 & -1 \\ 0 & 0 & 0 & -\sin(\theta_1) & \cos(\theta_1) & 0 \\ a_2 \sin(\theta_1) \cos(\theta_2) & -a_2 \sin(\theta_1) \sin(\theta_2) & -a_2 \cos(\theta_2) & -\sin(\theta_1) & \cos(\theta_1) & 0 \end{pmatrix} \quad (2.16)$$

For clarity, we can write explicitly:

$$\tau_1 = -M_{\text{base}}^Z \quad (2.17)$$

$$\tau_2 = -\sin(\theta_1)M_{\text{base}}^X + \cos(\theta_2)M_{\text{base}}^Y \quad (2.18)$$

$$\tau_3 = \tau_2 - a_2(-\cos(\theta_1)\sin(\theta_2)F_{\text{base}}^X + \sin(\theta_1)\sin(\theta_2)F_{\text{base}}^Y + \cos(\theta_2)F_{\text{base}}^Z) \quad (2.19)$$

Note that the torque estimation equations depend only on the manipulator joint positions, the measured base wrench, and the manipulator's kinematic parameters. These estimation equations are computationally very simple, and for the case of the PUMA requires knowledge of only a single kinematic parameter.

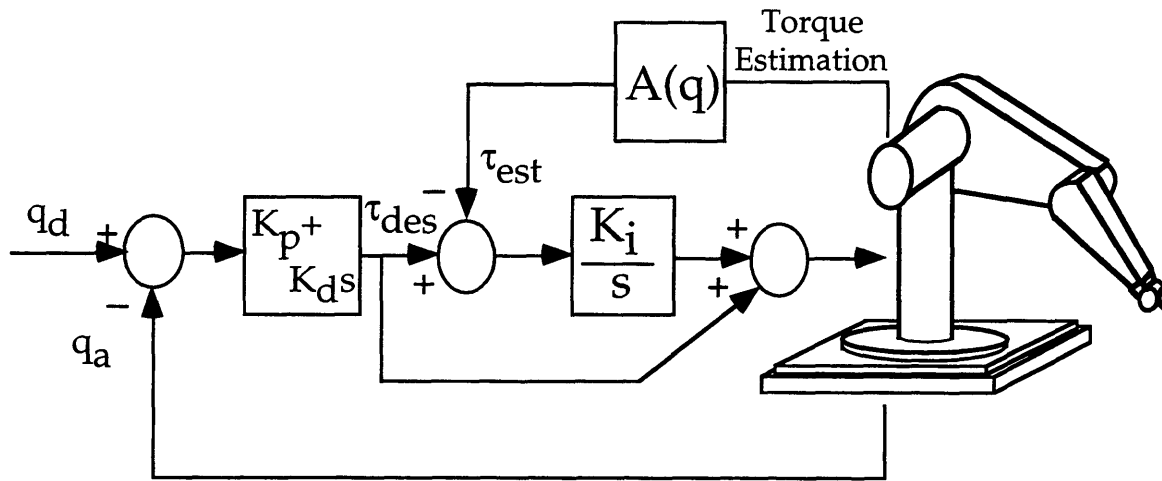


Figure 2.7: Position Control System Architecture

### 2.3.2 Simulation Results for PUMA 550 System

#### 1) Torque Control Results

As discussed in Section 2.3.1, an integral-type controller was used in the torque control loop. Equation 2.14 describes the control law which was used.



To evaluate the performance of the torque controller, we conducted simulated experiments which mirrored the real-world requirements of a torque controlled system. One such experiment is the tracking of a small amplitude triangular torque wave. The magnitude of the triangular wave was chosen such that its maximum value was less than the value of the simulated static friction (see Figure 2.6). The simulation was written for joint one of the PUMA 550.

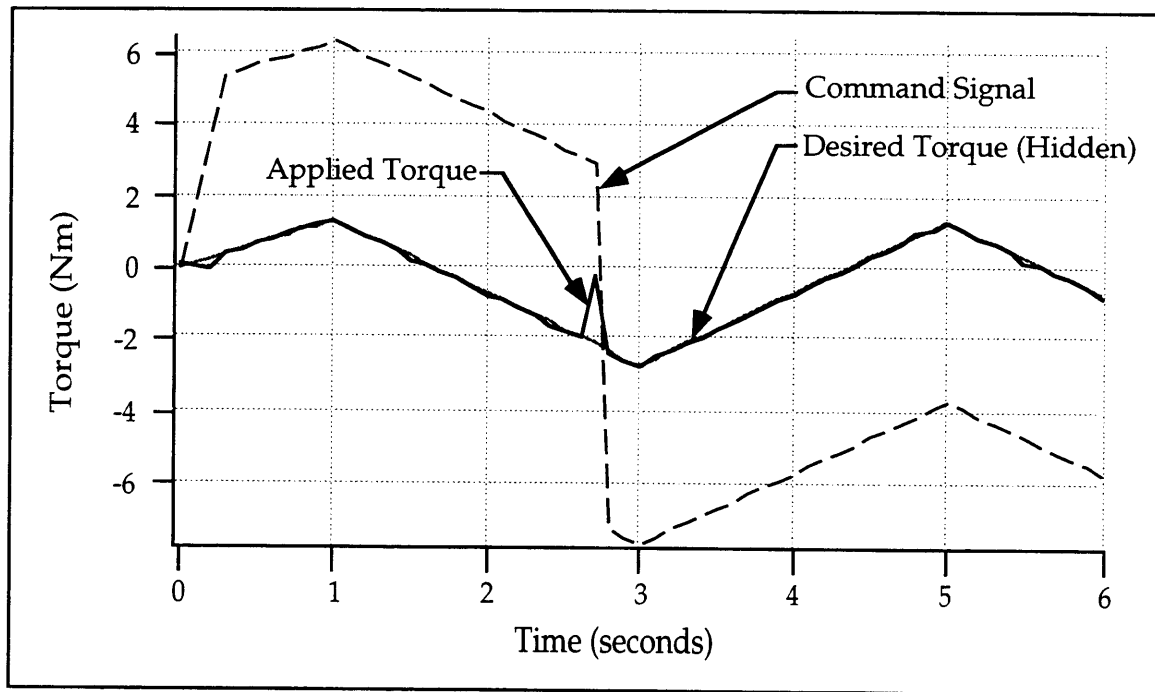


Figure 2.8: Joint One Torque Control Simulation

Figure 2.8 shows the response of the simulated system. The command signal (i.e. the signal sent to the DC motor) has a higher magnitude than the desired torque, in order to overcome friction. The simulated system tracks the desired torque accurately, with transient errors occurring at velocity sign changes, where frictional disturbances are largest.

Figure 2.9 shows the results of an experimental trial with the first joint of the PUMA 550. This result was obtained by Guillaume Morel and can be found in the literature (Morel and Dubowsky, 1996). Comparing this result to the simulation, it can be seen that the simulated manipulator tracks the desired torque at a slightly higher accuracy than that of the physical system.

The higher accuracy of the simulation is probably due to nonlinear disturbance forces, such as gear cogging and backlash, that were not included in the model. These effects, however, appeared to be small. It is clear that the simulation captures the dominant behavior of the physical system.

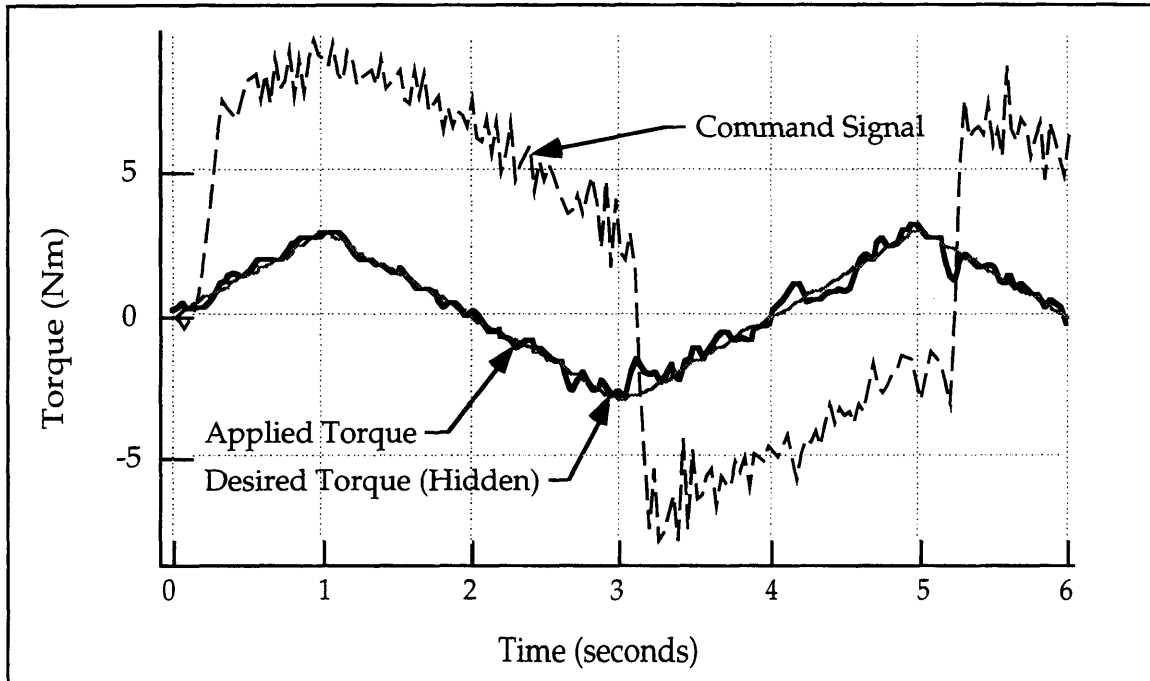


Figure 2.9: Joint One Torque Control Experiment

### II) Joint Space Position Control Results

To evaluate the performance of the closed-loop position control system, tracking of a 0.10 degree triangular wave was simulated. The average joint speed was approximately 0.08 degrees per second, which corresponds to the stick-slip regime of the friction model (see Figure 2.6). The simplified torque estimation equations (Equations 2.17 through 2.19) were used. Base-sensor control performance was compared to both PD and PID control. Controller gains were tuned on a trial-and-error basis.

As seen in Figures 2.10 and 2.11, the simulation predicts marked improvement of base-sensor control over PID and PD control. Tracking error

is significantly lower, and recovery time at velocity sign changes is greatly reduced.

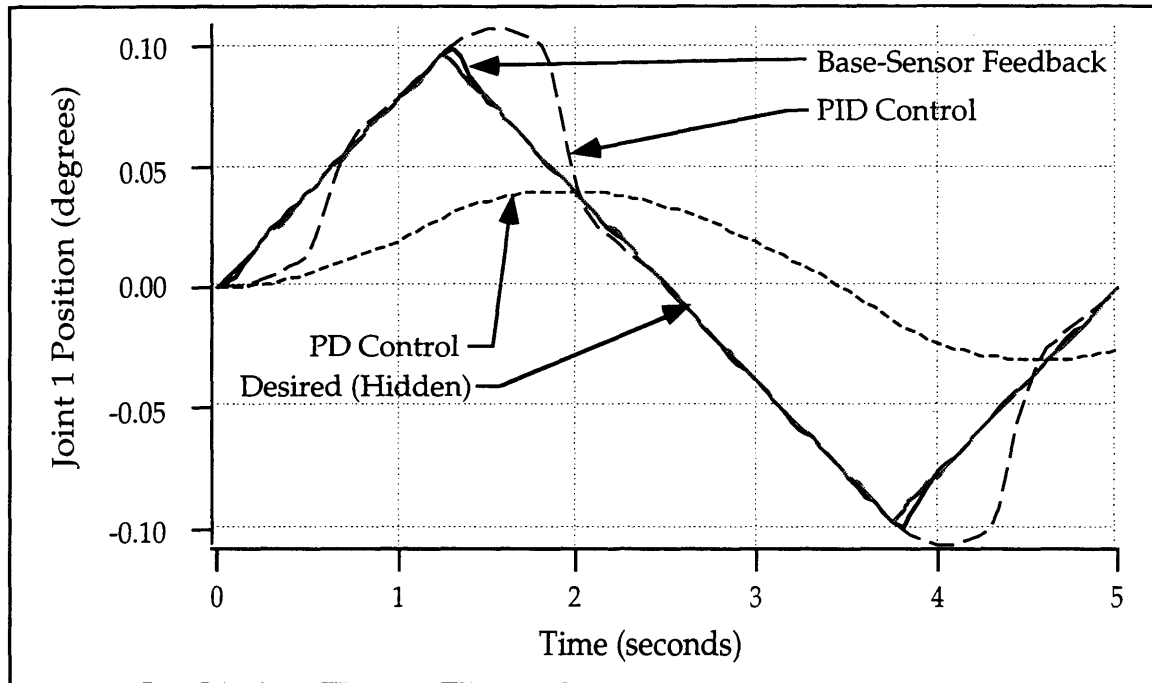


Figure 2.10: Joint One Simulated Triangular Wave Tracking

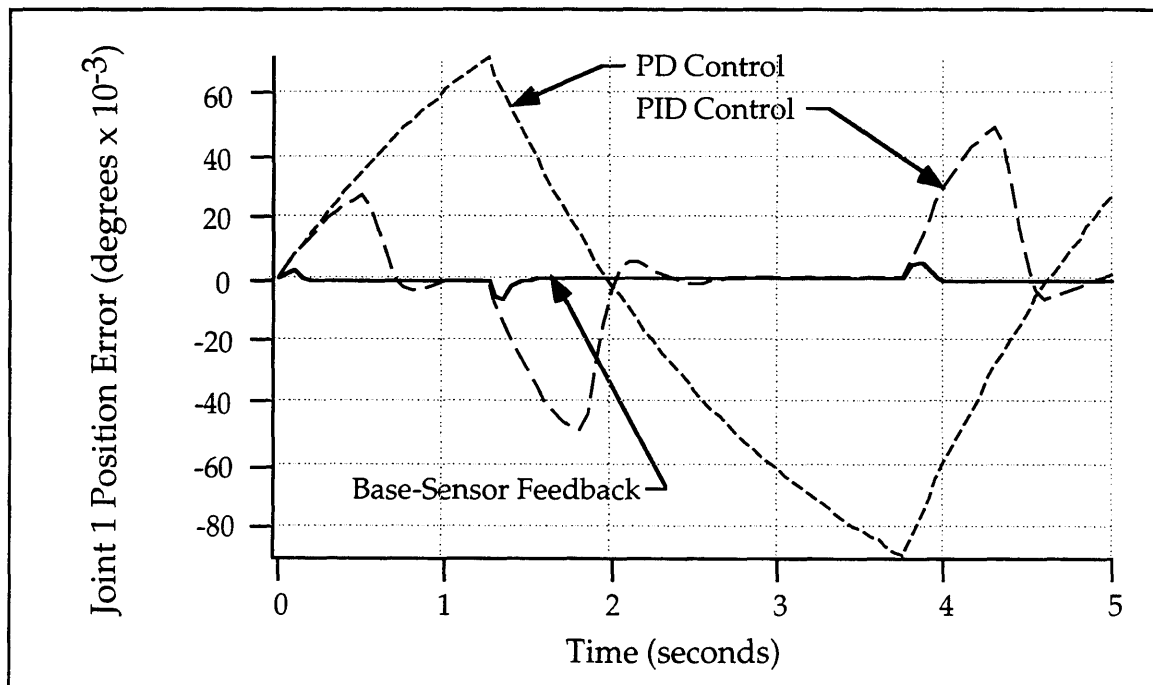


Figure 2.11: Joint One Simulated Triangular Wave Tracking Error

Comparing these results to experimental results obtained by Guillaume Morel in Figure 2.12, similarity in response shape and magnitude can be seen. This implies that the modeled frictional behavior and controller gains are similar to that of the experimental system.

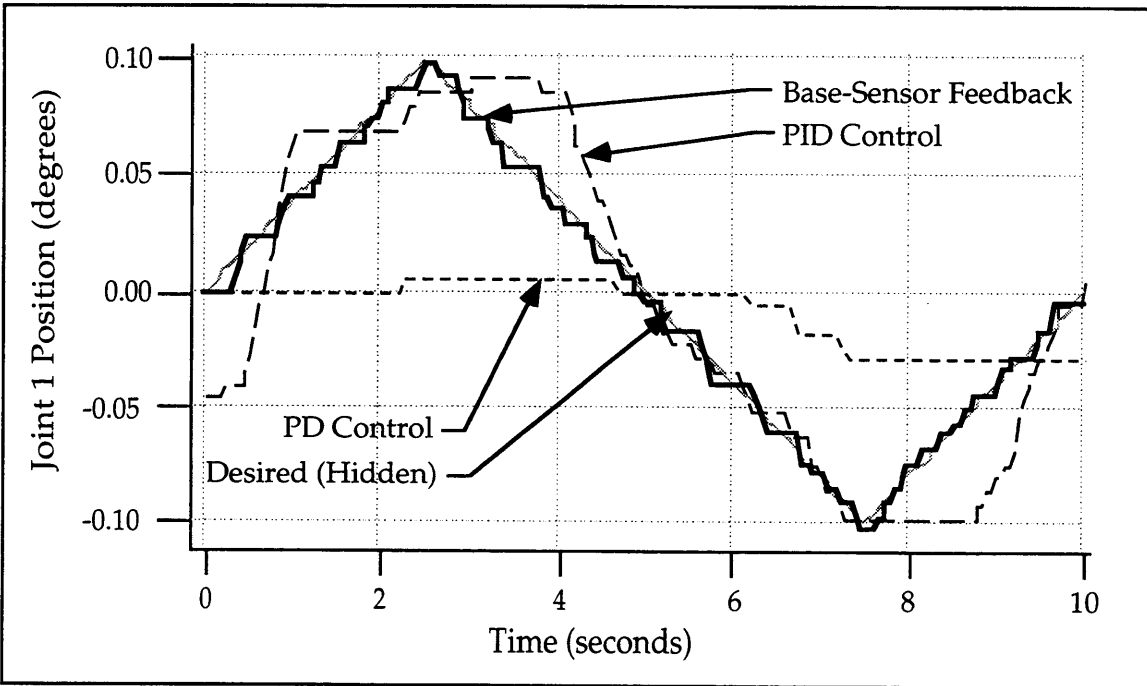


Figure 2.12: Joint One Experimental Triangular Wave Tracking

Table 2.1 compares the error of the three types of control for the simulated trajectory. The root-mean-square error of the base sensor feedback was 14.8 times better than in PID control, and 37.2 times better than PD control. The RMS error is approximately 0.0013 degrees throughout the task, which is less than the encoder resolution of 0.0058 degrees. These excellent simulation results are comparable to experimental results found in the literature (Morel and Dubowsky, 1996). These results are reprinted in Table 2.2. The experimental system displayed slightly poorer tracking accuracy, probably due to unmodeled effects such as gear cogging and backlash.

	RMS Error (degrees)	Maximum Error (degrees)
PD	0.0483	0.0891
PID	0.0193	0.0485
P + Base Sensor Feedback	0.0013	0.0062

Table 2.1: Summary of Simulated Error Results—Triangular Wave Tracking

	RMS Error (degrees)	Maximum Error (degrees)
PD	0.120	0.059
PID	0.056	0.020
P + Base Sensor Feedback	0.012	0.004

Table 2.2: Summary of Experimental Error Results—Triangular Wave Tracking

### *III) Cartesian Space Position Control Results*

A circular tracking task in cartesian space was selected. Inverse kinematic calculations were performed prior to the simulation, and the resulting joint space trajectories were commanded, under the same control scheme as the previous section.

Cartesian-space tasks require the coordinated motion of two joints. During this type of motion, we can examine the effects of disturbances on one joint resulting from motion of a different joint.

Again, the simulation predicts that base-sensor feedback control will greatly outperform PID control. Figure 2.13 shows that the simulation using PID control exhibits noticeable “squaring” of the circle. These square corners correspond to regions where the joint velocities are undergoing a sign change

(and thus the friction disturbance is large). Figure 2.14, taken from the literature, compares well with the simulated results (Morel and Dubowsky, 1996).

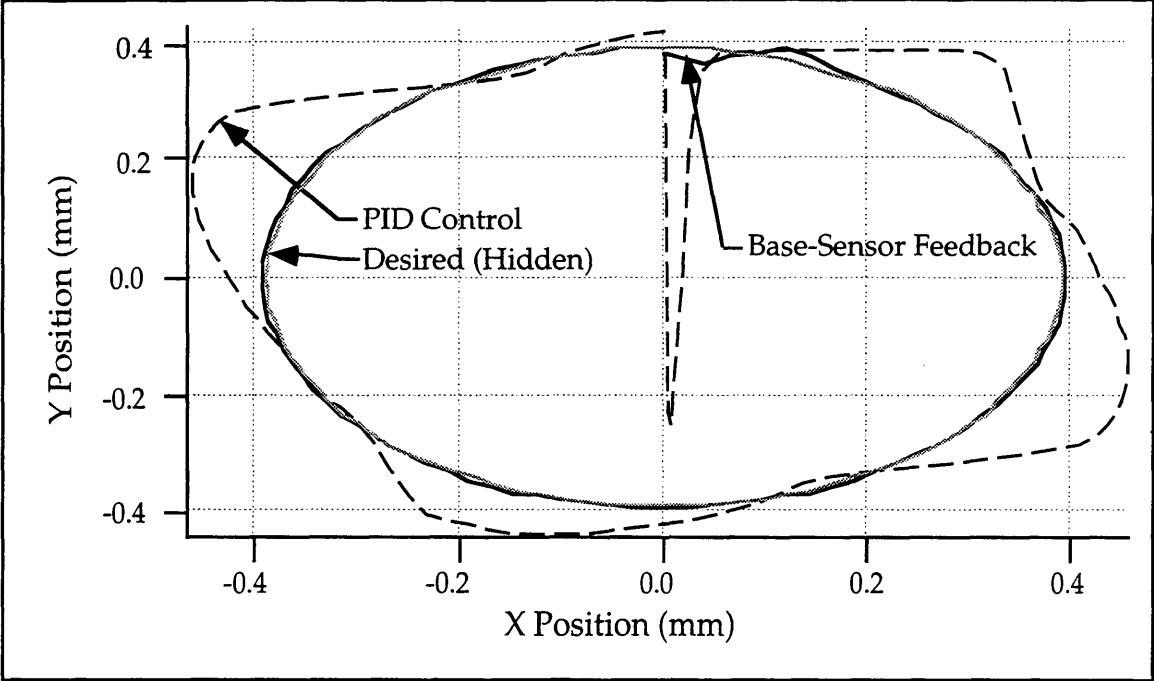


Figure 2.13: Simulated Cartesian Space Tracking

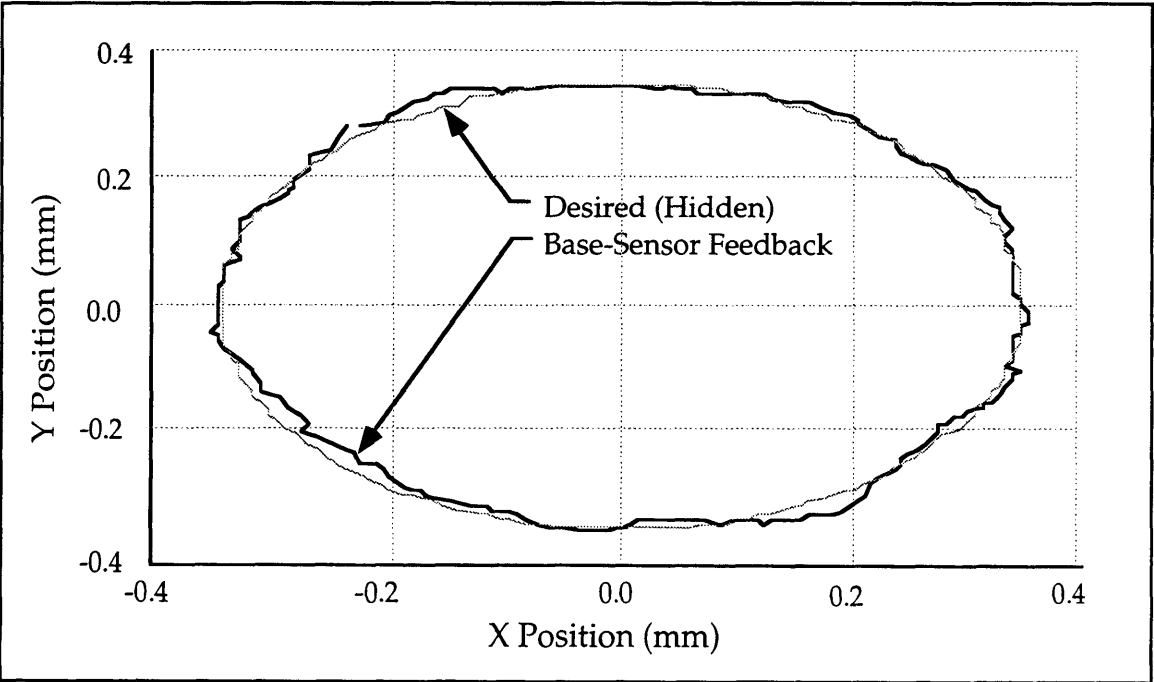


Figure 2.14: Experimental Cartesian Space Tracking

## 2.4 Fine-Motion Position Control Experimentation

Previous position control experiments have been performed on a PUMA 550 system (Morel and Dubowsky, 1996). In order to examine the effectiveness of the base sensor feedback method on a complex, highly nonlinear system, experiments were also conducted on a Schilling Titan II hydraulic manipulator. Development of governing equations and controller design proceeded in a manner similar to that for the PUMA 550 system. Experimental results were conducted for unloaded fine motions, cartesian-space fine motions, and for fine motions while supporting a payload.

### 2.5.1 Governing Equations and Controller Design for Schilling Titan II System

The Schilling Titan II is a six d.o.f. industrial hydraulic manipulator, shown in Figure 2.15. The Titan II is a widely used hydraulic manipulator in undersea and nuclear applications. It is attractive because of its high strength, low weight, and large workspace. However, the manipulator suffers from poor dynamic characteristics, largely due to high joint friction. Performance during small, slow motions is dominated by nonlinear friction effects. Further, it is very difficult to model the actuator and joint characteristics (Merritt, 1967; Habibi *et al.*, 1994; Electricité de France, 1996).

In this study the control system was implemented on a Sun 3/80 interfaced to a VME bus. The control software is run on a 68030 single-board computer (Durfee *et al.*, 1991; Kuklinski, 1993). Position feedback from the Titan II's joints is measured with resolvers, and dedicated hardware converts the resolver signal to quadrature waves with an effective resolution of 0.087 degrees. For all experiments, the sampling rate was seven milliseconds, which was deemed sufficiently fast for fine motion experiments.

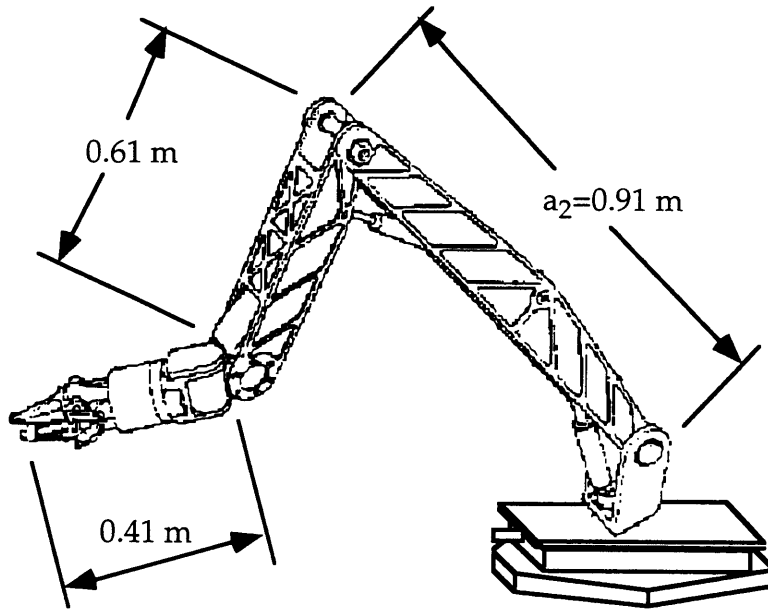


Figure 2.15: Schilling Titan II Dimensions

The position control scheme consists of an inner torque loop and an outer position loop, as shown in Figure 2.16. An inner loop integral compensator provides low-pass filtering, and zero steady-state error. Previous theoretical and experimental work has shown that an integral compensator with a feedforward term provides the best torque control performance for a geared, DC motor-driven manipulator (Vischer and Khatib, 1995; Morel and Dubowsky, 1996). Similar linear analysis is less conclusive for the Titan II, due to its highly nonlinear dynamic characteristics in the operating range of interest. Experimentation has shown, however, that the selection of an inner loop integral compensator is effective for this system.

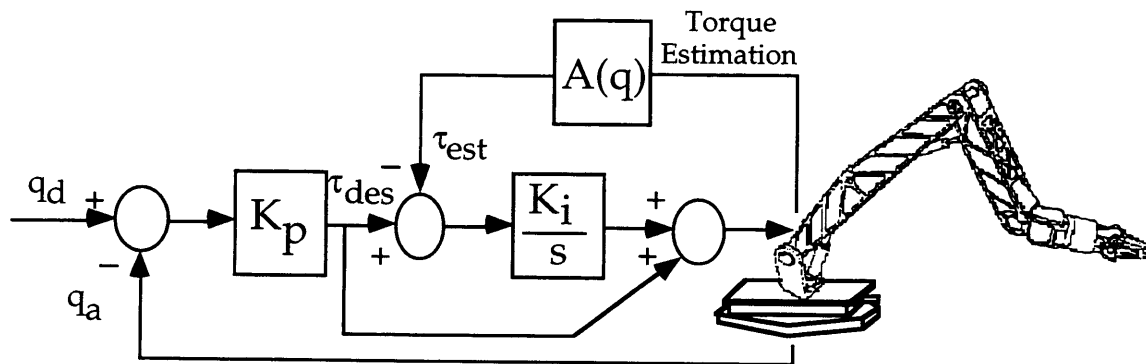


Figure 2.16: Control System Architecture



A simple proportional controller is employed in the outer loop. A derivative term was not added (as in (Morel and Dubowsky, 1996)) due to the high level of damping caused by joint friction. The control law was:

$$\tau_{\text{out}} = \tau_{\text{des}} + K_{\text{int}} \int_0^r (\tau_{\text{des}} - \tau_{\text{est}}) \quad (2.20)$$

with

$$\tau_{\text{des}} = K_p (\theta_d - \theta) \quad (2.21)$$

Equation 2.10, when applied to the Titan II, yields the following form for the matrix A for the first three joints (see Figure 2.17 for Titan II frame assignments):

$$A(q) = \begin{pmatrix} 0 & 0 & 0 & 0 & 0 & -1 \\ 0 & 0 & 0 & -\sin(\theta_1) & \cos(\theta_1) & 0 \\ a_2 \cos(\theta_1) \sin(\theta_2) & -a_2 \sin(\theta_1) \sin(\theta_2) & -a_2 \cos(\theta_2) & -\sin(\theta_1) & \cos(\theta_1) & 0 \end{pmatrix} \quad (2.22)$$

For clarity, we can write explicitly:

$$\tau_1 = -M_{\text{base}}^z \quad (2.23)$$

$$\tau_2 = -\sin(\theta_1) M_{\text{base}}^x + \cos(\theta_2) M_{\text{base}}^y \quad (2.24)$$

$$\tau_3 = \tau_2 - a_2 (-\cos(\theta_1) \sin(\theta_2) F_{\text{base}}^x + \sin(\theta_1) \sin(\theta_2) F_{\text{base}}^y + \cos(\theta_2) F_{\text{base}}^z) \quad (2.25)$$

As expected, the torque estimation equations depend only on the manipulator joint positions, the measured base wrench, and the manipulator's kinematic parameters. These estimation equations are computationally very simple, and for the case of the Titan II requires knowledge of only a single kinematic parameter,  $a_2$ .

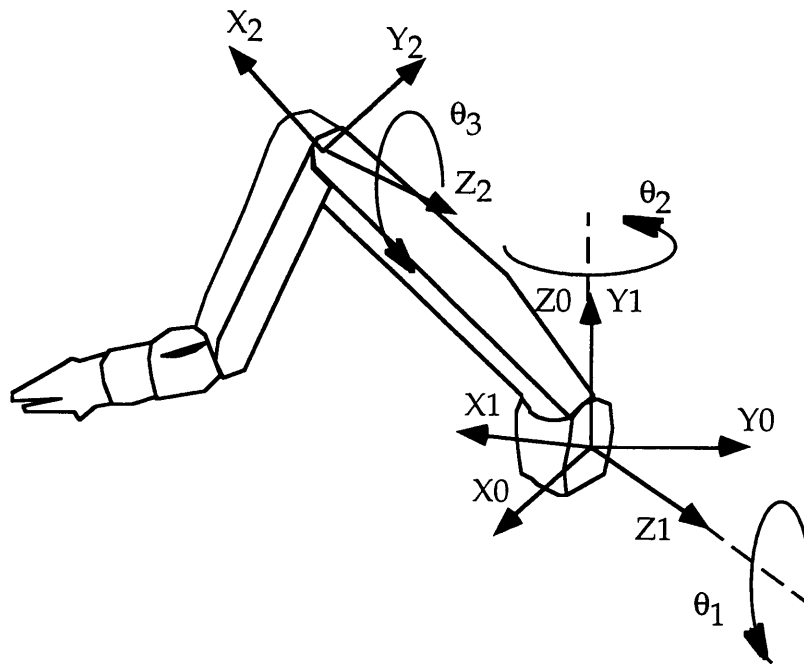


Figure 2.17: Schilling Titan II Coordinate Frames

## 2.5.2 Experimental Results for Schilling Titan II System

### 1) Joint Space Position Control Results

The first task presented is for the third joint ( $\theta_3$ ) of the Titan II to track a 1.5 degree magnitude triangular wave at 0.1 Hertz. Due to the Titan II's very high levels of joint friction, this small amplitude, slow motion is difficult to execute. The commanded trajectory magnitude corresponds to approximately 17 counts of the quadrature-converted resolver signal.

The benchmark against which control performance is compared is PI control. Proportional and integral gains were tuned to be at 75% of the level causing structural oscillation. Figure 2.18 compares the performance of traditional proportional-integral (PI) control (dashed line) and proportional control with base-sensor feedback (solid line). For motions of this magnitude, PI control requires a relatively long time ( $\approx 6$  seconds) to reach zero-error tracking. Base-sensor feedback allows the manipulator to achieve good tracking performance within a much shorter ( $\approx 0.5$  second) time. Due to the integral nature of both controllers, tracking performance lags at velocity sign changes (when the frictional force changes direction).

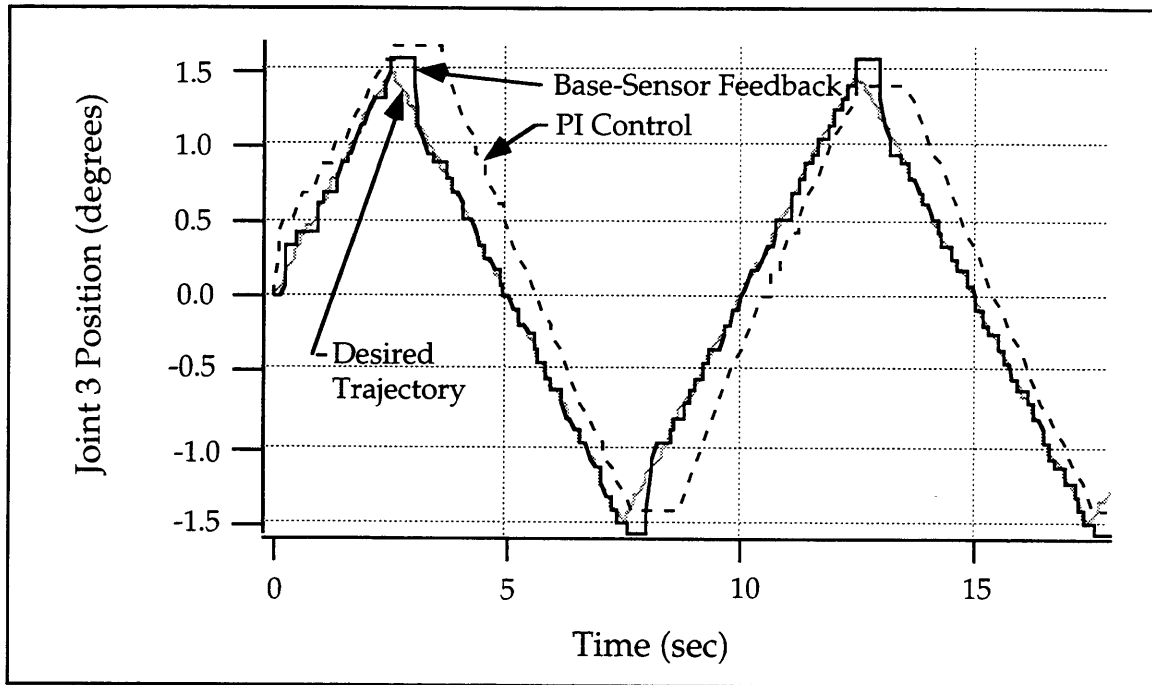


Figure 2.18: Joint Three Triangular Wave Tracking

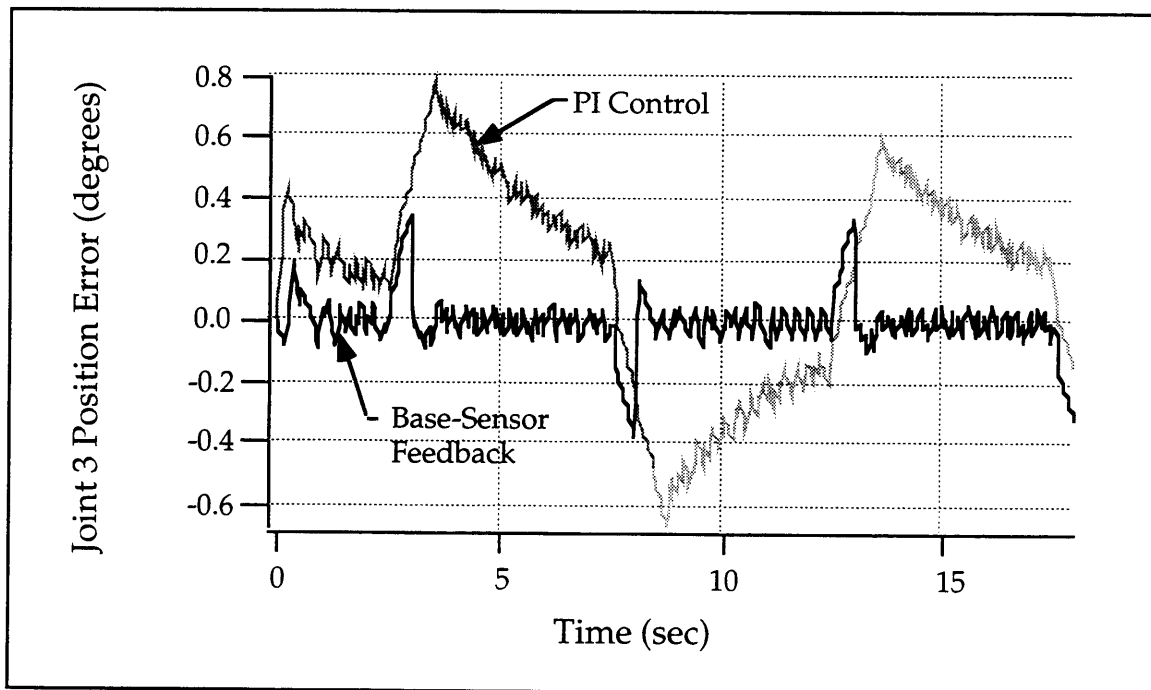


Figure 2.19: Joint Three Triangular Wave Tracking Error

Figure 2.19 shows the joint angular errors of the two control approaches, and Table 2.3 qualitatively compares the results. Proportional

control with torque estimation achieves a 77% improvement in RMS error over PI control, and the maximum error is substantially reduced.

	RMS Error (degrees)	Maximum Error (degrees)
PI	0.3671	0.7860
P + Base Sensor Feedback	0.0861	0.3460

Table 2.3: Summary of Error Results for 1.5° Triangular Wave Tracking

Figure 2.20 compares performance of the same controllers with the same gains executing 0.5 degree, 0.1 Hertz triangular waves, which correspond to a magnitude of approximately 6 counts, and velocity of 2 counts per second.

At these very low speeds, proportional control with base-sensor feedback requires slightly longer to compensate for friction at velocity sign changes ( $\approx 1$  sec). However, zero steady-state error is still achieved.

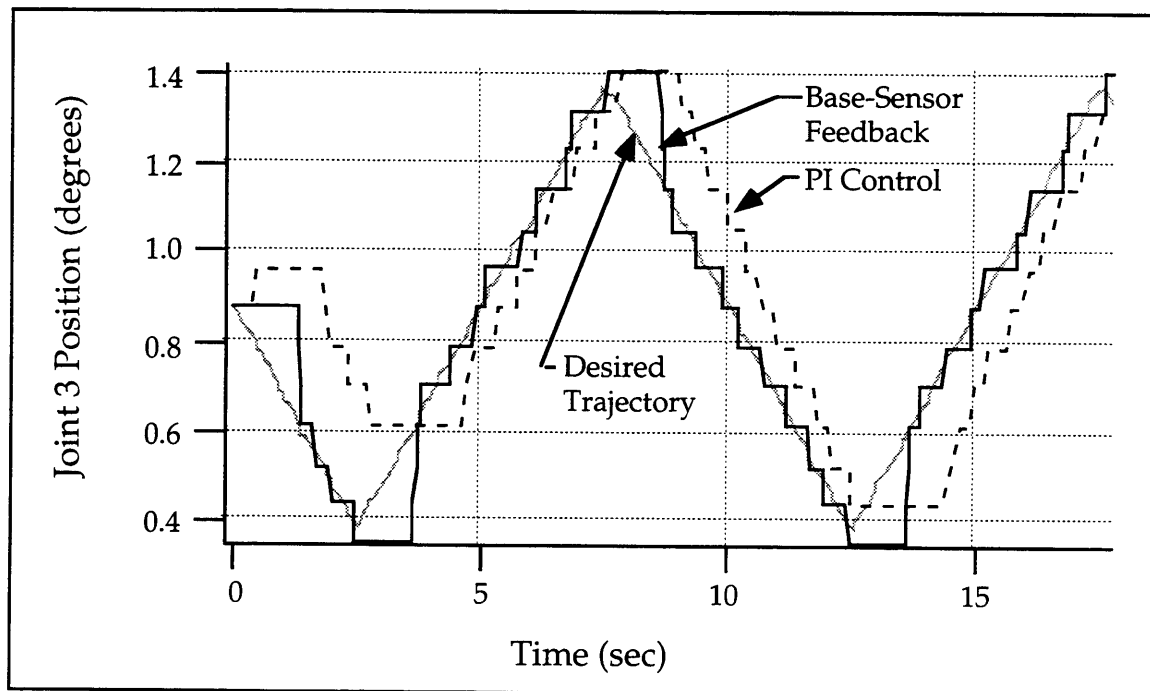


Figure 2.20: Joint Three Triangular Wave Tracking

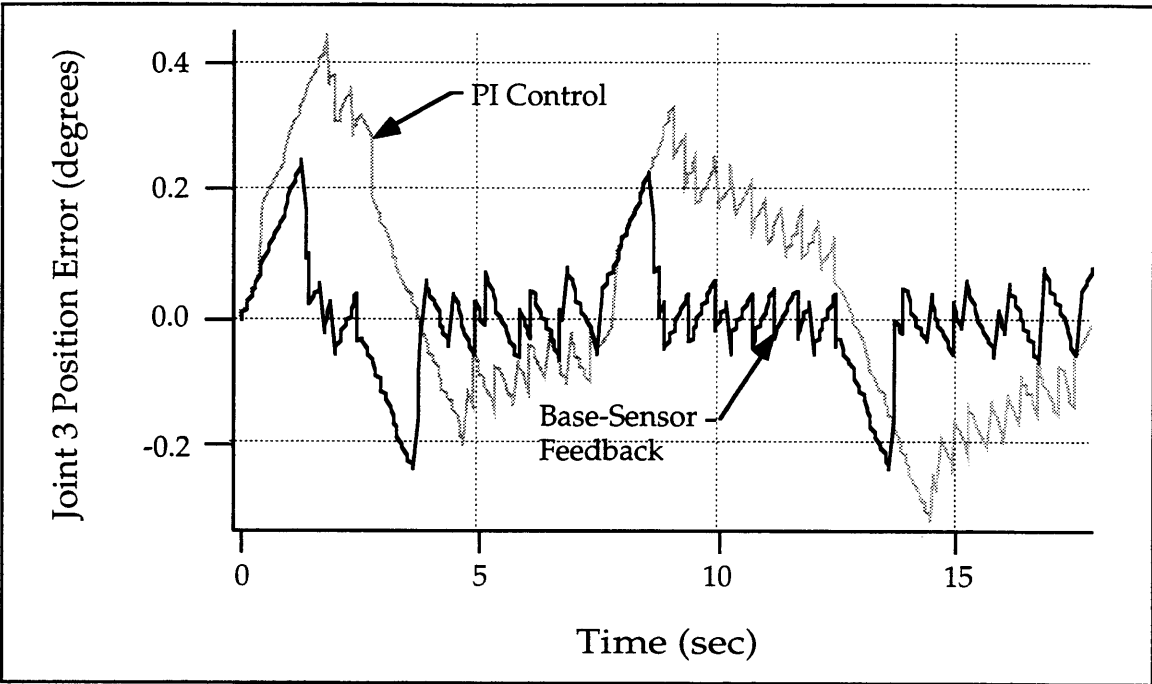


Figure 2.21: Joint Three Triangular Wave Tracking Error

Table 2.4 compares the error of the two types of control for this trajectory. Base sensor feedback achieves a 54% improvement in RMS error over PI control. While some errors remain, recall that this is a very large, powerful manipulator with very high joint friction performing a very slow and small motion, a very difficult task for it.

	RMS Error (degrees)	Maximum Error (degrees)
PI	0.1863	0.4480
P + Base Sensor Feedback	0.0845	0.2520

Table 2.4: Summary of Error Results For 0.5° Triangular Wave Tracking

*II) Cartesian Space Position Control Results*

Cartesian-space tasks are more typical of practical applications. Here, a cartesian task was designed using joints two and three of the Titan II manipulator. The desired endpoint trajectory was a small circle of 15 m m

radius at a speed of .166 revolutions per minute. Recall that the manipulator has a reach of approximately 1.9 meters. Joint-space paths were computed off-line using inverse kinematics. Errors were formed in joint space, and thus the control scheme is unchanged.

What is unique to this experiment is that coupled motion between joints with two parallel axes is required. The axes of rotation of joints two and three are parallel. The simplification of the torque estimation equation (i.e. the removal of dynamic terms for the torque estimation of joint 3) is thus explicitly tested.

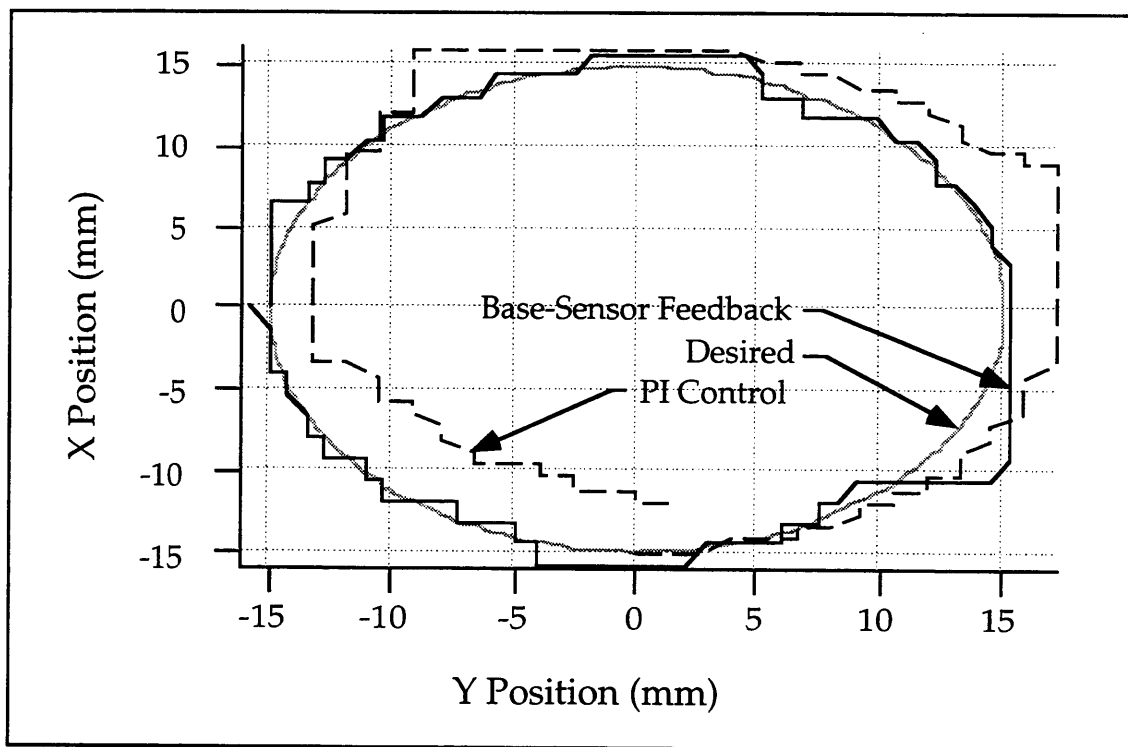


Figure 2.22: Cartesian Space Tracking

The effectiveness of the model-free base-sensor controller is shown in Figure 2.22. Table 2.5 gives a numerical summary of the results. Clearly, the method makes a significant improvement.

	RMS Error (degrees)	Maximum Error (degrees)
PI	3.033	4.643
P + Base Sensor Feedback	0.776	1.365

Table 2.5: Summary of error results cartesian-space tracking

### III) Joint Space with Payload Results

Many industrial tasks require accurate positioning of heavy payloads, such as the placement of the steam generator nozzle dam during nuclear power facility maintenance (Electricité de France, 1996). A control system must therefore be robust to variations in the effective inertia of the system, and should provide high-performance control in both loaded and unloaded states. The Titan II is a very lightweight arm (77 kg). However, an ungeared, lightweight arm which is capable of supporting large loads will be subject to dramatic variations in the effective manipulator inertia tensor, a difficult control problem. While adaptive control methods can be applied, they have limitations (Craig, 1988). Here it is shown that the model-free control scheme is robust enough to deal with these variations, and still provide accurate tracking performance.

The commanded task was for the third joint of the Titan II to perform one degree sine wave tracking at 0.1 hertz while supporting a payload. The payload has a weight of 210 Newtons, a load that is approximately 30% of the Titan II weight. However, since the maximum torque capacity of joint 3 is 1200 Nm, a fully extended payload represents only 17% of the Titan II's maximum lift capacity.

Figure 2.23 compares the tracking performance of PI control and P control with base sensor feedback. From these results we see that even with a small payload, the performance of PI control is substantially degraded. With base sensor feedback, rapid response to friction sign changes and to initial control switching (at time=0) is exhibited, and zero-error tracking is achieved.

The rapid tracking of the system with base sensor feedback implies that the system bandwidth has been increased. This result follows the conclusions drawn for electrical systems (Pfeffer *et al.*, 1989; Vischer and Khatib, 1995).

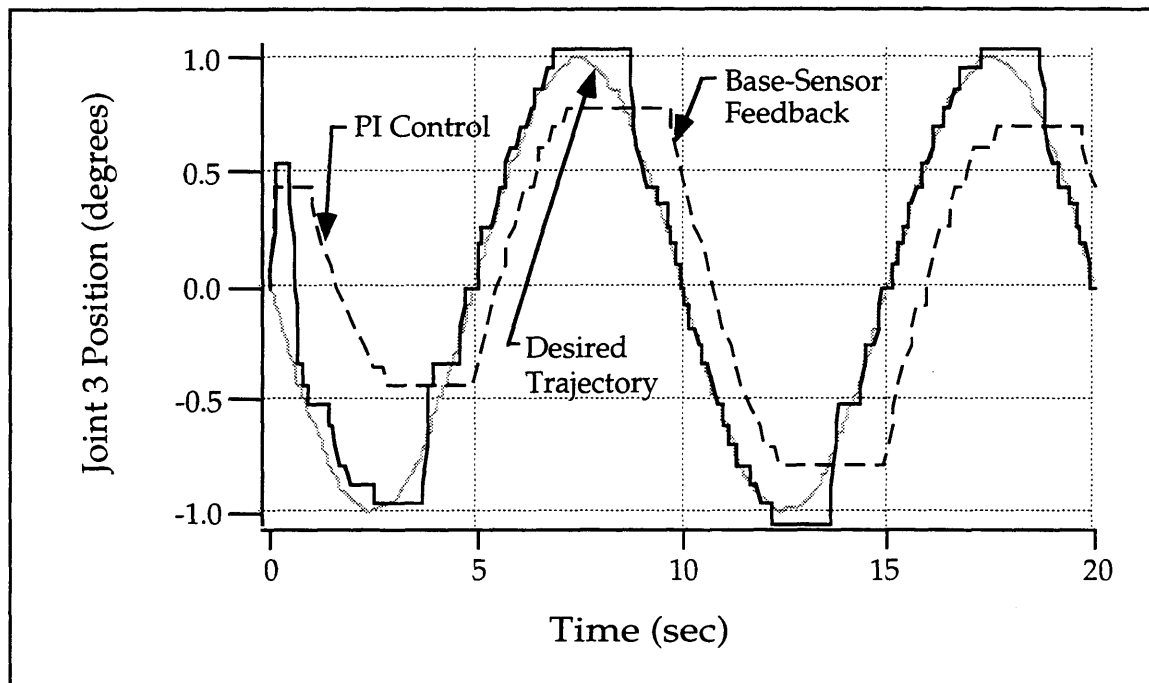


Figure 2.23: Joint Three Tracking with Payload

## 2.5 Summary and Conclusions

This chapter presented simulation and experimental studies of fine-motion position control of both a PUMA 550 and a Schilling Titan II manipulator. The theoretical framework for the base force/torque sensor method was discussed, and a simplified form of the algorithm was formulated for the fine-motion case. Simulation results for a PUMA 550 manipulator executing fine-motion tasks were presented and shown to be consistent with experimental results, confirming the validity of the simulation. Extensive experimental results for the Schilling Titan II system were presented, for unloaded free motion tasks, and free motion tasks with a payload. The results showed substantial improvement over conventional control schemes.



## Chapter 3

# Manipulator Force Control

### 3.1 Introduction

This chapter describes simulation and experimental studies of delicate force control of a PUMA 550 manipulator. Section 3.2 presents a description of the force control simulation engine. Section 3.3 describes the force control experimental setup. Section 3.4 presents the theoretical background, simulation and experimental results for joint torque control. Section 3.5 presents a theoretical background, simulation and experimental results for implicit force control.

### 3.2 Force Control Simulation

A force control simulation program was developed, based on the position control simulation described in Section 2.3. The position control simulation was modified to include the effect of end-effector contact forces, both on the motion of the manipulator and on the base sensor measurement.

The environment was modeled as a lightly damped one-dimensional linear spring, as follows:

$$F_{env} = (K_{env} \cdot \delta) + (b_{env} \cdot \dot{\delta}) \quad (3.1)$$

where  $\delta$  is defined as the penetration into the simulated environment boundary. For the following simulations, an environment with a simulated stiffness of  $K_{env}=50$  kN/m and damping rate of 100 Ns/m was used. These

parameters are similar to experimentally-measured parameters of a stiff environment (An, 1988).

The effect of environment interaction on manipulator motion was simulated by computing the joint torque caused by contact, and subtracting this torque from the applied joint torque. The joint torque caused by environment interaction is computed from the environment interaction force,  $F_{env}$ , via the relation:

$$\tau_{env} = J^T \cdot F_{env} \quad (3.2)$$

where  $J$  is defined as the manipulator Jacobian matrix and is of dimension  $(3 \times n)$ , where  $n$  is the number of manipulator joints. The vector  $F_{env}$  is assumed to be  $\in \mathcal{R}^3$ , since environment contact is modeled as frictionless point contact.

The effect of environment contact on the base sensor measurement is computed via simple rigid-body analysis, as shown in Figure 3.1. The wrench measured by the base sensor due to a generalized interaction force can be expressed at the base via a force/moment transformation, as follows:

$$W_{env} = F_{env} + (r_{oa} \times F_{env}) \quad (3.3)$$

where all vectors are expressed in the base-sensor frame.

This interaction wrench is then added to the total computed base wrench (i.e. the wrench caused by dynamic robot motion).

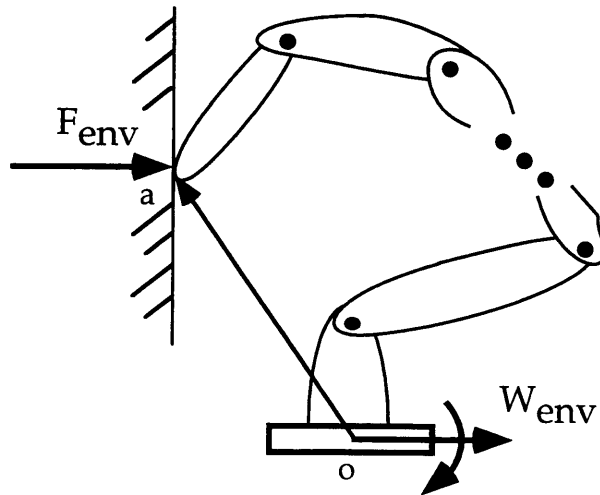


Figure 3.1: Simulated Base-Sensor Interaction Force Measurement

### 3.3 Force Control Experimentation

The system used for the following experiments was a PUMA 550 five d.o.f. manipulator, shown in Figure 2.5. The PUMA control architecture is based on a Programmable Multi-Axis Controller (PMAC) and a Sun 3/80 running VxWorks (Durfee *et al.*, 1991; Kuklinski, 1993). Control loops were run on a single-board 68020 computer, with sampling periods of eight milliseconds.

For the experiments in this chapter, joint one of the PUMA was controlled, and joints two and three were held under joint PID control. The initial state of the PUMA was  $\theta_1=0^\circ$ ,  $\theta_2=0^\circ$ ,  $\theta_3=90^\circ$ . This can be seen in Figure 3.2.

A rigid aluminum brace was used as the environment. The stiffness of the environment was determined empirically to be approximately 50 kN/m. Damping was not experimentally determined, but was assumed to be low.

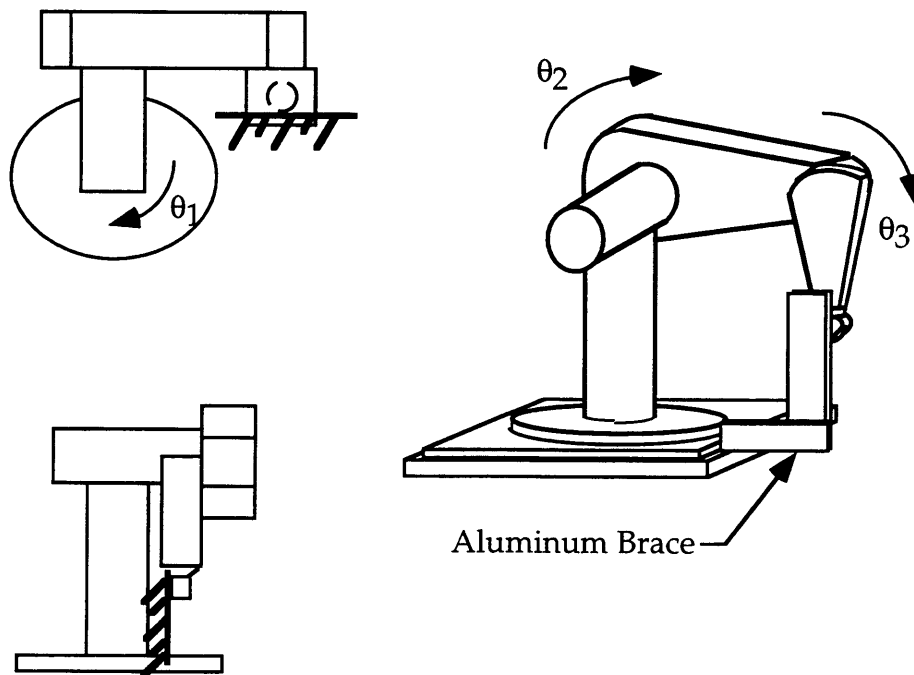


Figure 3.2: Force Control Experimental Setup

### 3.4 Torque Control

Torque control is a force control method which relies on accurate control of individual joint torques. A desired environment interaction force is achieved by transforming the interaction force to a vector of desired joint torques, through the relation  $\tau_{des} = J^T \cdot F_{des}$ . Closed-loop control is then performed on these desired torques.

An analysis of torque control's disturbance rejection properties is presented in this section, and simulation results for a torque-controlled system are also discussed. Experimental studies on a PUMA 550 manipulator are shown to agree well with simulation results.

#### 3.4.1 Torque Control Theory

Torque control is an effective method of rejecting joint-level disturbances, such as friction (An, 1988; Williams and Khatib, 1995, Morel and Dubowsky, 1996). Linear analysis presented in Chapter 2.2.1 demonstrated the effectiveness of torque control on system positioning accuracy. Here, we examine torque control at the joint level, in order to understand its influence on force control.

Figure 3.3 is a simplified block diagram of a single manipulator joint with a frictional disturbance.

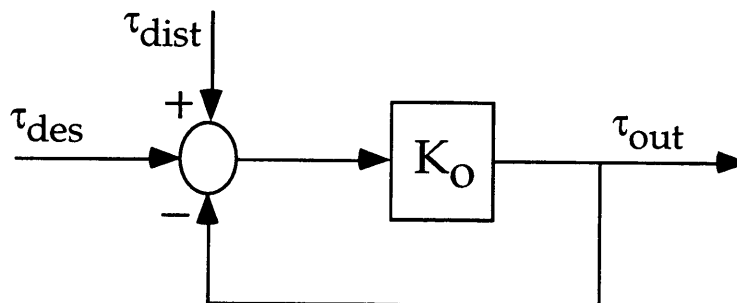


Figure 3.3: Single Joint Model with Frictional Disturbance

In this simple model, the output torque,  $\tau_{out}$ , is related to the desired torque,  $\tau_{des}$ , by the relation:

$$\tau_{out} = (\tau_{des} - \tau_{dist}) \left( \frac{K_o}{K_o + 1} \right) \quad (3.4)$$

There is no means of disturbance rejection for this model. This is highly ineffective for situations where  $\tau_{dist}$  is large relative to  $\tau_{des}$ , such as small, low-velocity motion, such as force control. In this case, the output torque differs substantially from the desired torque, and force control performance is poor. For this reason, torque control is not used as a force control method for geared systems without torque feedback.

An integral compensator is expected to reject joint-level disturbances. Figure 3.4 shows the previous system with the addition of an integral compensator and a feedforward term. Note that this model assumes “perfect” torque feedback (i.e. there is no error in the measurement of  $\tau_{out}$ ).

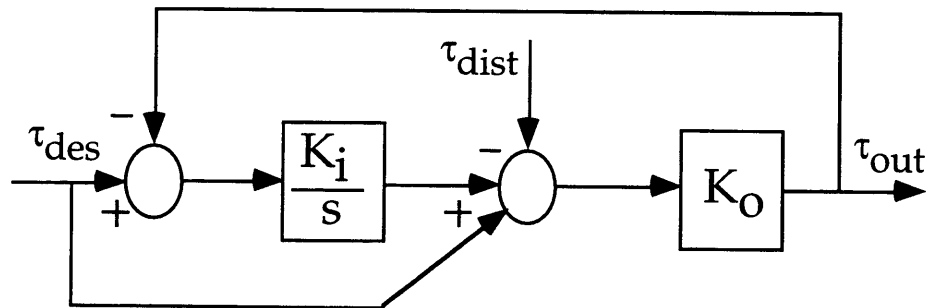


Figure 3.4: Single Joint with Frictional Disturbance Under Integral Control

In this model, the output torque,  $\tau_{out}$ , is related to the desired torque,  $\tau_{des}$ , by the following relation (assuming  $K_o$  is near unity):

$$\tau_{out} = \tau_{des} + \left( \frac{s}{s + K_i} \right) \tau_{dist} \quad (3.5)$$

The addition of an integral compensator rejects disturbances below a break frequency which is set by the integral gain  $K_i$ . This is illustrated in Figure 3.5.

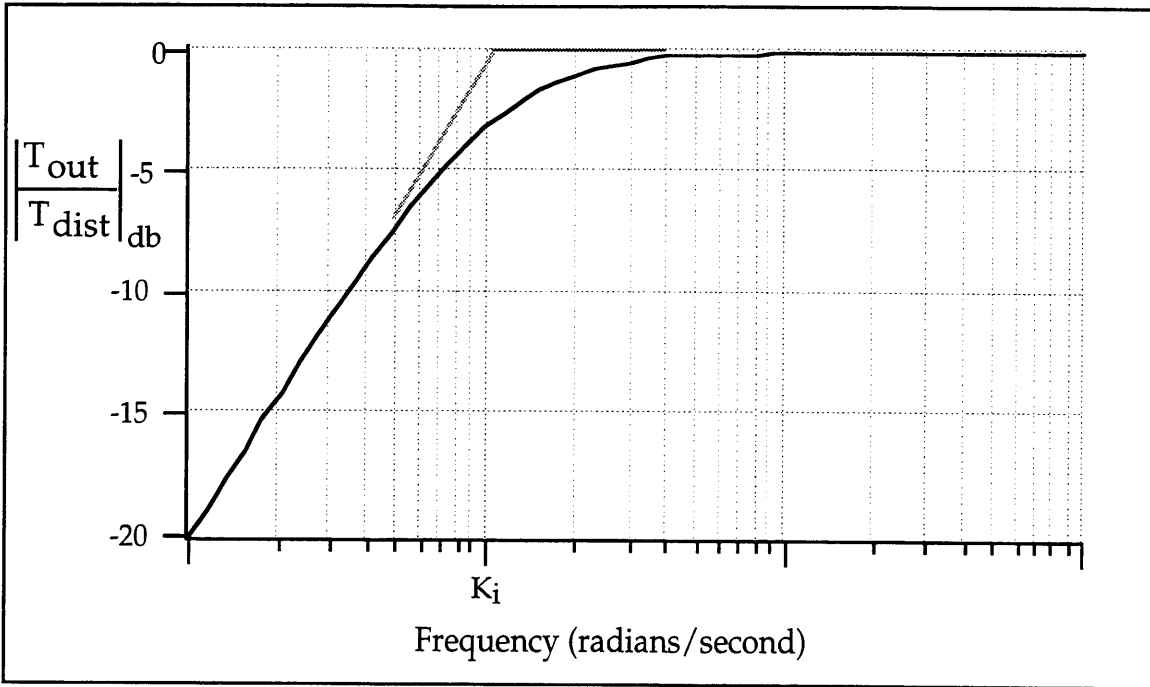


Figure 3.5: Integral Compensator Disturbance Rejection Properties

From this simple example, it is clear that the addition of an integral torque feedback loop improves the manipulator's disturbance rejection properties, and therefore its torque tracking abilities. This benefit is directly applicable to force control. Given a desired environment interaction force, a vector of desired joint torques can be computed via the relation:

$$\tau_{des} = J^T \cdot F_{des} \quad (3.6)$$

To exert a desired interaction force, accurate control of individual joint torques is required. For manipulators with low drivetrain friction (such as direct-drive manipulators), accurate torque control is possible (Asada and Youcef-Toumi, 1987). For manipulators with joint friction, however, we have shown that the output torque can differ substantially from the desired torque. This results in poor force control performance, and thus torque control is an ineffective force control method for geared manipulators without some form of torque feedback.

A block diagram of the experimental system used in this work is shown in Figure 3.6. A desired force is specified, from which a desired torque vector is computed. Closed-loop control is performed on this desired torque,

using the simplified torque estimation equations for the PUMA manipulator (Equations 2.17 through 2.19). The assumptions of small, slow motions, which were made for the fine-motion positioning case are equally valid for the force control case.

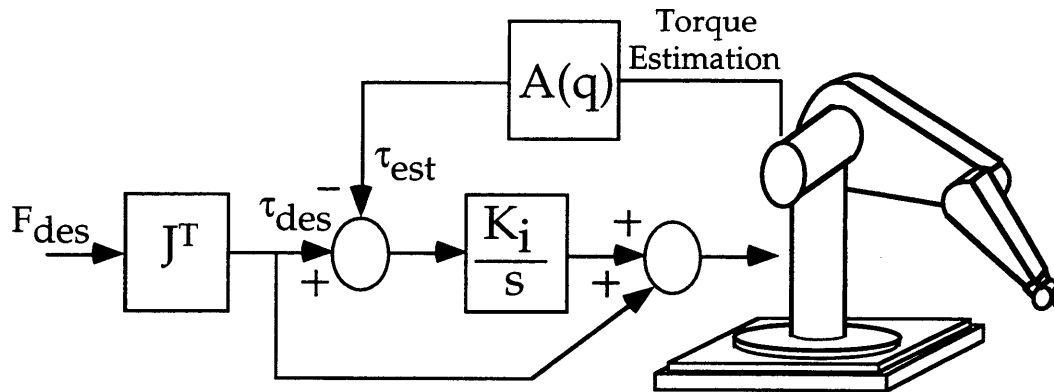


Figure 3.6: Torque Control System Architecture

For force control, it is interesting to note that the base-sensor feedback becomes inherently equivalent to wrist sensor feedback if the manipulator is considered a rigid body. Thus, the proposed control scheme can be viewed as similar to recent wrist sensor-based schemes (Williams and Khatib, 1995). It is important to realize, however, that a wrist sensor measures only forces caused by interaction, while the base sensor measures forces caused by both motion and interaction. Thus, the base-sensor could be used as the basis for a high-performance hybrid control scheme (controlling both interaction-related and motion-related torque), but a wrist sensor could not.

### 3.4.2 Torque Control Simulation Results

A simulation task was written for the first joint of the PUMA 550. A desired force of 10 Newtons was commanded, with the manipulator beginning in contact with the environment. Integral control with feedforward was employed as a compensator, as shown in Figure 3.6. The interaction force is plotted in Figure 3.7.

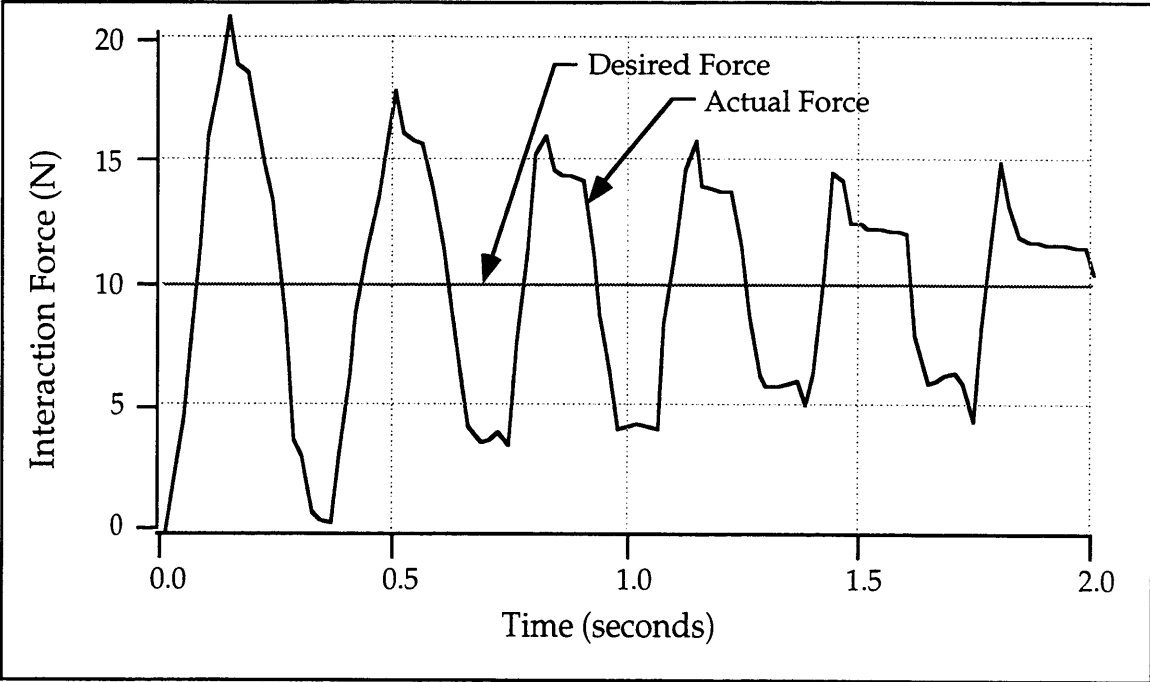


Figure 3.7: Torque Control Simulation—Pure Integral Control

Although the simulated system is stable, the response exhibits undesirable oscillations. These oscillations are caused by the absence of damping in the system. This is due to the fact that the torque control loop effectively removes joint friction, which accounts for much of the system's mechanical damping. Additionally, there is no electronic (i.e. velocity-based) damping present in the controller.

To reduce the oscillations of Figure 3.7, a damping term is added to the controller which takes the form  $K_d \dot{\theta}$ . Thus, the control law is as follows:

$$\tau_{\text{out}} = \tau_{\text{des}} + K_{\text{int}} \int_0^t (\tau_{\text{des}} - \tau_{\text{est}}) + K_d \dot{\theta} \quad (3.7)$$

The response of the damped system to a desired command input of 10 Newtons is shown in Figure 3.8.



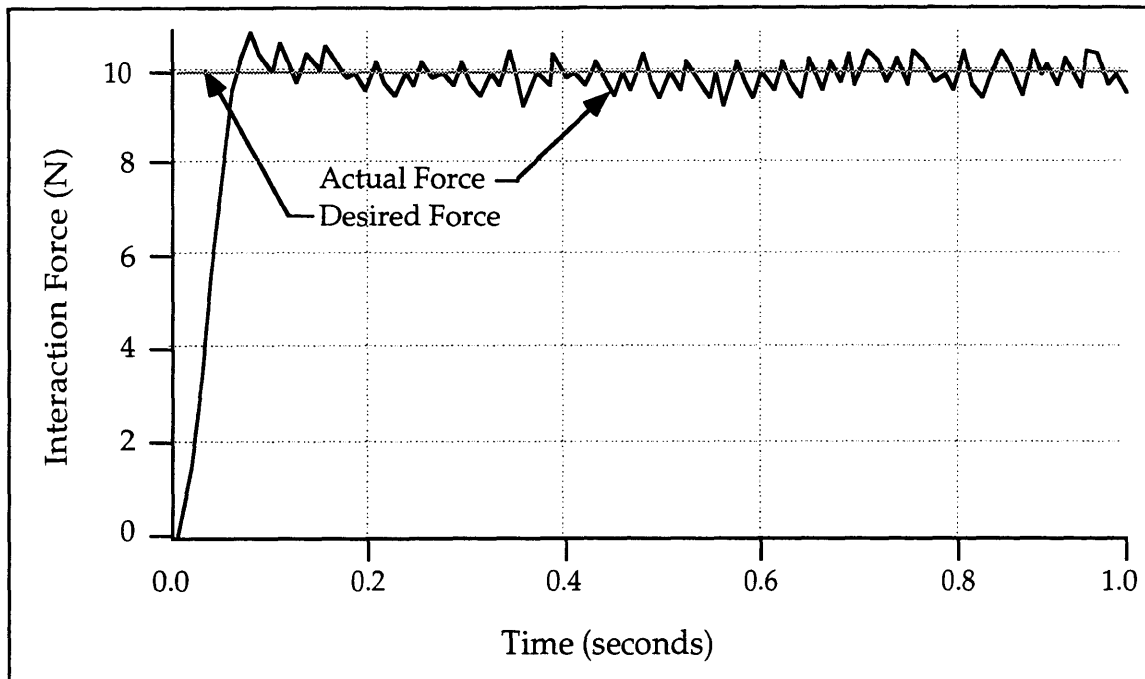


Figure 3.8: Torque Control Simulation—Integral Control with Damping

From Figures 3.7 and 3.8, it is clear that the introduction of damping to the control law improves system response with respect to overshoot and settling time. This result is well documented in the literature (Volpe and Khosla, 1992). Note, however, that high-frequency components result from the addition of damping. This is due to the high  $K_d$  term that is required to attain a substantial level of damping. The high-frequency components are a product of the  $K_d$  gain acting on the joint velocity, which is small but highly variable during force control.

Another method suggested by researchers to improve system response involves filtering the command signal through a dominant pole, in an attempt to remove high-frequency components of the signal that cause oscillation (An, 1988; Roberge *et al.*, 1996). A dominant pole takes the form  $(a/(s+a))$ . This is a simple first-order filter with unity gain at DC, and a break frequency set by the constant  $a$ . The control law for the system with a dominant pole is as follows:

$$\tau_{\text{out}} = \left( \frac{a}{s+a} \right) \tau_{\text{des}} + K_{\text{int}} \int_0^t (\tau_{\text{des}} - \tau_{\text{est}}) \quad (3.8)$$

Figure 3.9 displays the simulated response of the torque controlled system with a dominant pole, attempting to attain a desired force of 10 Newtons. The response is well damped and the rise time corresponds to the time constant of the dominant pole, as expected. Small high-frequency oscillations still exist in the system response, but this behavior is caused by vibration of the stiff environment/manipulator system, rather than the addition of velocity-dependent damping. This distinction is significant in the control of real systems, as we will see in Section 3.4.3.

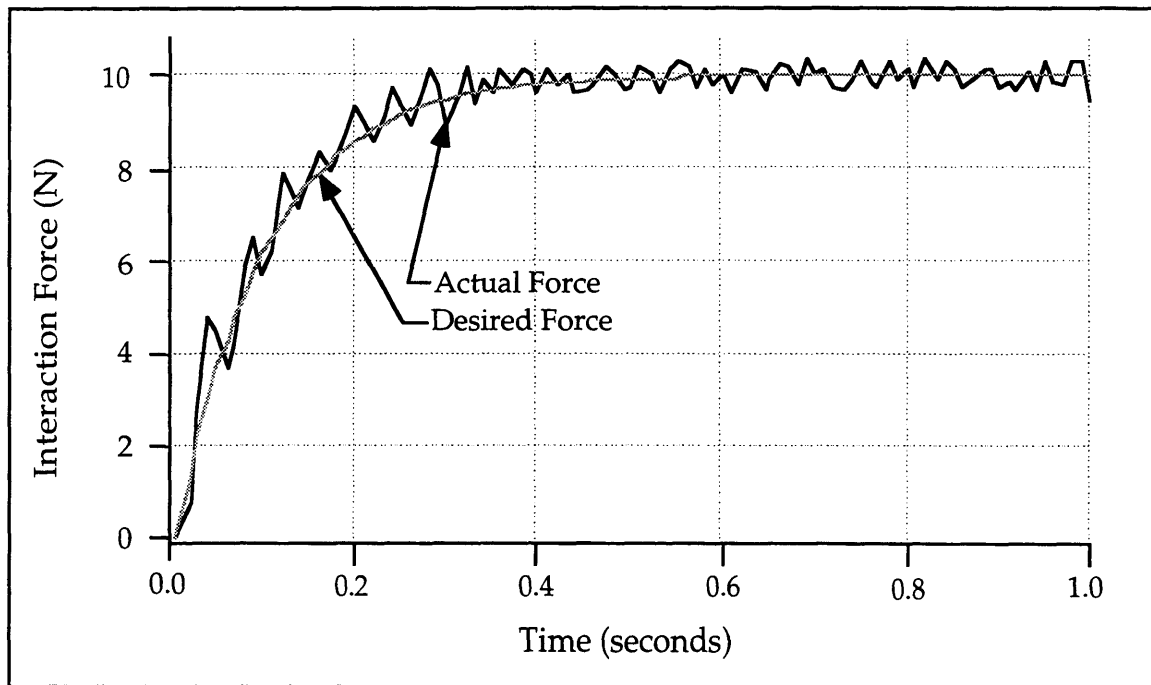


Figure 3.9: Torque Control Simulation—Integral Control with Dominant Pole

### 3.4.3 Torque Control Experimental Results

An experimental task was designed for the first joint of the PUMA 550. A desired force of 5.2 Newtons was commanded, with the manipulator beginning in contact with the environment. Integral control with feedforward was employed as a compensator, as shown in Figure 3.6. The interaction force is plotted in Figure 3.10.

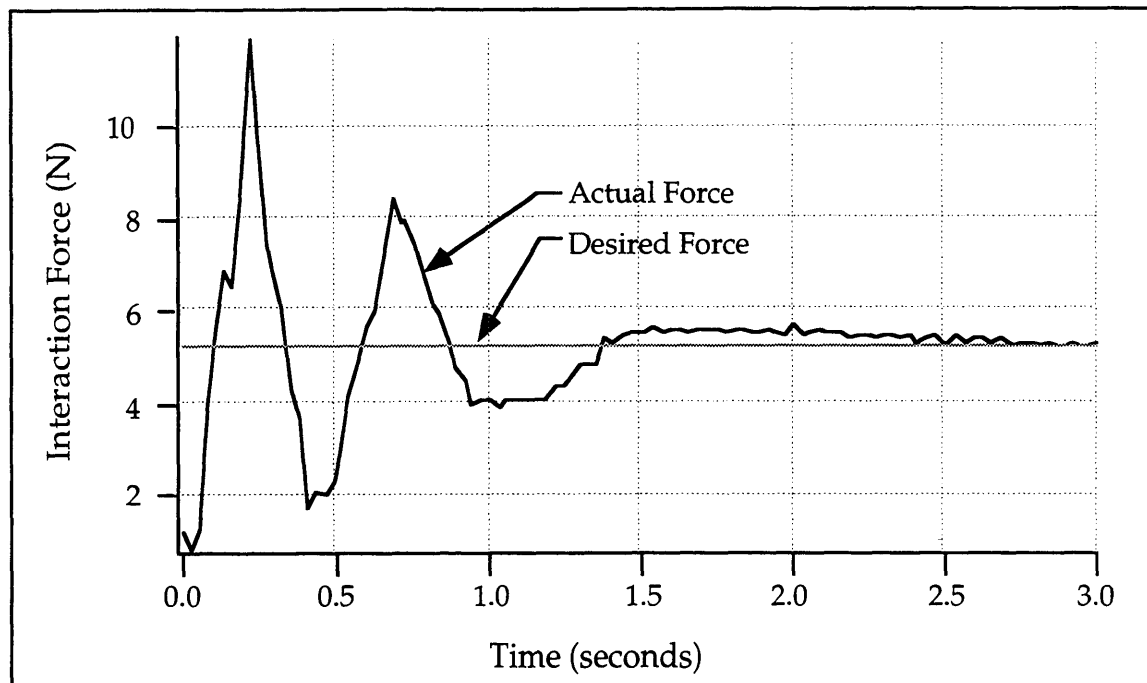


Figure 3.10: Torque Control Experimentation—Pure Integral Control

Although the experimental system is stable, the response exhibits undesirable oscillations and a large overshoot (maximum percent overshoot  $\approx 288\%$ ). As in simulation, these oscillations are caused by the absence of damping in the system, and in fact confirm the high performance of the torque control loop. Joint friction has been largely removed from the system. (Note that the initial interaction force offset was caused by sensor drift.)

As in the simulation, damping of the form  $K_d \dot{\theta}$  was added to the system control law in an attempt to reduce oscillation. The modified control law was identical to Equation 3.7, and experiments were performed for desired force step inputs of approximately 5 Newtons. Unlike the simulated system, however, the addition of damping tended to have a destabilizing effect on the system. Most step response trials resulted in unstable or marginally stable performance. This is most likely due to fact that first-order backward-difference numerical differentiation of the position was used to calculate the velocity. For small, slow motions (which predominate in force control), the computed velocity is highly variable. This variability leads to

“spikes” in the control signal from the term  $K_d\dot{\theta}$ , which in turn leads to oscillation or instability.

Figure 3.11 displays a result which was typical of experiments involving velocity-based damping terms. In this experiment a dominant pole was added in order to improve system stability.

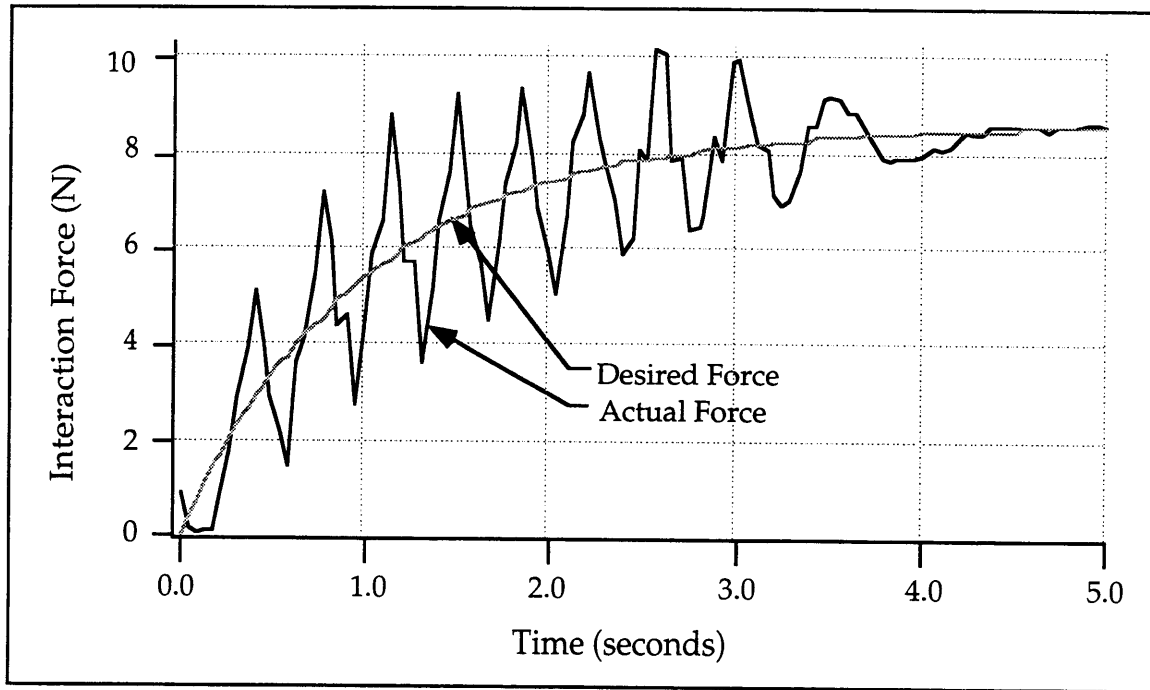


Figure 3.11: Torque Control Experimentation—Integral Control with Damping

Experiments were also conducted which utilized a dominant pole filter. The desired interaction force was 4.5 Newtons, and the control law was identical to Equation 3.8. The pole of the filter was placed at 1.43 radians per second, giving a time constant of 0.7 seconds. The results of this experiment can be viewed in Figure 3.12.

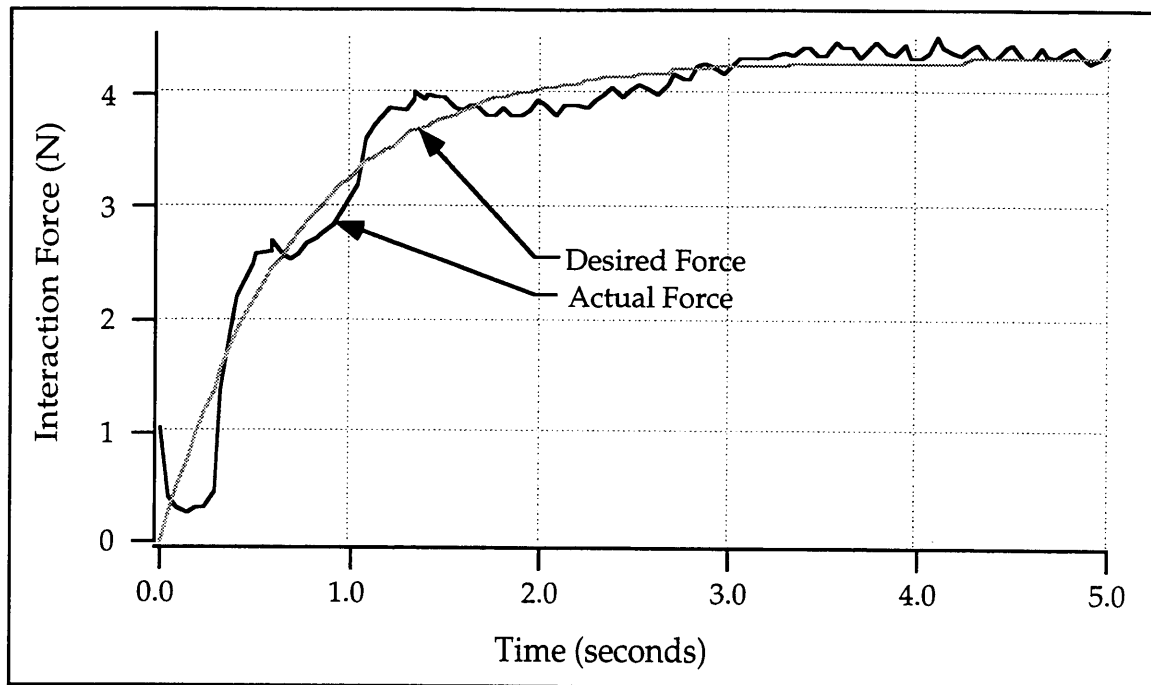


Figure 3.12: Torque Control Simulation—Integral Control with Dominant Pole

This system exhibits stability and good tracking. The time response of the system is slower than the simulated system, but is still acceptable for many real-world applications. A small amount of steady-state error remains, but this is to be expected from a torque-controlled system (An, 1988). Kinematic uncertainty and sensor noise limit the absolute accuracy of the response.

### 3.5 Implicit Force Control

Implicit force control refers to a force control scheme where closed-loop control is not performed on the measured environment interaction force, but rather on endpoint position. The desired position is related to a desired force by an estimate of the environment stiffness. This scheme is sometimes referred to as *position-based force control* (Whitney, 1987).

An analysis of implicit force control's accuracy limitations is presented in this section. Simulation results are then presented, which focus on

attainable force resolution. Experimental results are presented which agree with simulation studies, and show that torque feedback improves the allowable force resolution.

### 3.5.1 Implicit Force Control Theory

The relationship between desired force and desired position can be understood by examining the model of Figure 3.13.

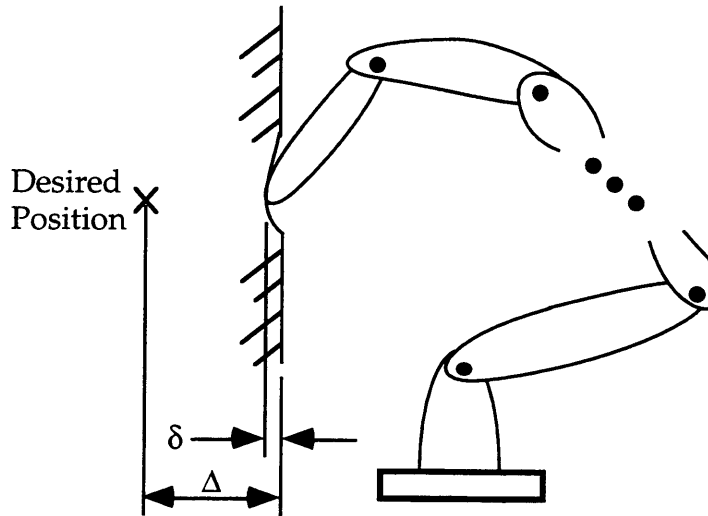


Figure 3.13: Force Control Environment Interaction Model

A desired position which lies at a distance  $\Delta$  beyond the environment boundary is commanded. When the robot contacts the environment, a small deflection  $\delta$  results. The resultant stiffness of the manipulator/environment system can be modeled as a series spring combination. That is,

$$\frac{1}{K_{\text{tot}}} = \frac{1}{K_{\text{arm}}} + \frac{1}{K_{\text{env}}} \quad (3.9)$$

Assuming linear elastic behavior, we can relate the desired force to the desired position by the following equation:

$$x_{\text{des}} = F_{\text{des}} / K_{\text{tot}} \quad (3.10)$$

Noting that the arm stiffness is configuration dependent, we can write Equation 3.10 in a slightly expanded form, which gives an equation for calculating desired position from a desired force:

$$x_{des} = \left( \frac{F_{des}}{\left( \frac{K_{env} \cdot J^T K J}{K_{env} + J^T K J} \right)} \right) \quad (3.11)$$

In this equation,  $J$  represents the manipulator Jacobian matrix, and  $K$  represents the diagonal joint stiffness matrix. The product  $J^T K J$  is the cartesian-space stiffness matrix (Craig, 1986).

From the preceding analysis, we see that accurate implicit force control relies on manipulator kinematics, and knowledge of the environment stiffness. If both of these factors were known exactly, Equation 3.11 could be used in an algorithm to compute a position trajectory, based on a desired force input. However, environment stiffness is often difficult to estimate accurately, and thus implicit force control is inherently inaccurate (Mills, 1996; Siciliano *et al.*, 1996).

Although highly accurate force control is difficult to achieve, high *resolution* force control is attainable. For this reason, implicit force control is often used in tasks which require the application of forces which need not be precisely known (Dubowsky, 1996; Mills, 1996). For many tasks, such as precision assembly and part mating, force resolution is a critical system performance metric.

Rearranging Equation 3.10, we see that:

$$F_{des} = K_{tot} \cdot x_{des} \quad (3.12)$$

Force control resolution depends on the attainable positioning resolution. Based on the high resolution obtained in small-magnitude positioning tasks in Chapter 2, we expect to be able to attain high resolution during force control. Controlling small-magnitude forces will be the focus of the simulation and experimental tasks that follow.

A block diagram of the implicit force control system can be seen in Figure 3.14. From this figure, we observe that implicit force control differs from torque control only by the generation of its input signals. We also observe that the implicit force control scheme is identical to the position control scheme employed in Chapter 2. The advantage of using a position-based control scheme is that it allows for a single control system to be used for both positioning and contact tasks, potentially eliminating the need for controller switching in a task that requires both positioning and environment interaction. This is advantageous since controller switching can lead to instability and undesirable transients (Slotine, 1991).

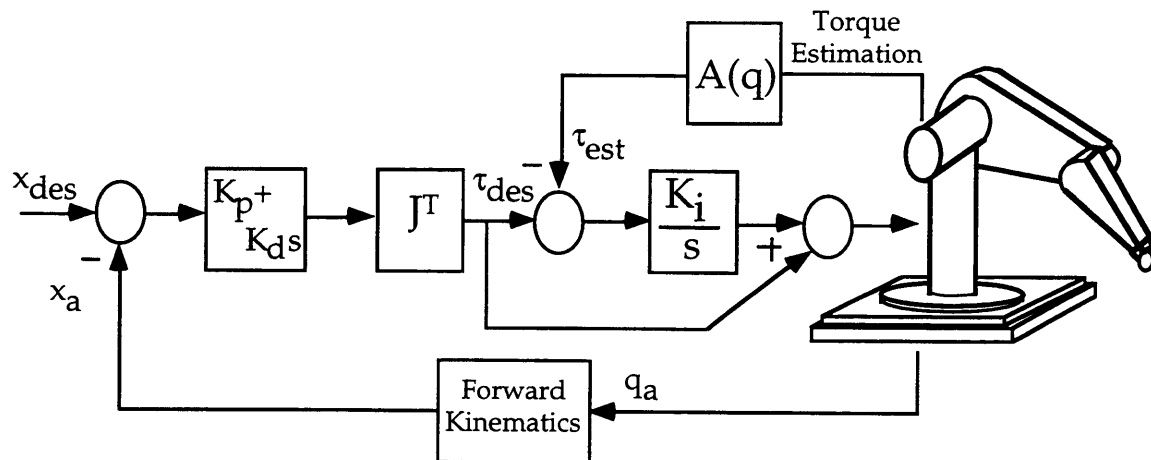


Figure 3.14: Implicit Force Control System Architecture

### 3.5.2 Implicit Force Control Simulation Results

Simulation tasks were written for the first joint of the PUMA 550. Although the stiffness of the simulated environment was known exactly, a desired interaction force was not explicitly commanded, since the purpose of this experiment was to examine the force resolution of the system, not the absolute accuracy.

The performance of a simulated system without torque feedback was first examined. In this case, the system control law is reduced to classical cartesian-space PD form:



$$\tau_{\text{out}} = K_p(x_{\text{des}} - x_a) + K_d(\dot{x}_{\text{des}} - \dot{x}_a) \quad (3.13)$$

Without torque feedback, nonlinear friction can dominate the performance at low speeds, and we would expect to observe relatively poor force resolution (Armstrong, 1991). The control law of Equation 3.13 was implemented in simulation, and a desired position which lay beyond the simulated environment was commanded. A 2.0 mm magnitude sinusoid was the desired trajectory. However, the manipulator could not track signals of such small magnitude. Static friction was greater than the commanded output torque, and thus no motion was observed. Successive trials were performed, until recognizable force tracking was achieved. The interaction force for a typical experiment is plotted in Figure 3.17.

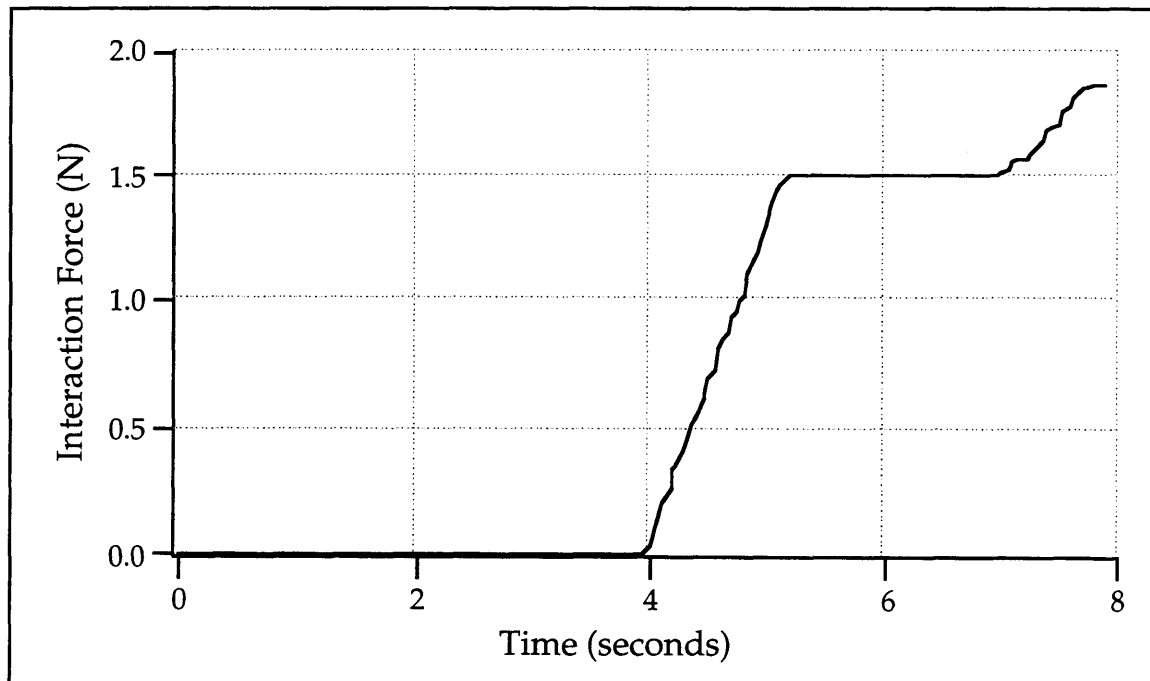


Figure 3.15: Implicit Force Control Simulation Results—PD Control

As expected, the system under PD control demonstrates marked stick-slip behavior, which leads to poor force resolution. It is clear that joint friction impairs force control performance, as well as position control performance. For PD control without torque feedback, the maximum attainable force resolution was found to be approximately 2 N. These

simulation results strongly suggest that high resolution force control is not achievable under standard PD control.

The performance of a simulated system with torque feedback was then examined. The control architecture for this system can be seen in Figure 3.14. The simplified torque estimation equations (Equations 2.17 through 2.19) were used. A desired position which lay beyond the simulated environment was commanded. A sinusoidal desired position of magnitude 2.0 mm was added to a DC offset of 1.0 mm, and this offset sinusoid was filtered through a first-order filter with break frequency of 1 Hz in order to ensure that the manipulator did not lose contact with the environment. The commanded position profile can be seen in Figure 3.16. The interaction force is plotted in Figure 3.17.

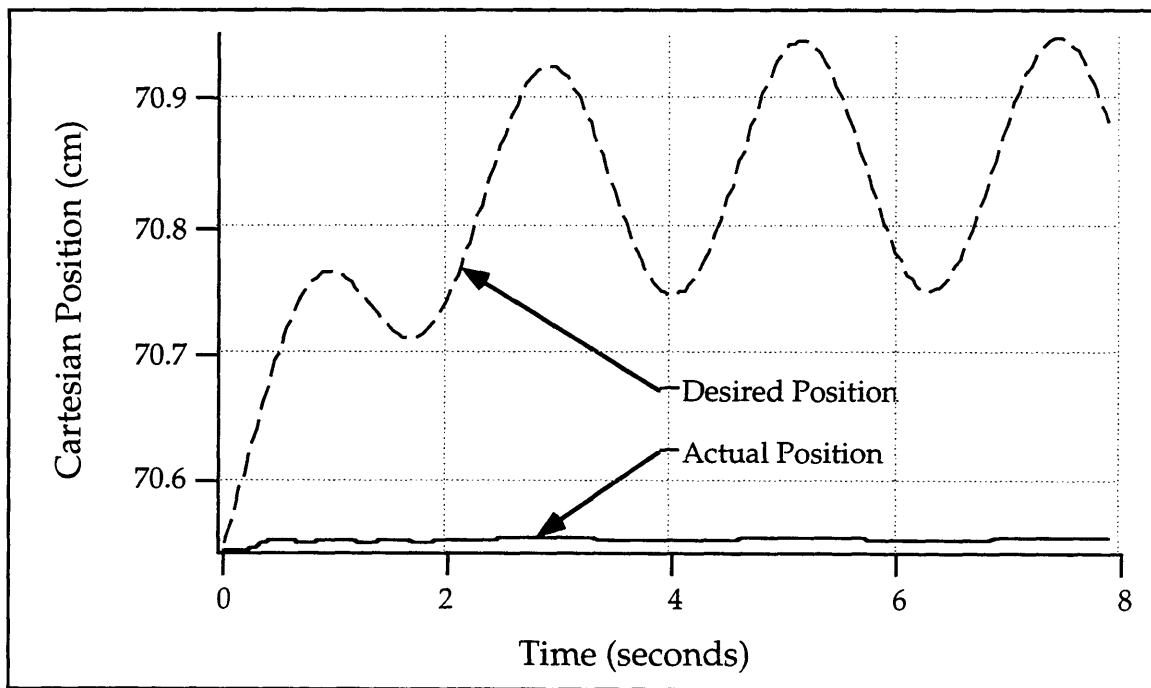


Figure 3.16: Implicit Force Control Position Trajectory—PD Control with Torque Feedback

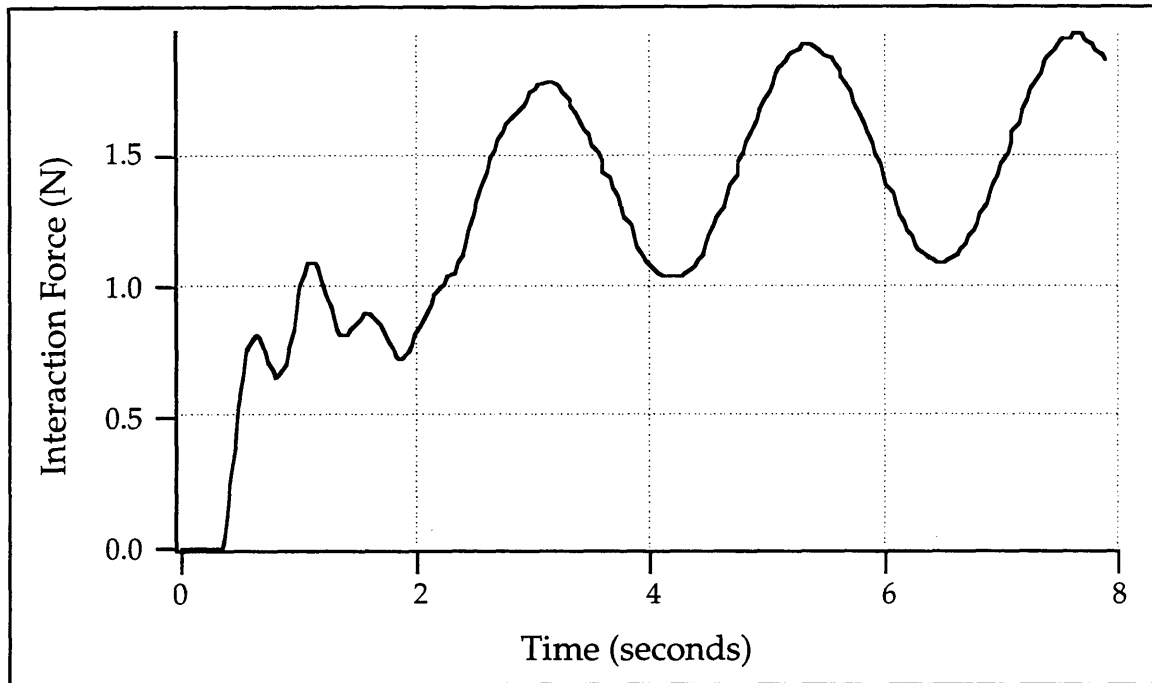


Figure 3.17: Implicit Force Control Simulation Results—PD Control with Torque Feedback

The system is stable, and able to respond to minute changes in the command signal, even while in contact with a stiff surface. This suggests that implicit force control is a viable method for high-resolution force control. Numerous simulation trials were performed, and the maximum attainable force resolution was found to be approximately 0.1 N. In theory, with perfect torque feedback, the limitation on attainable force resolution is set by the resolution of the cartesian endpoint position. This limitation is configuration-dependent and is dictated by the encoder resolution, as:

$$\delta x_{\max} = J \cdot \delta \hat{\theta} \quad (3.14)$$

where  $\delta \hat{\theta}$  is a vector composed of the angular displacement corresponding to one encoder count.

### 3.5.3 Implicit Force Control Experimental Results

Experimental tasks were performed with the PUMA 550. The location of the environment was measured, and a desired position which lay “inside” the environment surface was commanded (see Figure 3.13).

Experimental trials were first conducted for joint one of the PUMA under PD control, without torque feedback. The desired position trajectory and interaction force for a typical trial are shown in Figures 3.18 and 3.19.

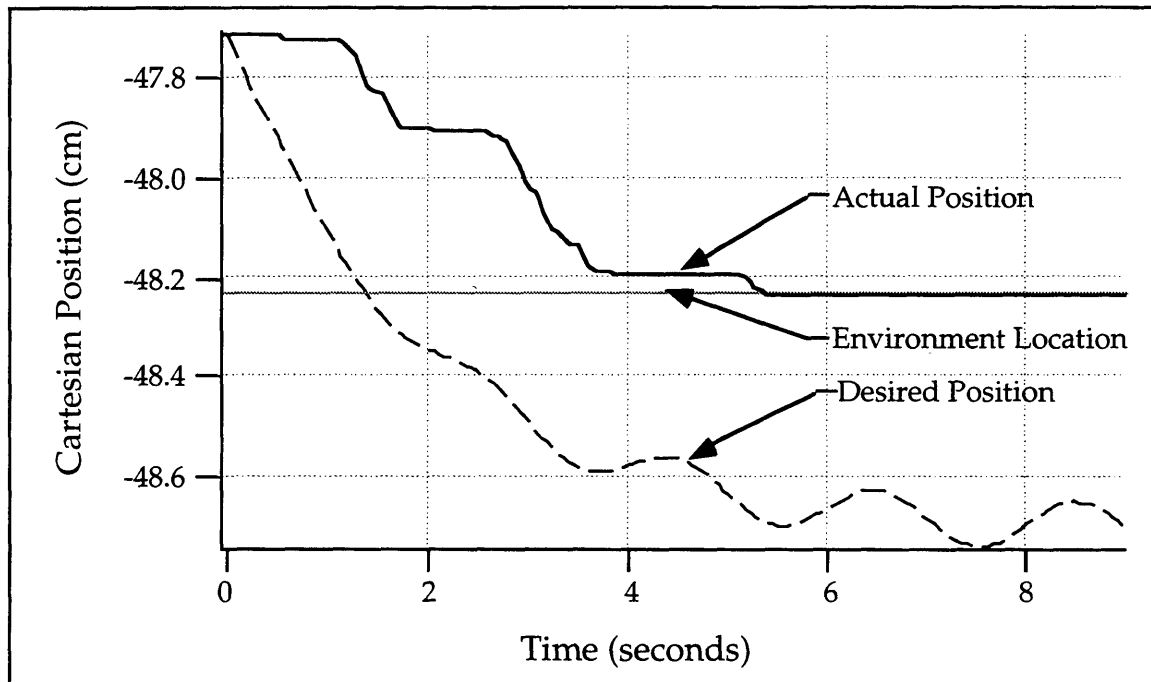


Figure 3.18: Implicit Force Control Desired Position Trajectory—PD Control

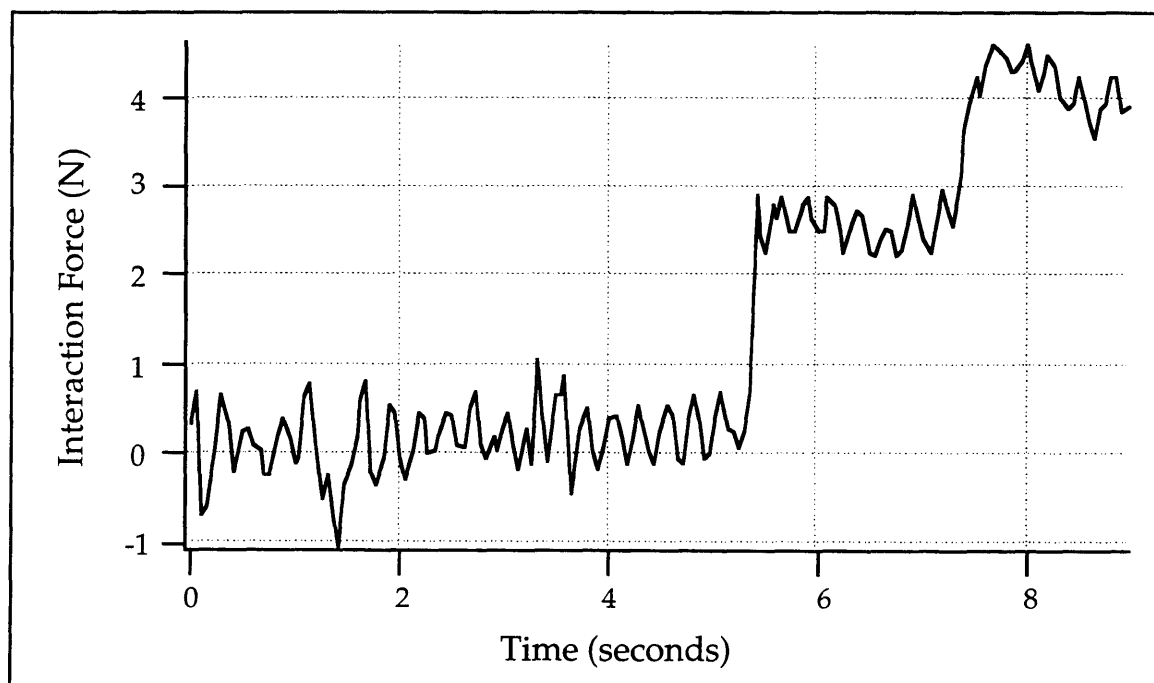


Figure 3.19: Implicit Force Control Experimental Results—PD Control

As in the simulation, the system under PD control demonstrated stick-slip behavior, which leads to poor position tracking, and poor force resolution. For PD control without torque feedback, the maximum attainable force resolution was found to be approximately 1.5 N. These results confirm that high resolution force control is not achievable under standard PD control.

Experimental trials were then conducted for joint one of the PUMA with torque feedback. A sinusoidal desired position of amplitude 1.0 mm was added to a DC offset of 1.0 cm, and this offset sinusoid was digitally filtered through a first-order filter with a time constant of 2 seconds, in order to ensure that the manipulator did not lose contact with the environment. The commanded position profile can be seen in Figure 3.20.

The control system was identical to the system shown in Figure 3.14. The simplified torque estimation equations (Equations 2.17 through 2.19) were used in the torque feedback loop. The interaction force is plotted in Figure 3.21.

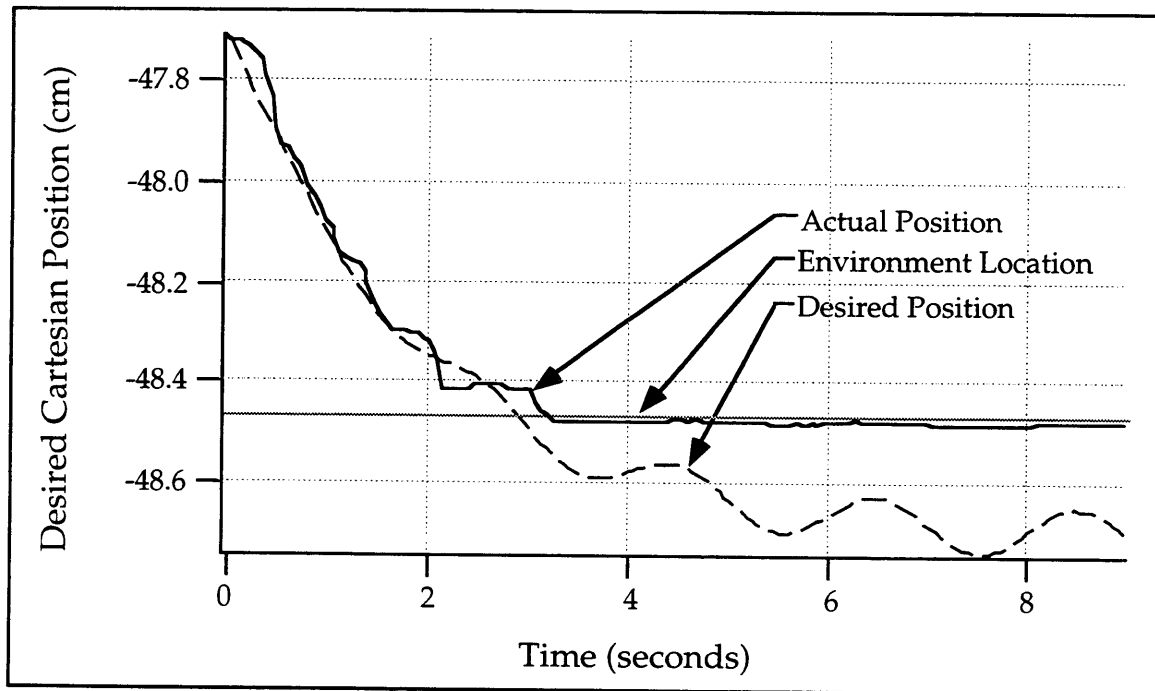


Figure 3.20: Implicit Force Control Position Trajectory—PD Control with Torque Feedback

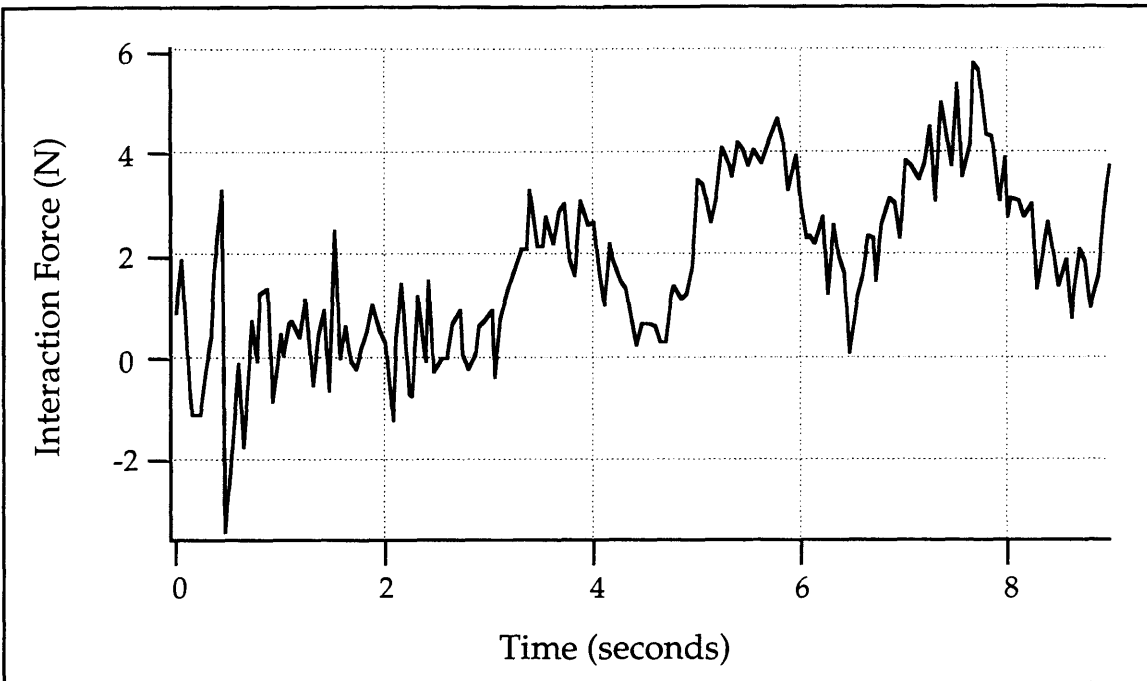


Figure 3.21: Implicit Force Control Experimental Results—PD Control with Torque Feedback

From Figure 3.21 we observe that the experimental system can respond to minute changes in the commanded position signal, as predicted by the simulation. It is also important to note that the system is stable during contact. Stability during contact is an important property of implicit force control.

Additional experimental trials were performed in an attempt to discern the maximum allowable force resolution. Figure 3.22 displays the highest-resolution trial recorded. From this figure we can see that sensor noise becomes significant with respect to the signal level as the desired force resolution increases. However, this noise is due to electronics, and is not caused by high-frequency interaction forces. This is confirmed by the fact that the noise frequency is identical before and after contact. Thus, the noise can be filtered with a second-order Butterworth filter. The unfiltered and filtered force signals are displayed in Figure 3.21. Note that the negative interaction forces are caused by sensor offset.

Based on all trials, it was concluded that the maximum achievable force resolution is approximately equal to 0.5 Newtons. This number is

approximate due to the uncertainty caused by noise filtering and configuration dependency. Different manipulator configurations could have drastically different force control properties, especially under the cartesian control scheme of Figure 3.14. The estimation of 0.5 Newton resolution was found to be a reasonable average value over a large portion of the PUMA workspace.

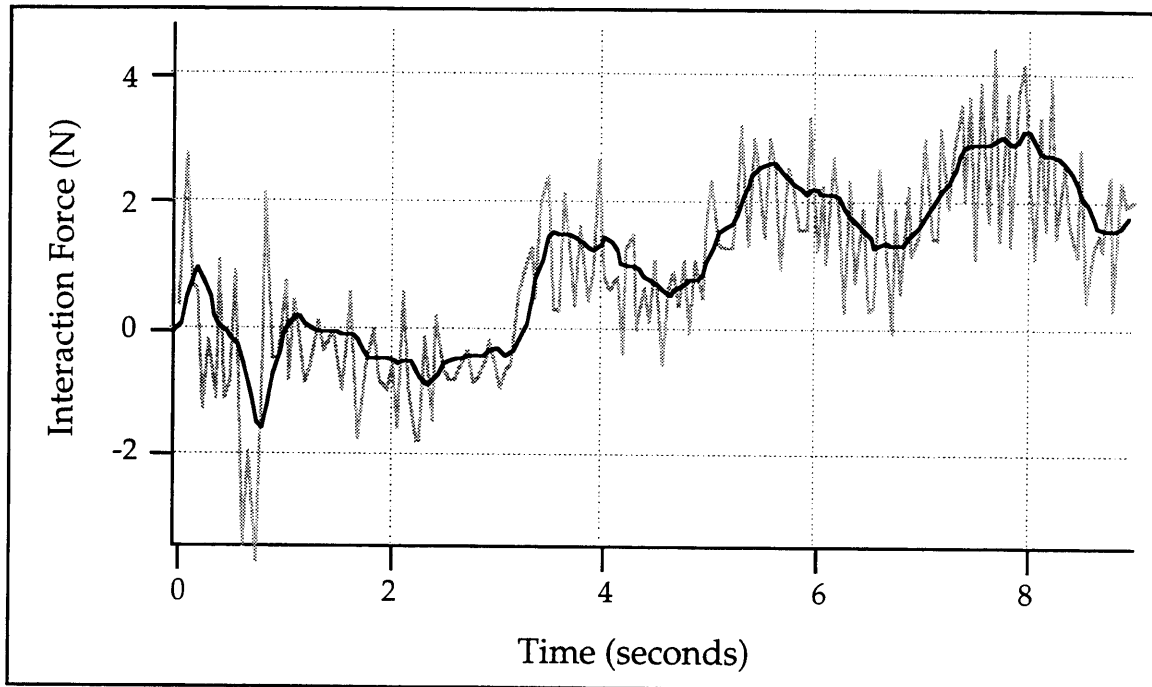


Figure 3.21: Implicit Force Control Experimental Results—PD Control with Torque Feedback

### 3.6 Summary and Conclusions

This chapter presented simulation and experimental studies of two different types of force control: torque control, and implicit force control. The theoretical framework for both control methods was discussed, and predictions were made regarding system performance. Simulation results for both types of force control were presented. Experimental results were then presented which largely agreed with the simulation results.

Torque control with a dominant-pole filter was shown to be an accurate, stable force control method. Implicit force control was shown to

allow high force control resolution, although its accuracy is limited. Force resolution, however, can reach the sub-Newton level with base-sensor feedback. Implicit force control was also found to be stable during contact, even against a stiff environment. It was shown that “real-world” effects, such as numerical differentiation and sensor noise, hindered the experimental systems.



## Chapter 4

# Manipulator Identification

### 4.1 Introduction

This chapter describes theoretical and experimental studies of manipulator mass and inertial parameter identification. Section 4.2 presents a slightly modified version of a mass parameter identification method which was developed for use with the base force/torque sensor (West *et al.*, 1989). Theoretical analysis and experimental results are presented. Section 4.3 presents a description of an inertial parameter estimation method which was developed for use with the force/torque sensor (Liu *et al.*, 1997). The algorithm described in section 4.3 was developed by Guangjun Liu, and is presented here for completeness. Theoretical analysis and experimental results of mass and inertial parameter identification are presented.

### 4.2 Manipulator Mass Parameter Identification

Mass parameter identification refers to the determination of masses and center of mass locations of the links of a manipulator. These parameters are important for gravity compensation and model-based control schemes, but are not usually known by robot manufacturers. Thus, methods to identify these parameters have been developed (West *et al.*, 1989).

Mass parameter identification is conceptually simple. Consider the single d.o.f. manipulator shown in Figure 4.1. The goal of mass parameter

identification is to identify the link mass,  $m$ , and the distance of the center of mass from the joint,  $c$ .

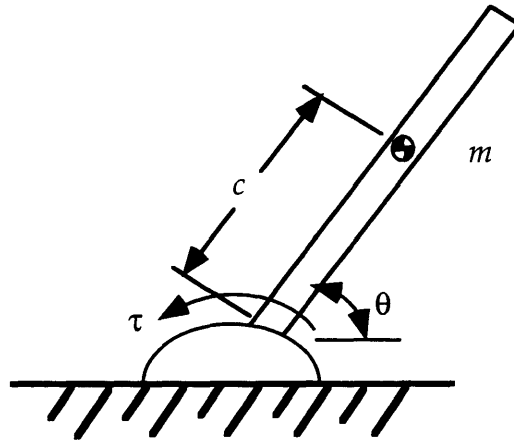


Figure 4.1: A One Degree-Of-Freedom Static Manipulator

The relationship between torque and link mass is:

$$\tau = m \cdot g \cdot c \cdot \cos(\theta) \quad (4.1)$$

It is clear that the product of the link mass and distance of the center of mass from the joint can be determined from a single measurement of the joint torque,  $\tau$ , and joint angle,  $\theta$ . That is:

$$m \cdot c = \tau / (g \cdot \cos(\theta))$$

If additional information is desired, such as the magnitude of the link mass independent of its center of mass location, the complete wrench at the joint is required.

Equation 4.1 requires accurate knowledge of the joint torque, which is difficult to obtain without purpose-built joint torque sensors. Most identification theories assume accurate knowledge of the joint torque, ignoring the fact that few manipulators are equipped with joint torque sensors (Khosla and Kanade, 1985; Hsu *et al.*, 1987; Goldenberg *et al.*, 1989). This section will focus on an identification method which is based on feedback from a base force/torque sensor instead of sensed joint torque. It

circumvents the requirement for accurate joint torque sensing, yet allows highly accurate mass parameter identification.

#### 4.2.1 Mass Parameter Identification Theory

A mass property identification theory was formulated which exploits feedback from a base force/torque sensor, and requires reorientation of the manipulator base (West *et al.*, 1989). Reorientation of the manipulator base is not always practical or desirable. A modified version of this theory, which allows the manipulator base to remain fixed, is presented here. It should be noted that reorienting the base allows the identification of additional mass parameters (such as the total manipulator mass). For control of fixed-base manipulators, however, this information is unnecessary.

Consider an  $n$ -joint manipulator mounted on a six-axis base force/torque sensor, as shown in Figure 2.3. The manipulator has  $n+1$  links, where link 0 and link  $n+1$  represent the base and the terminal link, respectively. The wrench measured by the base force sensor is denoted as  $w$ . We will assume that link 1 is rigid and immobile. Under this assumption, it is desirable to express the base wrench  $w$  at an inertial frame fixed at joint 1. The wrench at joint 1,  $w_1$ , can be obtained as:

$$w_1 = Tw \quad (4.2)$$

where  $T$  is a force/moment transformation matrix (Craig, 1986).

A local coordinate system is fixed at the joint of each link  $i$ . With respect to this coordinate system, the three mass parameters of link  $i$  are denoted as follows:

$$\phi = \begin{bmatrix} m_i r_{xi} \\ m_i r_{yi} \\ m_i r_{zi} \end{bmatrix} \quad (4.3)$$

where  $m_i$  is the mass of link  $i$ . The coordinates  $(r_{xi}, r_{yi}, r_{zi})$  are of the center of mass of link  $i$  with respect to joint  $i$ .

Note that for a multi-link manipulator, the mass parameters in the vector  $\phi$  may consist of a group of several parameters. This occurs if the parameters are unidentifiable individually (An *et al.*, 1985; An 1988). That is, the grouped components always influence the base wrench in a coupled manner, and their individual influence on the robot dynamics cannot be determined. However, this grouping does not affect gravity compensation or robot modeling, since these grouped parameters must occur together in any static equations. (A more detailed discussion of parameter grouping will be presented in Section 4.3.1).

The wrench at joint 1 is related to the mass parameters of the links as:

$$w_1 = U\phi \quad (4.4)$$

where  $U$  is a matrix determined by kinematics and joint position of the manipulator, and can be determined from static equilibrium equations. The vector  $\phi$  represents the mass parameters of links 1 through  $n$ . A detailed derivation of Equation 4.4 can be found in the literature (An *et al.*, 1985; An, 1988).

Combining Equations 4.2 and 4.4 yields:

$$w = T^{-1}U\phi \quad (4.5)$$

Denoting

$$y = T^{-1}U \quad (4.6)$$

gives

$$w = y \phi \quad (4.7)$$

When  $m$  measurements are used, the elements of Equation 4.7 can be augmented as:

$$W = \begin{bmatrix} w(1) \\ w(2) \\ \cdot \\ \cdot \\ w(m) \end{bmatrix} \quad Y = \begin{bmatrix} y(1) \\ y(2) \\ \cdot \\ \cdot \\ y(m) \end{bmatrix} \quad (4.8)$$

Equation 4.7 can then be rewritten as:

$$W = Y\phi \quad (4.9)$$

When the manipulator is moved to different configurations, the components of  $W$  and  $Y$  vary. In theory, if we wish to identify  $r$  mass parameters, the number of different manipulator configurations which must be considered is equal to  $\lceil r/6 \rceil$ , since each measurement supplies six static equations (one from each component of the base wrench). Then, the calculation of the vector  $\phi$  would be accomplished as follows:

$$\phi = Y^{-1} \cdot W \quad (4.10)$$

If  $Y$  is non-square, the matrix least-squares inverse  $(Y^T Y)^{-1} Y^T$  can be used.

In practice, however, the number of measurements which must be taken is greater than  $r/6$ . This is due to the fact that the  $F_x$ ,  $F_y$ ,  $F_z$ , and  $M_z$  components of the base wrench are configuration invariant, and thus do not contribute unique equations. Thus, the theoretical minimum number of configurations required becomes  $\lceil r/2 \rceil$ , since each measurement contributes only two equations, from  $M_x$  and  $M_y$ .

It is intuitively obvious that in order to identify the mass parameters of several manipulator links, each link should be exercised. That is, all joints of the manipulator should move with respect to one another during data collection. This observation leads to a metric on identification which is defined by the condition number of the matrix  $Y^{-1}$  (or  $(Y^T Y)^{-1} Y^T$  if  $Y^{-1}$  does not

exist). An estimate of the magnitude of errors on  $\phi$  caused by measurement errors in  $W$  can then be defined as follows (West *et al.*, 1989):

$$\|\delta\| \leq C\|\phi\| \frac{\|\delta W\|}{\|W\|} \quad (4.11)$$

Where  $C$  is the matrix condition number,  $\delta$  is the error magnitude, and  $\delta W$  is the magnitude of the error vector corresponding to  $W$ . This equation implies that a large condition number could cause some parameters to be greatly influenced by errors in  $W$ . Thus,  $C$  should be as small as possible.

One way to minimize  $C$  is to collect redundant data points. In this case,  $Y$  is non-square and the matrix least-squares inverse  $(Y^T Y)^{-1} Y^T$  is used in the computation of  $P$ . In practice, all joints of interest should move through most of their range of motion. This usually ensures a well-conditioned matrix.

#### 4.2.2 Mass Parameter Identification Experimentation

Mass parameter identification experiments were conducted on the first three joints of a PUMA 550 five d.o.f. manipulator, shown in Figure 2.5. Joints four and five (the wrist joints) were excluded from this analysis due to their small influence on manipulator mass.

As explained in Section 4.2.1, only the  $M_x$  and  $M_y$  components of the base wrench are configuration dependent, and thus contribute independent equations. Thus,  $w$  of Equation 4.7 can be written as:

$$w = \begin{bmatrix} M_x \\ M_y \end{bmatrix} \quad (4.12)$$

The matrix  $y$  was developed from a static analysis of the PUMA (Corrigan, 1994). This matrix relates the base wrench  $w$  and the mass parameter  $\phi$  vector as follows:

$$y = g \begin{bmatrix} s1 & -c1 & s1c2 & -s1s2 & s1c23 & -s1s23 \\ -c1 & -s1 & -c1c2 & c1s2 & -c1c23 & c1s23 \end{bmatrix} \quad (4.13)$$

In this notation,  $(s_i, c_i)$  represents  $(\sin(\theta_i), \cos(\theta_i))$ , and  $(s_{ij}, c_{ij})$  represents  $(\sin(\theta_i + \theta_j), \cos(\theta_i + \theta_j))$ .

The vector of mass parameters,  $\phi$ , was determined by inspection to be:

$$\phi = \begin{bmatrix} m_1 r_{x1} \\ m_1 r_{z1} + m_2 r_{z2} + (m_2 + m_3)d_2 + m_3 r_{z3} + m_3 d_3 \\ m_2 r_{x2} + (m_2 + m_3)a_2 \\ m_2 r_{y2} \\ m_3 r_{x3} + m_3 a_3 \\ m_3 r_{y3} \end{bmatrix} \quad (4.14)$$

Refer to Appendix A for a kinematic description of the PUMA 550.

Numerous experiments were performed, with varying ranges of joint motion. A typical experiment is described below. The first three joints of the PUMA were commanded to follow linear trajectories (in joint space) within the following bounds:

$$\theta_1: -90^\circ \text{ to } -270^\circ \quad \theta_2: -35^\circ \text{ to } 85^\circ \quad \theta_3: 0^\circ \text{ to } -90^\circ$$

The manipulator was stopped at 50 equally-spaced points, and the base wrench  $W$  was compiled. Since 50 data points leads to 100 equations, the matrix  $Y$  was of dimension  $(100 \times 6)$ . This non-square matrix was inverted with the least-squares inversion technique, as follows:

$$\phi = (Y^T Y)^{-1} Y^T \cdot W \quad (4.15)$$

The numerical values of the vector  $P$  were computed as:

$$\phi = \begin{bmatrix} 0.0231 \\ -5.4622 \\ 3.4887 \\ 0.2379 \\ 0.6359 \\ -0.0087 \end{bmatrix}$$

These values are similar to those computed by previous researchers (Armstrong *et al.*, 1986; Corrigan, 1994). This comparison can be seen in Table 4.1. The discrepancy in the term  $(m_3 r_{3x} + m_3 a_3)$  is due to the fact that the

reported data is for a PUMA 560 manipulator, which contains an additional wrist joint, and thus an additional motor in link three. The term  $(m_2 r_{2x} + (m_2 + m_3) a_2)$  is also influenced by this additional motor.

	Experimentally Determined Parameters	Previously Determined Values (Corrigan)	Physically Measured Values (Armstrong)
$m_1 r_{x1}$	0.0231	0.1593	0
$m_1 r_{z1} + \dots$	-5.4622	-5.8440	-5.3080
$m_2 r_{x2} + \dots$	3.4487	4.6137	5.0650
$m_2 r_{y2}$	0.2379	0.1298	-0.1044
$m_3 r_{x3} + m_3 a_3$	0.6359	2.2527	2.6170
$m_3 r_{y3}$	-0.0087	-0.0738	0

Table 4.1: Comparison of Mass Parameter Values

However, comparison to published data is an inconclusive test of the method's accuracy, since several researchers have reported substantially different values for PUMA mass parameters (Corke, 1994). Thus, the identified mass parameters must be verified by more direct methods.

The accuracy of the computed parameters was verified by comparing the measured moment vector (i.e. the data from the base sensor) with a predicted moment vector. The predicted moment vector was calculated off-line using a calculated  $\phi$  vector and knowledge of the robot joint positions along a trajectory. That is, the measured moment vector was compared to the product  $((Y^T Y)^{-1} Y^T \cdot \phi)$  at each point along the trajectory. The results of this comparison can be seen in Figures 4.2 and 4.3.



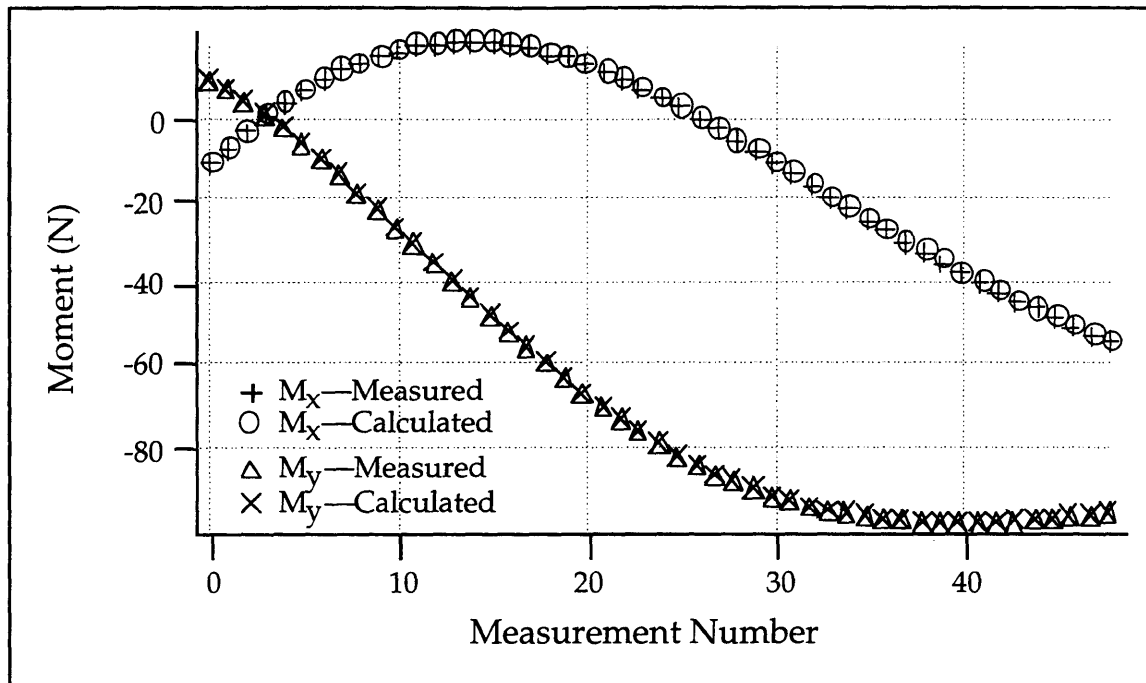


Figure 4.2: Comparison of Measured and Computed  $M_x$  and  $M_y$

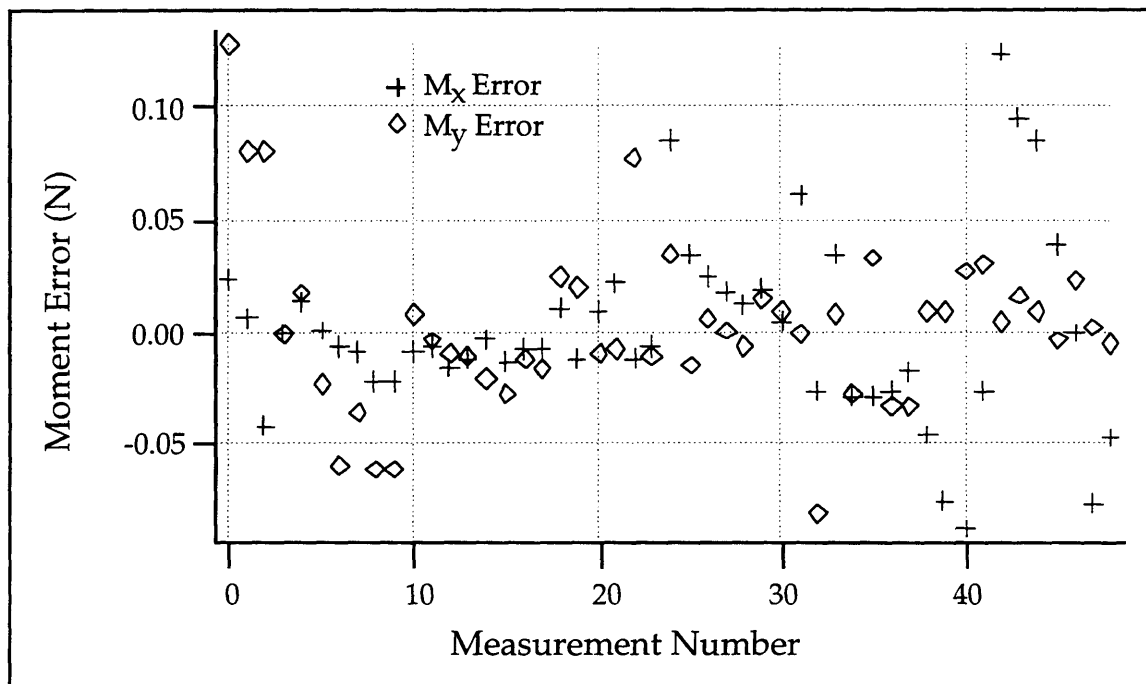


Figure 4.3: Error Between Measured and Computed  $M_x$  and  $M_y$

Notice the excellent agreement between measured and predicted moments. The “random” appearance of Figure 4.3 implies that no systematic errors are present in the estimation process. It is therefore safe to conclude

that the computed parameters will be effective in a gravity compensation scheme, or a static manipulator model.

Table 4.2 numerically presents the results of Figures 4.2 and 4.3. Since the noise level of the AMTI sensor is approximately 0.5 N-m, we can conclude that the estimation accuracy has surpassed the level of measurement noise (Corrigan, 1994). It should be noted that this level of accuracy is achievable due to oversampling and averaging. This is possible since during mass parameter identification experiments, data collection time is not constrained.

	RMS Error (N-m)	Maximum Error (N-m)
$M_x$	0.0403	0.1233
$M_y$	0.0367	0.1275

Table 4.2: Comparison of Measured and Computed Moment Vector

### 4.3 Manipulator Inertial Parameter Identification

Inertial parameter identification refers to the determination of masses, center of mass locations, and moments of inertia of the links of a manipulator. Mass parameter identification can thus be viewed a subset of inertial parameter identification. Inertial parameters are important for dynamic manipulator modeling and model-based control schemes, but are not usually known by robot manufacturers. Thus, methods to identify these parameters have been developed (An *et al.*, 1985; Khosla and Kanade, 1985; Gautier and Khalil, 1990).

Unlike mass parameter identification, inertial parameter identification requires that data be collected during manipulator motion, since inertia is a dynamic property. Therefore, the methods for identifying inertial parameters are fundamentally different from methods for identifying mass parameters.

Let us return to the one link example of Figure 4.1 to demonstrate this. In this case, we assume the manipulator is accelerating at a rate  $\alpha$ .

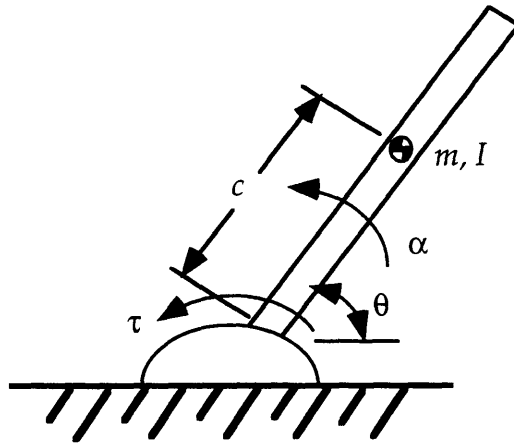


Figure 4.4: A One Degree-Of-Freedom Dynamic Manipulator

The relationship between torque and link mass is:

$$\tau = m \cdot g \cdot c \cdot \cos(\theta) + I \cdot \alpha \quad (4.9)$$

Unlike Equation 4.1, this equation has two unknown quantities: the product  $m \cdot c$ , and the link inertia  $I$ . However, the problem is not indeterminate, since it can be solved as long as multiple data points are available.

Examining Equation 4.9, we can see that knowledge of both joint torque and joint acceleration are required. Joint torque measurement difficulties have been discussed in Section 4.2 and Chapter 2. Acceleration measurements are difficult to obtain due to noise amplification that is inherent in numerical differentiation.

Difficult theoretical issues of inertial property identification can be observed in this simple example. One issue involves the joint motion: how fast does the link need to accelerate in order to obtain a “good” estimate of the mass properties? (And, for a multi-link robot, what level of velocity must be obtained?) What motion profile leads to a “good” estimate? Another question is of inertial parameter grouping: do inertial parameters occur in

“groups” (as they did in mass parameter identification), and if so, how can we identify these groups?

The answers to these questions are intuitively less obvious than they were for mass parameter identification, since they require examination of the dynamics of a multi-d.o.f. manipulator. The following section will address these issues, while developing a generalized inertial parameter estimation procedure.

### 4.3.1 Inertial Property Identification Theory

An inertial property identification theory was formulated which utilizes data from a base force/torque sensor (Liu *et al.*, 1997). This theory is presented here for completeness.

Consider again the  $n$ -joint manipulator mounted on a six-axis base force/torque sensor, as shown in Figure 2.3. The wrench at joint 1,  $w_1$ , can be obtained as:

$$w_1 = Tw \tag{4.10}$$

where  $T$  is a force/moment transformation matrix (Craig, 1986).

A local coordinate system is fixed at the joint of each link  $i$ . With respect to this coordinate system, the ten inertial parameters of link  $i$  are denoted as follows:

$$\phi = \begin{bmatrix} m_i \\ m_i r_{xi} \\ m_i r_{yi} \\ m_i r_{zi} \\ I_{xxi} \\ I_{xyi} \\ I_{xzi} \\ I_{yyi} \\ I_{yzi} \\ I_{zzi} \end{bmatrix} \tag{4.11}$$

where  $m_i$  is the mass of link  $i$ . The coordinates  $(r_{xi}, r_{yi}, r_{zi})$  are of the center of mass of link  $i$  with respect to joint  $i$ . The elements of the inertia tensor of link  $i$  about joint  $i$  are represented by  $(I_{xxi}, I_{xyi}, I_{xzi}, I_{yyi}, I_{yzi}, I_{zzi})$ . It should be noted that the inertia tensor is expressed with respect to the joint, not the center of mass of the link.

The wrench at joint 1 is related to the inertial parameters of the links as:

$$w_1 = U\phi \quad (4.12)$$

The vector  $\phi$  represents the inertial parameters of all links. The matrix  $U$  is a matrix determined by the kinematics, joint velocity and acceleration of the manipulator. Since it relates the base wrench to joint motion,  $U$  can be determined by writing the dynamic equations of motion for the manipulator with respect to a reference frame fixed at the sensor center.

Combining Equations 4.10 and 4.12 yields:

$$w = T^{-1}U\phi \quad (4.13)$$

Denoting

$$y = T^{-1}U \quad (4.14)$$

gives

$$w = y\phi \quad (4.15)$$

When  $m$  measurements are used, the elements of Equation 4.7 can be augmented as:

$$W = \begin{bmatrix} w(1) \\ w(2) \\ \cdot \\ \cdot \\ w(m) \end{bmatrix} \quad Y = \begin{bmatrix} y(1) \\ y(2) \\ \cdot \\ \cdot \\ y(m) \end{bmatrix} \quad (4.16)$$

Equation 4.15 can then be rewritten as:

$$W = Y\phi \quad (4.17)$$

This equation is identical to Equation 4.9. Note, however, that the matrix  $Y$  includes dynamics terms (i.e.  $Y = f(q, \dot{q}, \ddot{q})$ ), where in Equation 4.9 it contained only static terms ( $Y = f(q)$ ).

The vector  $\phi$  can generally be estimated from Equation 4.17 using the least-squares method as:

$$\phi = (Y^T Y)^{-1} Y^T W \quad (4.18)$$

However, the least-squares method may not be applied directly when  $(Y^T Y)^{-1}$  does not exist. In this case, the ridge regression or singular value decomposition methods can be used to solve this problem. Ridge regression is a technique which makes  $(Y^T Y)$  invertible by adding a small number  $d$  to the diagonal elements. Singular value decomposition is a technique which reformulates the matrix  $Y$  in terms of a diagonal matrix  $\Sigma$  and two orthogonal matrices  $U$  and  $V$ . This new matrix is invertible. More detail on these methods can be found in the literature (Marquardt and Snee, 1975; Golub and Van Loan, 1983).

#### *1) Elimination of the Acceleration Requirement*

To compute the elements of  $Y$  in Equation 4.17, knowledge of joint acceleration is required. However, it is difficult to measure manipulator joint acceleration directly, and estimating acceleration with position or velocity signals is usually difficult due to noise. A low-pass filter transformation can help overcome this problem (Goldenberg *et al.*, 1989; Liu and Goldenberg, 1996). Applying a low-pass filter with unity DC gain to both sides of Equation 4.17 yields:

$$(W)_i = (Y)_i \phi \quad (4.19)$$

where

$$(\cdot)_l = L^{-1}\left[\frac{l}{s+l}L[\cdot]\right] \quad (4.20)$$

where  $L[\cdot]$  and  $L^{-1}[\cdot]$  represent the Laplace transform and the inverse Laplace transform respectively, and  $l$  is a positive constant.

Since acceleration terms in  $Y$  appear only in conjunction with functions of the joint angles  $q$ , a term containing  $\ddot{q}$  can be generally represented by  $f(q)\ddot{q}_j$  (Hsu *et al.*, 1987). Its Laplace transform is:

$$L[f(q)\ddot{q}_j] = sL[f(q)\dot{q}_j] - L\left[\sum_{i=1}^n \frac{\partial f(q)}{\partial q_i} \dot{q}_i \dot{q}_j\right] \quad (4.21)$$

Applying the low-pass filter to both sides of Equation 4.21 leads to (Hsu *et al.*, 1987; Liu and Goldenberg, 1996):

$$\begin{aligned} \frac{l}{s+l}L[f(q)\ddot{q}_j] &= \frac{l}{s+l}sL[f(q)\dot{q}_j] - \frac{l}{s+l}L\left[\sum_{i=1}^n \frac{\partial f(q)}{\partial q_i} \dot{q}_i \dot{q}_j\right] \\ &= l\left(1 - \frac{l}{s+l}\right)L[f(q)\dot{q}_j] - \frac{l}{s+l}L\left[\sum_{i=1}^n \frac{\partial f(q)}{\partial q_i} \dot{q}_i \dot{q}_j\right] \end{aligned} \quad (4.22)$$

Applying an inverse Laplace transformation to both sides of Equation 4.22 yields:

$$(f(q)\ddot{q}_j)_l = l[f(q)\dot{q}_j - (f(q)\dot{q}_j)_l] - \left(\sum_{i=1}^n \frac{\partial f(q)}{\partial q_i} \dot{q}_i \dot{q}_j\right) \quad (4.23)$$

Thus, no acceleration term appears on the right-hand side of Equation 4.22. This greatly simplifies the practical implementation of the identification method.

## II) Filtering of Velocity Measurement Noise

The first term of the right-hand side of Equation 4.23 is actually the difference between the unfiltered and filtered values of  $f(q)\dot{q}_j$ , multiplied by the filter parameter  $l$ . This term is sensitive to the noise that is inevitably

present in the computed joint velocity,  $\dot{q}_j$ . For example, when  $f(q)=1$ , Equation 4.23 becomes:

$$(f(q)\ddot{q}_j)_l = (\ddot{q}_j)_l = l[\dot{q}_j - (\dot{q}_j)_l] \quad (4.24)$$

which could be dominated by measurement noise when the low-pass filter bandwidth parameter  $l$  is large.

To overcome this problem, the transformation defined by Equation 4.20 is applied again to Equation 4.19:

$$((W)_d)_d = ((Y)_d)_d \phi \quad (4.25)$$

where  $d$  is another positive constant that determines the bandwidth of this second low-pass filter.

After applying the second low-pass filter, Equation 4.23 becomes:

$$((f(q)\ddot{q}_j)_d)_d = l[(f(q)\dot{q}_j)_d - ((f(q)\dot{q}_j)_d)_d] - \left( \sum_{i=1}^n \frac{\partial f(q)}{\partial q_i} \dot{q}_i \dot{q}_j \right)_d \quad (4.26)$$

And Equation 4.24 becomes:

$$((f(q)\ddot{q}_j)_d)_d = ((\ddot{q}_j)_d)_d = l[(\dot{q}_j)_d - ((\dot{q}_j)_d)_d] \quad (4.27)$$

Equation 4.25 is used to estimate  $\phi$  using the least squares technique.

When  $[((Y^T)_d)_d((Y)_d)_d]^{-1}$  exists, we can estimate  $\phi$  using :

$$\phi = [((Y^T)_d)_d((Y)_d)_d]^{-1}((Y^T)_d)_d((W)_d)_d \quad (4.28)$$

As described earlier, the ridge regression or singular value decomposition methods must be used when  $[((Y^T)_d)_d((Y)_d)_d]^{-1}$  does not exist.

When implementing the parameter identification algorithm, it is clear the parameter  $d$  should be set high compared to  $l$ . It should be low enough, however, to filter out velocity measurement noise. This will be demonstrated in the experimental results presented in Section 4.3.2.



### III) Elimination of the Effect of Sensor Offset

It is assumed in the previous analysis that the wrench  $w$  is caused by the dynamic motion of the manipulator. However, undesirable output offsets usually exist in strain gage force/moment sensors, due to mismatched electronics or mechanical preloading. In most cases, these offsets can be eliminated by measuring the sensor output at zero load, and removing this measurement from future readings. In our case, however, a manipulator is bolted to the base sensor, and thus it is impossible to measure the sensor output at zero load. The sensor offset could be measured by removing the manipulator from the base sensor, but this is impractical.

The dynamic wrench is also corrupted by the presence of a gravity-induced wrench. This wrench can be compensated for with gravity compensation techniques (Corrigan, 1994). However, although these methods are accurate, a more direct method is desired.

In summary, the base sensor output contains the motion-related wrench, gravity-induced wrench, and sensor offset. That is:

$$w_s = w_m + (w_g + w_o) \quad (4.29)$$

where  $w_m$  is the “dynamic” (i.e. motion-related) wrench, which is zero when the manipulator is stationary. The wrench caused by gravity,  $w_g$ , is mixed with the sensor offset,  $w_o$ .

The effect of sensor offset can be eliminated by extracting the motion-related wrench from Equation 4.29:

$$w_m = w_s - (w_g + w_o) \quad (4.30)$$

where  $w_s$  is measured during robot motion along a given trajectory. Since  $(w_g + w_o)$  depends only on the position of the manipulator, it can be measured as follows: the manipulator is controlled to move along the “dynamic” trajectory, but is stopped at each sampling position, and the sensor output is recorded. This “static” output corresponds to the  $(w_g + w_o)$  term of Equation 4.30, and can simply be subtracted from the “full” wrench.

Without gravity, Equation 4.15 becomes:

$$w_m = y_m \phi \quad (4.31)$$

For  $m$  sampling points:

$$W_m = \begin{bmatrix} w_m(1) \\ w_m(2) \\ \cdot \\ \cdot \\ w_m(m) \end{bmatrix} \quad Y_m = \begin{bmatrix} y_m(1) \\ y_m(2) \\ \cdot \\ \cdot \\ y_m(m) \end{bmatrix} \quad (4.32)$$

From Equation 4.31:

$$W_m = Y_m \phi \quad (4.33)$$

The identification algorithm, Equation 4.28, can then be modified using Equation 4.31 as:

$$\hat{\phi} = [((Y_m^T)_l)_d ((Y_m)_l)_d]^{-1} ((Y_m^T)_m)_d ((W_m)_l)_d \quad (4.34)$$

### 4.3.2 Inertial Parameter Identification Experimentation

Experiments were performed on a PUMA 550 robot arm, using only the first two joints. The manipulator was mounted on an AMTI six-axis force/torque sensor as shown in Figure 2.5. During the experiments, joints three, four, and five were immobilized, in the following configuration:  $q_3 = -142.1^\circ$ ,  $q_4 = 0^\circ$ ,  $q_5 = 0^\circ$ . Joint positions were measured with the PUMA's optical encoders, and joint velocities were computed off-line via forward differentiation of the position data. The sampling rate for the experiments was eight milliseconds.

For the coordinate system illustrated in Figure 2.5, the equations relating manipulator motion to the wrench exerted at the first joint were expressed in Equation 4.17 as:

$$W = Y\phi$$

where

$$W = \begin{bmatrix} F_x \\ F_y \\ F_z \\ M_x \\ M_y \\ M_z \end{bmatrix}$$

is a single measurement of the base sensor wrench, transformed to the origin of the  $\langle xyz1 \rangle$  coordinate system via a simple force/moment transformation. This transformation is performed under the assumption that the trunk of the PUMA is rigid. Thus, the transformation removes a constant term ( $d_0+d_1$ ) from the equations of the matrix  $Y$ . The elements of  $Y$  are given in Appendix C. The inertial parameter vector  $\phi$  is given by:

$$\phi = \begin{bmatrix} m_1 r_{x1} \\ m_1 r_{z1} + \beta m_2 \\ \alpha m_2 \\ m_2 r_{y2} \\ I_{xy1} \\ I_{yy1} + m_2 d_2^2 + 2d_2 m_2 r_{z2} + I_{xx2} \\ I_{yz1} \\ I_{xy2} \\ I_{xz2} \\ I_{yy2} - I_{xx2} \\ I_{yz2} \\ I_{zz2} \end{bmatrix}$$

where  $\alpha = a_2 + r_{x2}$  and  $\beta = d_2 + r_{z2}$ .

Note that some of the elements of  $\phi$  appear as sets of grouped parameters. These groups are usually determined through the use of energy-based methods (Siciliano *et al.*, 1996). In our case, the minimum parameter set was obtained analytically, by performing QR decomposition on the matrix  $Y$  (Siciliano *et al.*, 1996). Both the matrix formulation and QR decomposition

were accomplished with the aid of the symbolic processor Maple. After QR decomposition is performed, it is easy to observe the numerical interdependence of the columns of  $Y$ , and thus identify parameter groups.

The excitation trajectories of the two joints are shown in 4.5 and 4.6. The determination of “exciting” trajectories for real-world identification experiments is in itself a research topic (Gautier and Khalil, 1992). In our experiments, the excitation trajectories were designed with the aid of a MATLAB simulation. A simulated PUMA system (identical to the one described in Chapters 2 and 3) was asked to follow numerous different high-acceleration, high-velocity trajectories, and inertial parameters were computed based on the simulated base wrench. Suitably exciting trajectories were those which yielded well-conditioned ( $Y^T Y$ ) matrices (Siciliano *et al.*, 1996).

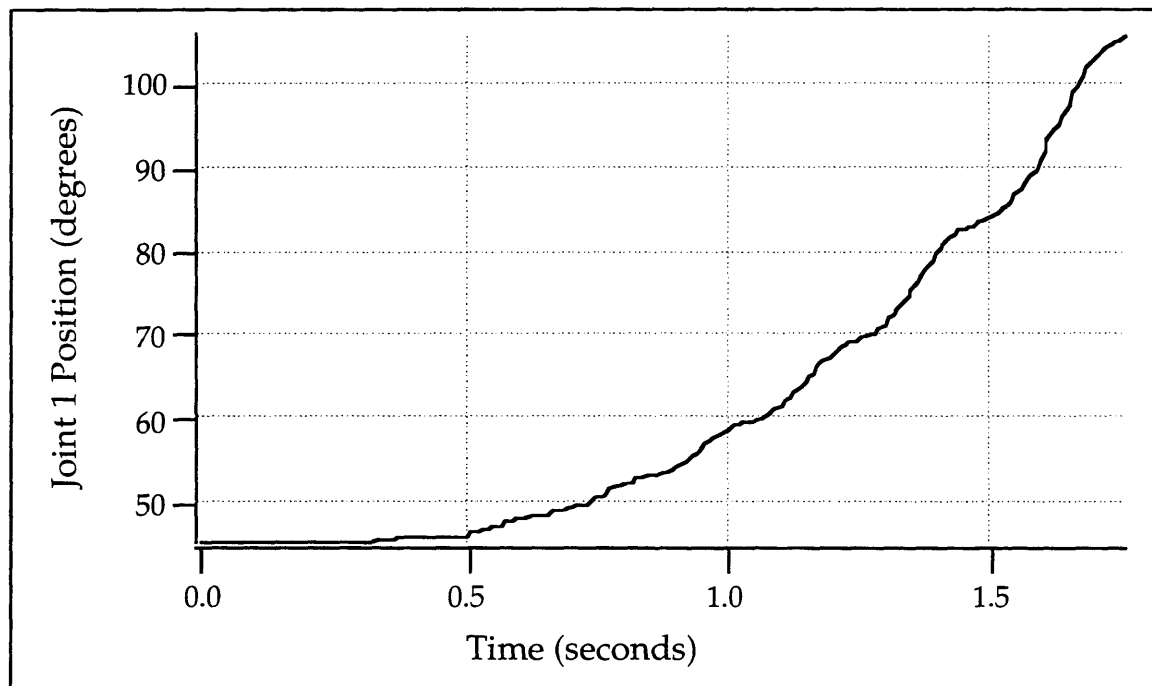


Figure 4.5: Excitation Trajectory—Joint One

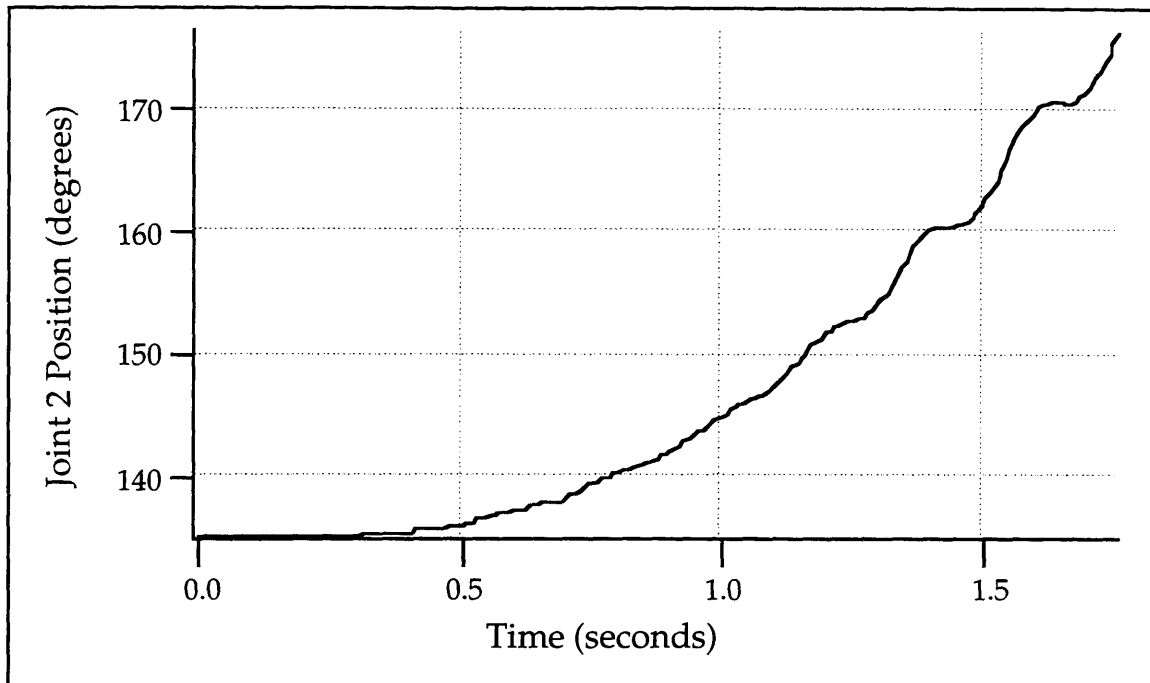


Figure 4.6: Excitation Trajectory—Joint Two

The identification algorithm of Equation 4.34 was implemented using Matlab. Filter parameters were chosen to minimize the effect of sensor noise while maintaining reasonable signal bandwidth. For the filter parameters  $l=1$ ,  $d=50$ , the following estimate of  $\phi$  was obtained:

$$\phi = \begin{bmatrix} 0.1125 \\ -4.2455 \\ 2.2202 \\ -0.1834 \\ -0.2278 \\ 1.2489 \\ 0.1338 \\ 0.1213 \\ -0.1247 \\ 0.8596 \\ -0.0086 \\ 0.9867 \end{bmatrix}$$

Although there is data in the literature for inertial parameter identification of a PUMA 560, it is not applicable to these experiments, since only the first two joints of the PUMA were exercised. Thus, in our experiments the mass and inertial properties of the second “link” contain contributions from the third link. Also, the PUMA 560 differs slightly from the PUMA 550 used in the experiments, as it contains an additional wrist motor. A more direct means of verifying the experimental results must therefore be employed. This verification is the focus of the following section.

### *1) Inertial Parameter Identification Verification*

To verify the results of the previous section, the estimated inertial parameters were used to predict the output of the base force/torque sensor for a completely different trajectory, shown in Figures 4.7 and 4.8. The base wrench during this trajectory was measured, and compared to a predicted wrench. The predicted wrench was computed as  $((Y_m)_1)_d \phi$ , where  $\phi$  is the vector of estimated inertial parameters. Filtering is performed as in previous experiments (i.e. the same filter parameters were used for all experiments).

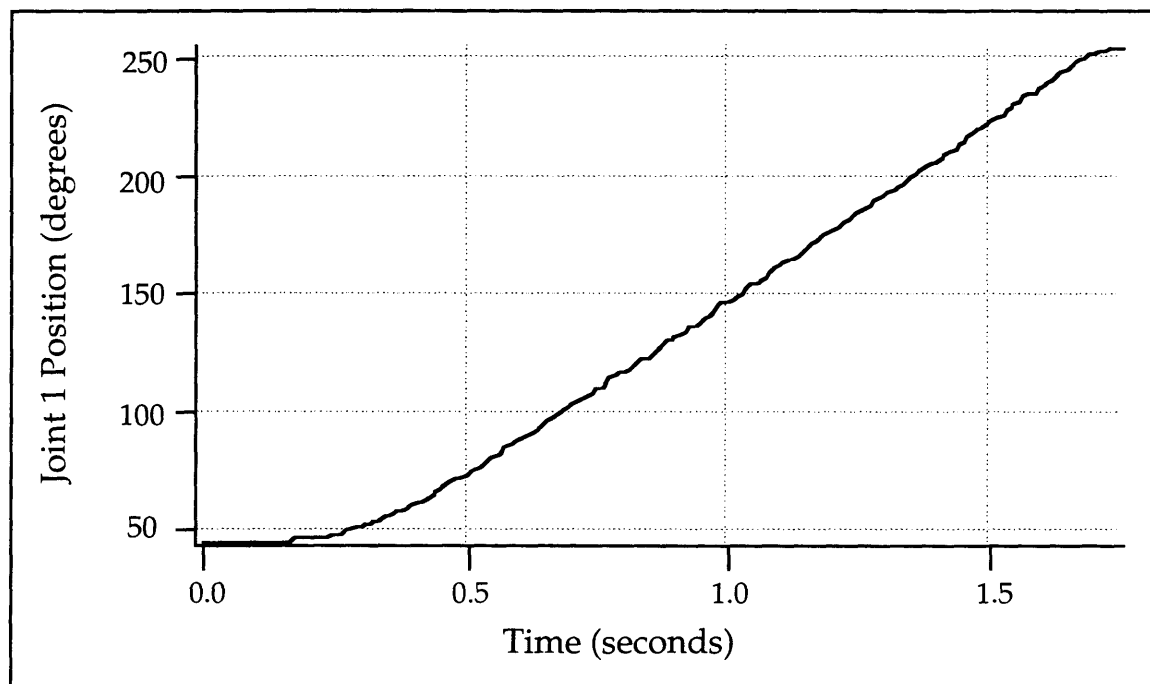


Figure 4.7: Verification Trajectory—Joint One

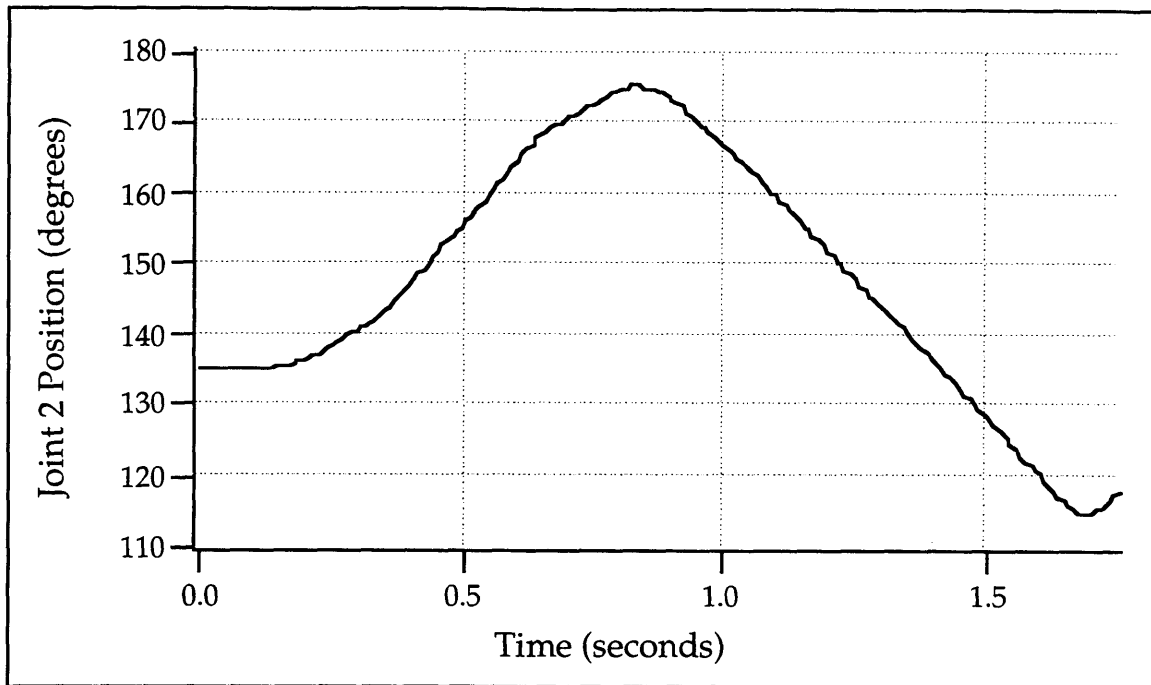


Figure 4.8: Verification Trajectory—Joint Two

The predicted base wrench agrees well with the measured base wrench. This can be observed in Figure 4.9a-g.

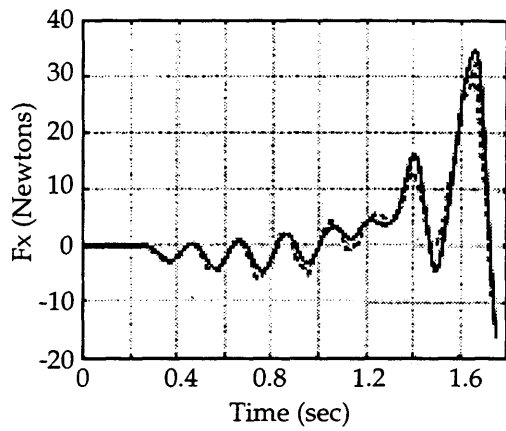


Figure 4.9a

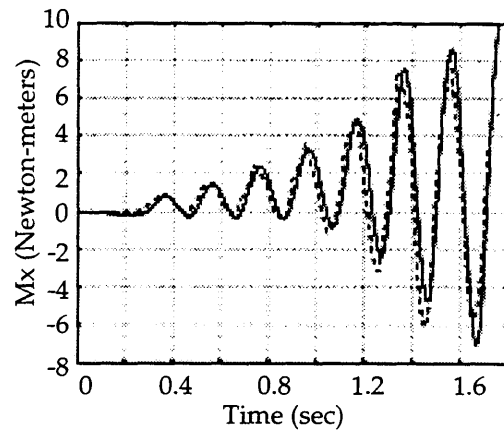


Figure 4.9d

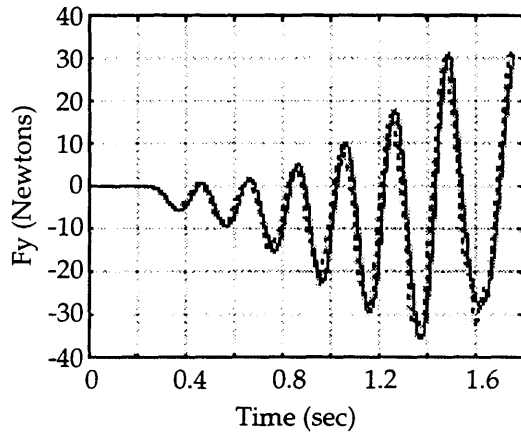


Figure 4.9b

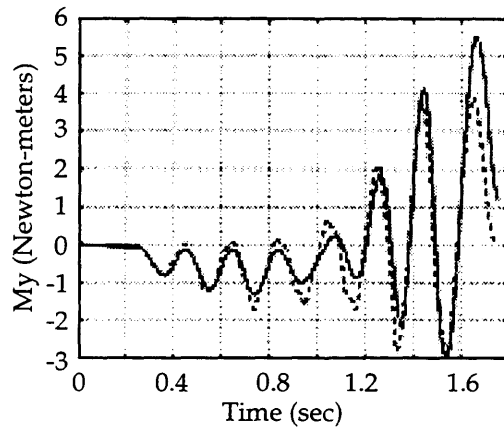


Figure 4.9e

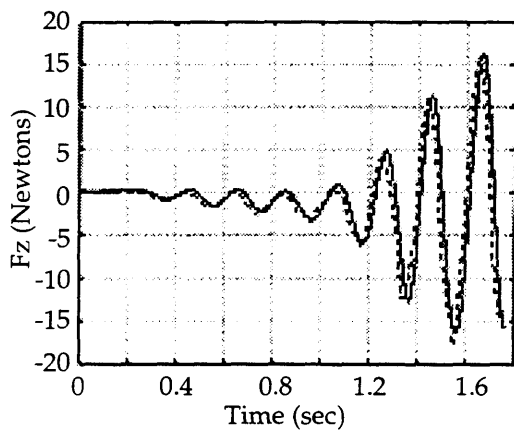


Figure 4.9c

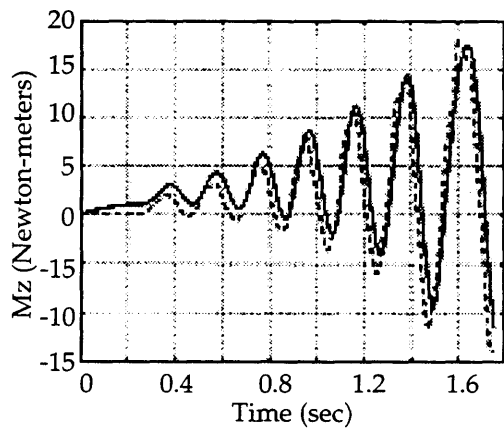


Figure 4.9f

Figure 4.9: Comparison of Predicted and Measured Forces and Torques  
(Solid Line: Measured; Dashed Line: Predicted)



## 4.4 Summary and Conclusions

This chapter presented an approach to both mass and inertial parameter identification which exploits feedback from the base force/torque sensor. The fundamental problems of parameter identification were discussed, and a theoretical framework was presented for each method. Experimental results were then presented, which showed that both methods are capable of achieving high levels of accuracy.

Unmodeled joint friction does not degrade the accuracy of the results, since the method does not use motor current to estimate the joint torque, but rather a direct measurement from the base sensor. The mass parameter estimation process is simple to implement, and the error is potentially less than the sensor noise level, due to the sensor data averaging.

# Chapter 5

## Conclusions and Suggestions for Further Work

### 5.1 Contributions of This Work

This thesis described the application of a base-mounted force/torque sensor to manipulator identification and control. Simulation and experimental data were presented which show the utility of base-sensor feedback in precision position and force control, and manipulator mass and inertial parameter identification.

Simulation and experimental studies of fine-motion position control of both a PUMA 550 and a Schilling Titan II manipulator were described. Simulation results for a PUMA 550 manipulator executing fine-motion tasks were presented and shown to be consistent with experimental results, confirming the validity of the simulation. Extensive experimental results for the Schilling Titan II system were presented, for unloaded free motion tasks, and free motion tasks with a payload. The results showed substantial improvement over conventional control schemes.

Simulation and experimental studies of torque control and implicit force control were then presented. The theoretical framework for both control methods was discussed, and predictions were made regarding system performance. Simulation results for both types of force control were presented. Experimental results were then presented which largely agreed with the simulation results.

Torque control with a dominant-pole filter was shown to be an accurate, stable force control method. Implicit force control was shown to

allow high force control resolution, although its accuracy is limited. Force resolution, however, can reach the sub-Newton level with base-sensor feedback. Implicit force control was also found to be stable during contact, even against a stiff environment. It was shown that “real-world” effects, such as numerical differentiation and sensor noise, hindered the experimental systems.

Unique approaches to both mass and inertial parameter identification were presented, which exploit feedback from the base force/torque sensor. The fundamental problems of parameter identification were discussed, and a theoretical framework was presented for each method. Experimental results were then presented, which showed that both methods are capable of achieving high levels of accuracy.

Unmodeled joint friction does not degrade the accuracy of the results, since the method does not rely on estimates of the joint torque. The mass parameter estimation process is simple to implement, and the error is potentially less than the sensor noise level, due to the sensor data averaging.

## **5.2 Suggestions for Further Work**

This thesis has shown that feedback from a base force/torque sensor can greatly improve manipulator performance for delicate position and force control, and can allow highly accurate parameter identification. Although substantial work has been completed in these areas, the unexplored potential of base-sensor feedback remains considerable.

Optimization of the torque control loop has yet to be performed. To date, a simple integral-type compensator has been employed, and controller tuning has been largely empirical. Although excellent results have been obtained, advanced controller design techniques should lead to further performance enhancement.

In the area of position control, experimentation with fully dynamic torque estimation has not yet been performed. Dynamic torque estimation would require knowledge of joint acceleration, which could limit its usefulness. However, with sufficiently high-quality sensors and fast sampling, an acceleration estimator could be constructed. Although some error would likely result in the torque estimation, system performance would still be greatly improved.

In the area of force control, it is clear that explicit force control could be performed with the base force/torque sensor. Hybrid control could also be benefited by base-sensor feedback. With the addition of a wrist-sensor to the manipulator, a system could be developed which is able to perform both high-precision closed-loop force control, and high-precision position control.

Base-sensor feedback could also be used to improve performance in master-slave teleoperated systems. A master arm with torque feedback would appear virtually frictionless to the operator, and would thus allow improved positioning performance of the slave arm.

In the area of parameter identification, further work remains in the area of identifiability of inertial parameters. An energy-based algorithm for computing the minimum set of inertial parameters is conceivable, similar to those found in the literature (Siciliano *et al.*, 1996).

## References

- An, C.H., Atkeson, C.G. and Hollerbach, J.M., "Estimation of Inertial Parameters of Rigid Body Links of Manipulators," *Proceedings of the 24<sup>th</sup> IEEE Conference on Decision & Control*, pp. 990-995, December 1985
- An, C.H., *Model-Based Control of a Robot Manipulator*, MIT Press, Cambridge, USA 1988
- Armstrong, B., Khatib, O., and Burdick, J., "The Explicit Dynamic Model and Inertial Parameters of the PUMA 560 Arm," *Proceedings of the IEEE International Conference on Robotics and Automation*, pp. 510-518, April 1986
- Armstrong, B., *Control of Machines with Friction*, Kluwer Academic Publishers, Boston, USA 1991
- Asada, H., Youcef-Toumi, K., *Direct-Drive Robots: Theory and Practice*, MIT Press, Cambridge, USA 1987
- Baker, J., *Gravity Compensation for Experiments in Space Robotics*, S.M. Thesis, Department of Mechanical Engineering, Massachusetts Institute of Technology, Cambridge, USA 1992
- Canudas de Wit, C., Olsson, H., Astrom, K.J., and Lischinsky, P., "A New Model for Control of Systems with Friction", *IEEE Transactions on Automatic Control*, Vol. 40, No. 3, pp. 419-425, 1996
- Corke, P., *The Unimation Puma Servo System*, Report MTM-226, CSIRO Division of Manufacturing Technology, Australia 1994

- Corrigan, T., *Implementation and Application of Methods for Micro-Gravity Emulation*, S.M. Thesis, Department of Mechanical Engineering, Massachusetts Institute of Technology, Cambridge, USA 1994
- Craig, J., *Introduction to Robotics*, Addison-Wesley, New York, USA 1986
- Craig, J., *Adaptive Control of Mechanical Manipulators*, Addison-Wesley, New York, USA 1988
- Dubowsky, S., "Robot Assisted Crucible Charging System One Year Progress Report," MIT Internal Report, 1996
- Durfee, W.K., Idris, H.R., and Dubowsky, S., "Real-Time Control of the MIT Vehicle Emulation System," *Proceedings of the American Control Conference*, 1991
- Electricité de France, Private Correspondence, 1996
- Gautier, M. and Khalil, W., "Direct Calculation of Minimum Set of Inertial Parameters of Serial Robots," *IEEE Transactions on Robotics and Automation*, Vol. 6, No. 3, pp. 368-373, June 1990
- Gautier, M. and Khalil, W., "Exciting Trajectories for Inertial Parameter Identification," *International Journal of Robotics Research*, Vol. 11, pp. 362-375, 1992
- Goldenberg, A.A., Apkarian, J.A. and Smith, H.W., "An Approach to Adaptive Control of Robot Manipulators Using the Computed Torque Technique," *ASME Journal of Dynamic Systems, Measurement, and Control*, Vol. 111, pp. 1-8, 1989
- Golub, G.H., and Van Loan, C.F., *Matrix Computations*, John Hopkins University Press, 1983

- Habibi, S.R., Richards, R.J., and Goldenberg, A.A., "Hydraulic Actuator Analysis for Industrial Robot Multivariable Control," *Proceedings of the American Control Conference*, pp. 1003-1007, 1994
- Heinrichs, B., Sepehri, N., Thornton-Trump, A.B., "Position-Based Impedance Control of an Industrial Hydraulic Manipulator," *Proceedings of the IEEE International Conference on Robotics and Automation*, Vol. 1, pp. 284-290, 1996
- Hsu, P., Bodson, M., Sastry, S. and Paden, B., "Adaptive Identification and Control for Manipulators without Using Joint Accelerations," *Proceedings of IEEE International Conference on Robotics and Automation*, pp. 1210-1215, 1987
- Khosla, P. and Kanade, T., "Parameter Identification of Robot Dynamics," *Proceedings of the 24<sup>th</sup> IEEE Conference on Decision & Control*, pp. 1754-1760, December 1985
- Kuklinski, A., *The Practical Implementation of an Experimental Tool for the Dynamic Interactions in Mobile Manipulator Systems*, S.M. Thesis, Department of Mechanical Engineering, Massachusetts Institute of Technology, Cambridge, USA 1993
- Liu, G. and Goldenberg, A.A., "Uncertainty Decomposition-Based Robust Control of Robot Manipulators," *IEEE Transactions on Control System Technology*, Vol. 4, No. 4, pp. 384-393, July 1996
- Liu, G., Iagnemma, K., Morel, G., and Dubowsky, S., "A Base Force/Torque Sensor Approach to Estimation of Inertial Parameters of Robot Manipulators," Submitted for publication in: *Journal of Mechanism and Machine Theory*, 1997
- Lu, Z., Shimoga, K.B. and Goldenberg, A.A., "Experimental Determination of Dynamic Parameters of Robotic Arms," *Journal of Robotic Systems*, Vol. 10, pp. 1009-1029, 1993

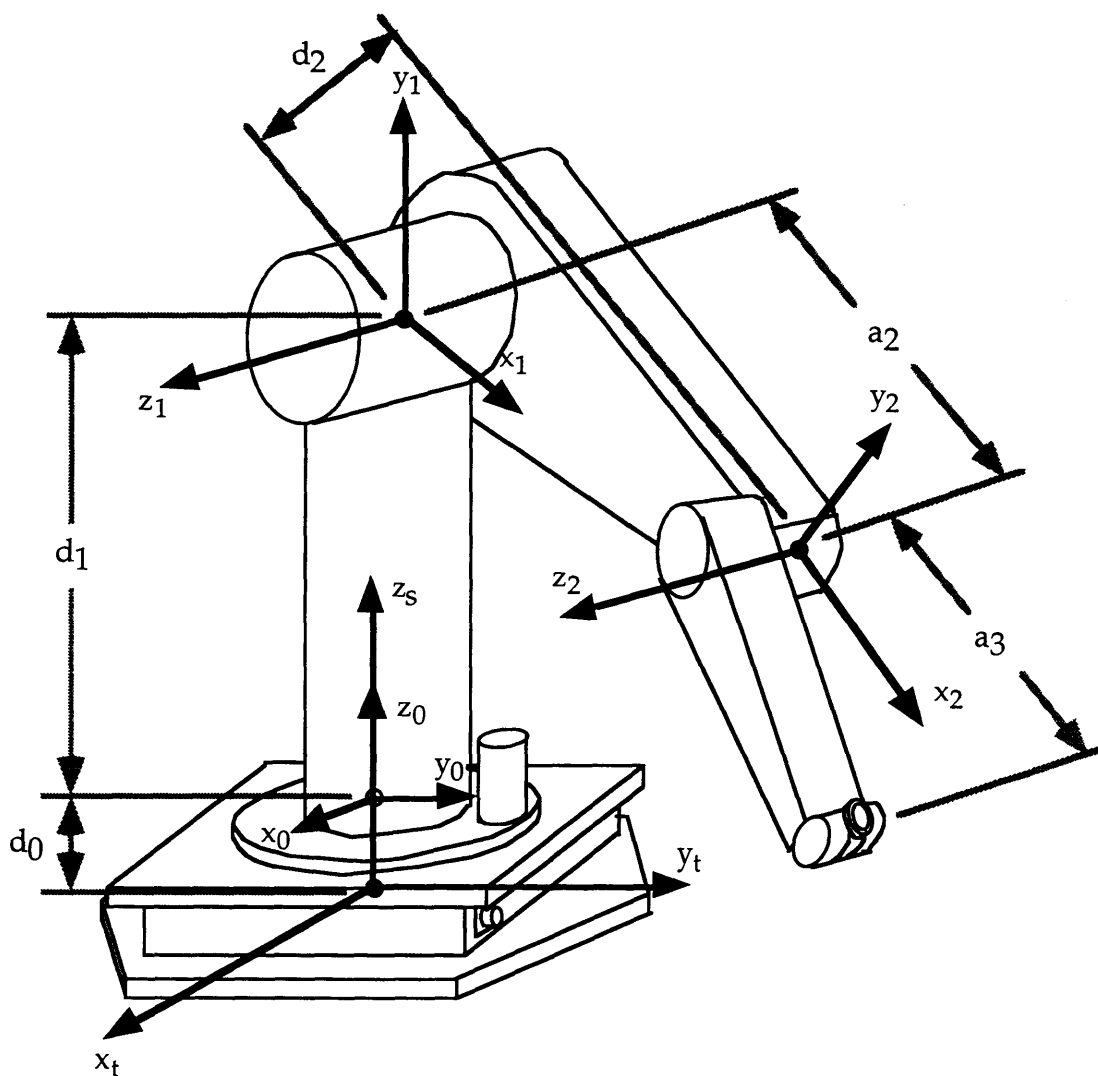
- Marquardt, D.W., and Snee, R.D., "Ridge Regression in Practice," *American Statistician*, Vol. 29, pp. 3-20, 1975
- Merritt, H., *Hydraulic Control Systems*, John Wiley and Sons, New York, 1967
- Mills, J.K., "Simultaneous Control of Robot Manipulator Impedance and Generalized Force and Position," *Journal of Mechanisms and Machine Theory*, Vol. 31, No. 8, pp. 1069-1080, 1996
- Morel, G. and Dubowsky, S., "The Precise Control of Manipulators with Joint Friction: A Base Force/Torque Sensor Method," *Proceedings of IEEE International Conf. on Robotics and Automation*, Vol. 1, pp. 360-365, 1996
- Pfeffer, L.E. , Khatib, O., and Hake, J., "Joint Torque Sensory Feedback in the Control of a PUMA Manipulator," *IEEE Transactions on Robotics and Automation*, Vol. 5, No. 4, pp. 418-425, 1989
- Popovic, M.R., Shimoga, K.B., and Goldenberg, A.A., "Model Based Compensation Of Friction In Direct Drive Robotic Arms," *Journal of Studies in Informatics and Control*, Vol. 3, No 1., pp. 75-88, March 1994.
- Popovic, M.R., Gorinevsky, D.M. and Goldenberg, A.A., "Accurate Positioning Of Devices With Nonlinear Friction Using Fuzzy Logic Pulse Controller," *International Symposium of Experimental Robotics, ISER '95, preprints*, pp. 206-211, 1995
- Roberge, Gould, Markey, and Trumper, *M.I.T. Course 2.737 Mechatronics Course Notes*, 1996
- Siciliano, B., Canudas de Wit, C., and Bastin, G.—Editors, *Theory of Robot Control*, London, Springer-Verlag, 1996
- Slotine, J.-J.E. and Li, W., "On the Adaptive Control of Robot Manipulators," *International Journal of Robotics Research*, Vol. 6, No. 3, pp. 49-59, Fall 1987



- Slotine, J.-J.E. and Li, W., *Applied Nonlinear Control*, New Jersey, Prentice Hall, 1991
- Vischer, D., and Khatib, O., "Design and Development of High-Performance Torque-Controlled Joints," *IEEE Transactions on Robotics and Automation*, Vol. 11, No. 4, August 1995
- Volpe, R., and Khosla, P., "An Analysis Of Manipulator Force Control Strategies Applied To An Experimentally Derived Model," *Proceedings of the IEEE/ RSJ International Conference on Intelligent Robots and Systems*, pp. 1989-1997, 1992
- West, H., Papadopoulos, E., Dubowsky, S., and Cheah, H., "A Method For Estimating the Mass Properties of a Manipulator by Measuring the Reaction Moments at its Base," *Proceedings of the IEEE International Conference on Robotics and Automation*, pp. 1510-1516, 1989
- Whitney, D., "Historical Perspective and State of the Art in Robot Force Control," *International Journal of Robotics Research*, Vol. 6, No. 1, pp. 3-14, Spring 1987
- Williams, D., and Khatib, O., "Improved Force Control for Conventional Arms Using Wrist-Based Torque Feedback," *International Symposium of Experimental Robotics, ISER 95, preprints*, pp. 323-328, 1995

# Appendix A

## PUMA 550 Kinematic Description



Kinematic Parameter Values (Corrigan,1994):

- |                           |                          |
|---------------------------|--------------------------|
| $d_0 = 0.189 \text{ m}$   | $a_2 = 0.4318 \text{ m}$ |
| $d_1 = 0.672 \text{ m}$   | $a_3 = 0.4331 \text{ m}$ |
| $d_2 = -0.2435 \text{ m}$ |                          |
| $d_3 = 0.098 \text{ m}$   |                          |

## Appendix B

### Base Force/Torque Sensor Calibration Procedure

This section describes a decomposition-based on-site calibration method for force/torque sensors, which was developed with Guangjun Liu.

#### B.1 Standard Calibration Method

The output voltage signals from a force/torque sensor are related to the applied wrench by:

$$f = C v \quad (\text{B.1})$$

where  $f \in \mathcal{R}^n$  is the force/torque wrench measured by the base sensor. The vector  $v \in \mathcal{R}^n$  is the output signals from the sensor. The matrix  $C \in \mathcal{R}^{n \times n}$  which relates  $f$  and  $v$  is a calibration matrix. The task of sensor calibration is to determine the values of the components of the matrix  $C$ . This is difficult due to the fact that  $C$  is not diagonal. Small off-diagonal terms, called coupling terms, remain and must be accurately identified.

Calibration is generally performed by applying precisely known loads to the sensor and recording the output signals. These data are then used to calculate  $C$ . There are various ways to apply the loads and calculate  $C$ . For example, suppose  $n$  different loads are applied to the sensor:  $f_i$  ( $i=1,2,\dots,n$ ). The corresponding signals are  $v_i$  ( $i=1,2,\dots,n$ ). From Equation B.1, the following equation holds:

$$[f_1 \ f_2 \ \dots \ f_n] = C [v_1 \ v_2 \ \dots \ v_n] \quad (\text{B.2})$$

Or in a more compact form:

$$F = C V \quad (B.3)$$

where  $F = [f_1 \ f_2 \ \dots \ f_n]$  and  $V = [v_1 \ v_2 \ \dots \ v_n]$ .

If the  $n$  different loads are applied such that  $v_i$  ( $i=1,2,\dots,n$ ) are linearly independent, then  $V$  is full rank and invertible. Then  $C$  can be obtained as:

$$C = F V^{-1} \quad (B.4)$$

Equation B.4 requires only  $n$  data points. However, for each data point, the  $n$  loads have to be carefully applied to ensure that  $V$  is invertible and well-conditioned. Theoretically, this would imply that each load would be applied directly along one of the sensor's  $n$  axes, with no off-axis loading.

This requirement is impossible to achieve in practice, due to coupling among the axes. For instance, when a sensor is fixed horizontally as shown in Figure 2.5, it is impossible to apply a load purely in the  $F_z$  direction, since the PUMA manipulator physically interferes with load application. Additionally, since the sensor center is located at some distance inside the sensor body, it is difficult to apply a pure force without exerting a corresponding moment.

In practice it is much easier to apply a load to one axis of the sensor if it is not necessary to know its effect on the other axes. This observation is the basis for a calibration method that requires that applied loads be well known along only one axis at a time. The method is described in the following section.

## B.2 Proposed Calibration Method

Consider the  $i^{\text{th}}$  axis of  $f$  in Equation B.1:

$$f_i = \sum_{j=1}^n C_{ij} v_j \quad i=1,2,\dots,n \quad (B.5)$$

Equation B.5 can be rewritten as follows:

$$f_i = \sum_{j=1}^n v_j C_{ij} = [v_1 \ v_2 \ \dots \ v_n] \begin{bmatrix} C_{i1} \\ C_{i2} \\ \cdot \\ \cdot \\ C_{in} \end{bmatrix} \quad (\text{B.6})$$

For  $k$  data points,

$$\begin{bmatrix} f_{i1} \\ f_{i2} \\ \cdot \\ \cdot \\ f_{ik} \end{bmatrix} = \begin{bmatrix} v_{i11} & v_{i21} & \dots & v_{ik1} \\ v_{i12} & v_{i22} & & v_{ik2} \\ \cdot & & & \\ \cdot & & & \\ v_{i1n} & v_{i2n} & & v_{ikn} \end{bmatrix} \begin{bmatrix} C_{i1} \\ C_{i2} \\ \cdot \\ \cdot \\ C_{in} \end{bmatrix} \quad (\text{B.7})$$

Or in a more compact form:

$$F_i = V_i C_i \quad (\text{B.8})$$

To determine the  $n$  components of  $C_i$ , at least  $i$  data points are required.

If  $V_i$  is invertible,  $C_i$  can be found by:

$$C_i = V_i^{-1} F_i \quad (\text{B.9})$$

In practice it is desirable to use more than the minimum number of data points, in order to assure a full rank, well-conditioned matrix. If more than  $n$  data points are used,  $C_i$  can be estimated using the least squares method:

$$C_i = (V_i^T V_i)^{-1} V_i^T F_i \quad (\text{B.10})$$

Note that this equation is only a function of forces applied in the  $i$  direction. Equation B.6 extracts the applied force along a single axis from from the applied wrench, and thus forces in other directions ( $F_k, k \neq i$ ) need not be measured. Note, however, that  $V_i^T V_i$  will be non-singular and well-conditioned only when components in the non-control directions ( $V_k, k \neq i$ ) are suitably large and variable. Thus, forces must be applied along non-control directions, but it is again important to note that the magnitude of these forces does not need to be precisely known. The importance of this results will be clarified in the following section.

### B.3 Practical Implementation

In the calibration procedure, a force or moment of well-known magnitude was applied to an axis. Several data points were collected, by applying known loads of increasing magnitude. For each measurement, unknown forces were applied to the orthogonal axes, one axis at a time.

Moments were applied by hanging known weights from a bar bolted to the mounting plate, or by simple pulleys and cables (see Figures B.1 and B.2).

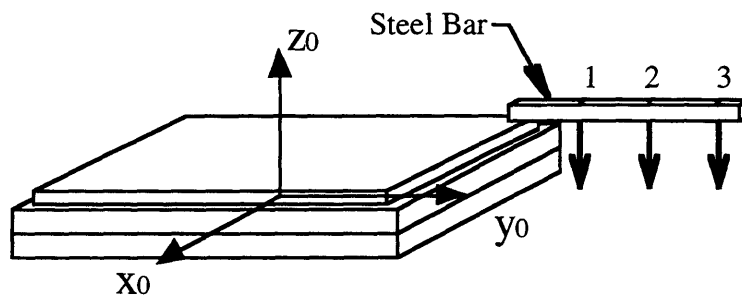


Figure B.1: Application of Moments:  $M_x$  Direction (PUMA Robot Hidden)

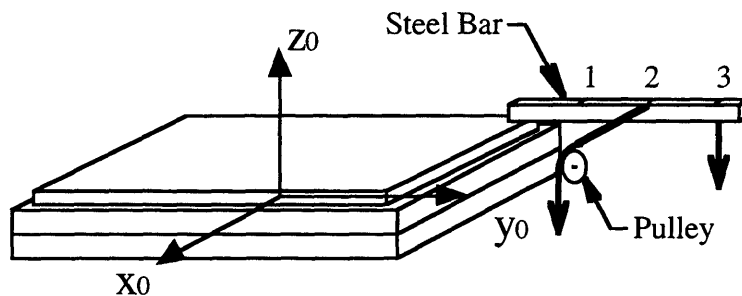


Figure B.2: Application of  $M_x$  Moment and  $F_x$  Force (PUMA Robot Hidden)

During the experiment, it is important to maintain parallelism of the applied load with the axis of interest.

In summary, for calibration of a single axis of the base force/torque sensor the following simple procedure was followed:

- 1) A well-known load was applied along the axis of interest, using either a hanging weight (for the  $M_x$ ,  $M_y$ , and  $F_z$  directions) or a pulley (for the  $F_x$ ,  $F_y$ , and  $M_z$  directions).

- 2) Additional well-known loads of different magnitudes were applied along the axis of interest in the same manner. This was done in order to improve the accuracy of the subsequent least-squares estimation.
- 3) With a known load applied to the axis of interest, a load of unknown magnitude was applied to an orthogonal (non-control) axis.
- 4) Step (3) was repeated along a different orthogonal axis, until all orthogonal axes had been exercised.
- 5) The row entry to the calibration matrix  $C$  corresponding to the axis of interest was computed with Equation B.10.

## Appendix C

### Complete Inertial Parameter Matrix for a PUMA 550 Manipulator

The following equations describe the elements of the 6x15 matrix Y in Equation 4.17. For compactness, the notation  $(c_i, s_i)$  represents  $(\cos(\theta_i), \sin(\theta_i))$ .

$$\begin{aligned} Y_{11} &= -c_1 \dot{q}_1^2 - s_1 \ddot{q}_1 \\ Y_{12} &= -s_1 \dot{q}_1^2 + c_1 \ddot{q}_1 \\ Y_{13} &= -s_1 c_2 \ddot{q}_1 - c_1 s_2 \ddot{q}_2 - \dot{q}_1^2 c_1 c_2 - c_1 c_2 \dot{q}_2^2 + 2s_1 s_2 \dot{q}_1 \dot{q}_2 \\ Y_{14} &= s_1 s_2 \ddot{q}_1 - c_1 c_2 \ddot{q}_2 + \dot{q}_1^2 c_1 s_2 + c_1 s_2 \dot{q}_2^2 + 2s_1 c_2 \dot{q}_1 \dot{q}_2 \\ Y_{15} &= -s_1 \dot{q}_1^2 + c_1 \ddot{q}_1 \\ Y_{16} &= -s_1 \dot{q}_1^2 d_2 + c_1 \ddot{q}_1 d_2 \\ Y_{17} &= 0 \\ Y_{18} &= 0 \\ Y_{19} &= 0 \\ Y_{110} &= 0 \\ Y_{111} &= 0 \\ Y_{112} &= 0 \\ Y_{113} &= 0 \\ Y_{114} &= 0 \\ Y_{115} &= 0 \\ Y_{21} &= -s_1 \dot{q}_1^2 + c_1 \ddot{q}_1 \\ Y_{22} &= c_1 \dot{q}_1^2 + s_1 \ddot{q}_1 \\ Y_{23} &= c_1 c_2 \ddot{q}_1 - s_1 s_2 \ddot{q}_2 - \dot{q}_1^2 s_1 c_2 - s_1 c_2 \dot{q}_2^2 - 2c_1 s_2 \dot{q}_1 \dot{q}_2 \\ Y_{24} &= -c_1 s_2 \ddot{q}_1 - s_1 c_2 \ddot{q}_2 + s_1 \dot{q}_1^2 s_2 + s_1 s_2 \dot{q}_2^2 - 2c_1 s_2 \dot{q}_1 \dot{q}_2 \\ Y_{25} &= c_1 \dot{q}_1^2 + s_1 \ddot{q}_1 \\ Y_{26} &= d_2 c_1 \dot{q}_1^2 + d_2 s_1 \ddot{q}_1 \end{aligned}$$



$$\begin{aligned}
Y_{27} &= 0 \\
Y_{28} &= 0 \\
Y_{29} &= 0 \\
Y_{210} &= 0 \\
Y_{211} &= 0 \\
Y_{212} &= 0 \\
Y_{213} &= 0 \\
Y_{214} &= 0 \\
Y_{215} &= 0 \\
Y_{31} &= 0 \\
Y_{32} &= 0 \\
Y_{33} &= -s_2\dot{q}_2^2 + c_2\ddot{q}_2 \\
Y_{34} &= -c_2\dot{q}_2^2 - s_2\ddot{q}_2 \\
Y_{35} &= 0 \\
Y_{36} &= 0 \\
Y_{37} &= 0 \\
Y_{38} &= 0 \\
Y_{39} &= 0 \\
Y_{310} &= 0 \\
Y_{311} &= 0 \\
Y_{312} &= 0 \\
Y_{313} &= 0 \\
Y_{314} &= 0 \\
Y_{315} &= 0 \\
Y_{41} &= 0 \\
Y_{42} &= 0 \\
Y_{43} &= -c_1s_2\dot{q}_1^2d_2 + c_1s_2d_2\dot{q}_2^2 - c_1c_2d_2\ddot{q}_2^2 - c_1c_2d_2\ddot{q}_2 - s_1s_2\ddot{q}_1d_2 \\
Y_{44} &= d_2(-c_1c_2\dot{q}_1^2 + c_1c_2\dot{q}_2^2 + c_1s_2\ddot{q}_2 - s_1c_2\ddot{q}_1) \\
Y_{45} &= 0 \\
Y_{46} &= 0 \\
Y_{47} &= -s_1\dot{q}_1^2 + c_1\ddot{q}_1 \\
Y_{48} &= 0 \\
Y_{47} &= -s_1\dot{q}_1^2 + c_1\ddot{q}_1 \\
Y_{48} &= 0 \\
Y_{49} &= c_1\dot{q}_1^2 + s_1\ddot{q}_1 \\
Y_{410} &= c_1c_2s_2\ddot{q}_1 - s_1c_2s_2\dot{q}_1^2 + \dot{q}_1\dot{q}_2(2c_1c_2^2 - c_1) \\
Y_{411} &= \ddot{q}_1(2c_1c_2^2 - c_1) + \dot{q}_1^2(-2s_1c_2^2 + s_1) - 4c_1c_2s_2\dot{q}_1\dot{q}_2
\end{aligned}$$

$$\begin{aligned}
Y_{4,12} &= \dot{q}_1^2 c_1 s_2 - c_1 s_2 \dot{q}_2^2 + c_1 c_2 \ddot{q}_2 + s_1 s_2 \ddot{q}_1 \\
Y_{4,13} &= -c_1 c_2 s_2 \ddot{q}_1 + s_1 c_2 s_2 \dot{q}_1^2 + \dot{q}_1 \dot{q}_2 (-2c_1 c_2^2 + c_1) \\
Y_{4,14} &= \dot{q}_1^2 c_1 c_2 - c_1 c_2 \dot{q}_2^2 - c_1 s_2 \ddot{q}_2 + s_1 c_2 \ddot{q}_1 \\
Y_{5,1} &= 0 \\
Y_{5,2} &= 0 \\
Y_{5,3} &= -s_1 s_2 \dot{q}_1^2 d_2 + s_1 s_2 d_2 \dot{q}_2^2 + c_1 s_2 \ddot{q}_1 d_2 - s_1 c_2 d_2 \ddot{q}_2 \\
Y_{5,4} &= -s_1 c_2 \dot{q}_1^2 d_2 + s_1 c_2 d_2 \dot{q}_2^2 + c_1 c_2 \ddot{q}_1 d_2 + s_1 s_2 d_2 \ddot{q}_2 \\
Y_{5,5} &= 0 \\
Y_{5,6} &= 0 \\
Y_{5,7} &= c_1 \dot{q}_1^2 - c_1 \ddot{q}_1 \\
Y_{5,8} &= 0 \\
Y_{5,9} &= s_1 \dot{q}_1^2 - c_1 \ddot{q}_1 \\
Y_{5,10} &= s_1 c_2 s_2 \ddot{q}_1 + c_1 c_2 s_2 \dot{q}_1^2 + \dot{q}_1 \dot{q}_2 (2s_1 c_2^2 - s_1) \\
Y_{5,11} &= \ddot{q}_1 (2s_1 c_2^2 - s_1) + \dot{q}_1^2 (2c_1 c_2^2 - c_1) - 4s_1 c_2 s_2 \dot{q}_1 \dot{q}_2 \\
Y_{5,12} &= s_1 \dot{q}_1^2 s_2 - s_1 s_2 \dot{q}_2^2 - c_1 s_2 \ddot{q}_1 + s_1 c_2 \ddot{q}_2 \\
Y_{5,13} &= -s_1 c_2 s_2 \ddot{q}_1 - c_1 c_2 s_2 \dot{q}_1^2 + \dot{q}_1 \dot{q}_2 (-2s_1 c_2^2 + s_1) \\
Y_{5,14} &= \dot{q}_1^2 s_1 c_2 - s_1 c_2 \dot{q}_2^2 - c_1 c_2 \ddot{q}_1 - s_1 s_2 \ddot{q}_2 \\
Y_{5,15} &= -c_1 \ddot{q}_2 + \dot{q}_1 \dot{q}_2 s_1 \\
Y_{6,1} &= 0 \\
Y_{6,2} &= 0 \\
Y_{6,3} &= -\ddot{q}_2 s_2 d_2 - \dot{q}_2^2 c_2 d_2 \\
Y_{6,4} &= -\ddot{q}_2 c_2 d_2 - \dot{q}_2^2 s_2 d_2 \\
Y_{6,5} &= 2\ddot{q}_1 d_2 \\
Y_{6,6} &= \ddot{q}_1 d_2^2 \\
Y_{6,7} &= 0 \\
Y_{6,8} &= \ddot{q}_1 \\
Y_{6,9} &= 0 \\
Y_{6,10} &= \ddot{q}_1 (1 - c_2^2) + 2c_2^2 s_2 \dot{q}_1 \dot{q}_2 \\
Y_{6,11} &= 2c_2 s_2 \ddot{q}_1 + \dot{q}_1 \dot{q}_2 (4c_2^2 - 2) \\
Y_{6,12} &= c_2 \dot{q}_2^2 + s_2 \ddot{q}_2 \\
Y_{6,13} &= -2c_2 s_2 \dot{q}_1 \dot{q}_2 + c_2^2 \ddot{q}_1 \\
Y_{6,14} &= -s_2 \dot{q}_2^2 + c_2 \ddot{q}_2 \\
Y_{6,15} &= 0
\end{aligned}$$